Radiation Modeling in Shock-Tubes and Entry Flows

Prof. Sergey T. Surzhikov
Institute for Problems in Mechanics Russian Academy of Sciences
101-1, Vernadskogo prosp.
Moscow, 119526
Russia

surg@ipmnet.ru

ABSTRACT

In the present lecture some basic problems of state and solving of radiation heat transfer equation as applied to radiation modelling in shock-tubes and entry flow are discussed. The lecture contains five parts.

In the first part the radiation heat transfer equation and the general definitions of the radiation heat transfer theory are presented. The definitions introduced in the first part are widely used in other parts.

The second part of the lecture (Chapter 3) presents four methods which are used for solution of radiation heat transfer problems in different aerospace applications.

Well known problem of radiation heat transfer in heated gases and low-temperature plasma in view of atomic and molecular rotational lines, as well as of the vibrational molecular bands, are discussed in the third part. Some untraditional models of radiation heat transfer are presented in this part.

The fourth part of the lecture is dedicated to the Monte-Carlo algorithms which are also in common use in aerospace problems, especially at prediction of emissivities of heated and radiating volumes of light-scattering gases. Several traditional and novel algorithms are presented in this part.

The final part (Chapter 6) of the lecture presents examples of using of numerical simulation methods described in previous parts at solution of various radiation heat transfer problems in aerospace applications. It should be stressed that the methods of the radiation heat transfer integration and various numerical simulation results presented in the lecture were used and obtained by the author at solution of concrete problems of aerospace physical gas dynamics.

The study was supported by the Russian Foundation of Basic Research (grant # 07-01-0133).

Report Documentation Page

Form Approved
OMB No. 0704-0188

1. REPORT DATE	2. REPORT TYPE	3. DATES COVERED
SEP 2009	**N/A**	**-**

4. TITLE AND SUBTITLE	5a. CONTRACT NUMBER
Radiation Modeling in Shock-Tubes and Entry Flows	5b. GRANT NUMBER
	5c. PROGRAM ELEMENT NUMBER
6. AUTHOR(S)	5d. PROJECT NUMBER
	5e. TASK NUMBER
	5f. WORK UNIT NUMBER
7. PERFORMING ORGANIZATION NAME(S) AND ADDRESS(ES) **Institute for Problems in Mechanics Russian Academy of Sciences 101-1, Vernadskogo prosp. Moscow, 119526 Russia**	8. PERFORMING ORGANIZATION REPORT NUMBER
9. SPONSORING/MONITORING AGENCY NAME(S) AND ADDRESS(ES)	10. SPONSOR/MONITOR'S ACRONYM(S)
	11. SPONSOR/MONITOR'S REPORT NUMBER(S)

12. DISTRIBUTION/AVAILABILITY STATEMENT
Approved for public release, distribution unlimited

13. SUPPLEMENTARY NOTES
See also ADA562449. RTO-EN-AVT-162, Non-Equilibrium Gas Dynamics - From Physical Models to Hypersonic Flights (Dynamique des gaz non- equilibres - Des modeles physiques jusqu'au vol hypersonique)., The original document contains color images.

14. ABSTRACT
In the present lecture some basic problems of state and solving of radiation heat transfer equation as applied to radiation modelling in shock-tubes and entry flow are discussed. The lecture contains five parts. In the first part the radiation heat transfer equation and the general definitions of the radiation heat transfer theory are presented. The definitions introduced in the first part are widely used in other parts. The second part of the lecture (Chapter 3) presents four methods which are used for solution of radiation heat transfer problems in different aerospace applications. Well known problem of radiation heat transfer in heated gases and low-temperature plasma in view of atomic and molecular rotational lines, as well as of the vibrational molecular bands, are discussed in the third part. Some untraditional models of radiation heat transfer are presented in this part. The fourth part of the lecture is dedicated to the Monte-Carlo algorithms which are also in common use in aerospace problems, especially at prediction of emissivities of heated and radiating volumes of light-scattering gases. Several traditional and novel algorithms are presented in this part. The final part (Chapter 6) of the lecture presents examples of using of numerical simulation methods described in previous parts at solution of various radiation heat transfer problems in aerospace applications. It should be stressed that the methods of the radiation heat transfer integration and various numerical simulation results presented in the lecture were used and obtained by the author at solution of concrete problems of aerospace physical gas dynamics.

15. SUBJECT TERMS

16. SECURITY CLASSIFICATION OF:			17. LIMITATION OF ABSTRACT	18. NUMBER OF PAGES	19a. NAME OF RESPONSIBLE PERSON
a. REPORT **unclassified**	b. ABSTRACT **unclassified**	c. THIS PAGE **unclassified**	**SAR**	**102**	

Standard Form 298 (Rev. 8-98)
Prescribed by ANSI Std Z39-18

CONTENTS

1.0 Introduction 3

2.0 Radiation heat transfer equation and general characteristics of heat radiation transfer 4

2.1 Classification of spectral optical models 4

2.2 General notations of the radiation heat transfer theory 5

3.0 Methods of integration of radiation heat transfer equations 9

3.1 The P_N (Spherical Harmonic) approximation 9

3.2 Quadro-moment methods 25

3.3 Ray-Tracing method 29

3.4 Discreet ordinates method 31

4.0 Random models 35

4.1. Formulation of Random Models for Atomic Lines 35

4.2. Numerical Simulation Method for Calculation of Radiative Heat Transfer in Plane-Parallel Non-Uniform Layers 38

4.3. The Macro-Random Model for Describing of Radiative Heat Transfer with Vibrational Band Structure 43

5.0 The Monte-Carlo methods 47

5.1 Line by line integration of radiation heat transfer equation on spectrum of rotational lines 47

5.2 Hybrid Statistical Method 48

5.3 Method of the smoothed coefficients 53

5.4 The two-group method 53

5.5 Line-by-line integration with little number of trajectories 54

5.6 The Monte-Carlo imitative method based on the Maximum Cross Section (MCS) method 54

5.7 Imitative Monte-Carlo algorithm based on the quasi-random sampling of photon trajectory parameters 56

5.8 The hybrid method based on the quasi-random sampling method 56

5.9 Three-dimensional simulation algorithms 56

5.10 Monte-Carlo Local Estimation of Directional Emissivity (MCLEDE) 56

6.0 Examples of application of methods for solving radiation heat transfer equations 59

6.1 P_1-approximation 59

6.2 The quadro-moment method 62

6.3 The ray-tracing method 63

6.4 Discrete ordinates method 68

6.5 Random models of atomic lines 69

6.6 Macro-random model 73

6.7 The Monte-Carlo method 77

References 95

1.0 INTRODUCTION

The term “thermal radiation” (“heat radiation”) means electromagnetic radiation of atomic and molecular, as opposed to nuclear, origin. Such radiation is emitted by matter in a state of thermal excitation, thus accounting for the designation of the radiation as thermal. The energy density of this type of radiation is given by the Planck formula for black body radiation. More generally the radiation energy distribution is described by a *kinetic* or *transport* equation, referred to historically as the equation of radiative transfer.

The importance of thermal radiation in physical problems, and particularly in problems of physical gas dynamics in different aerospace applications, increases as the temperatures is raised. At moderate temperatures ($10^4 \lesssim T \lesssim 10^5$ K), the role of radiation is primary one of transporting energy in gases and plasmas by radiative processes. At higher temperatures ($T \gtrsim 10^5 \div 10^6$ K), the energy and momentum densities of radiation field may become comparable or dominate the corresponding fluid quantities. As a rule, hydrodynamics with explicit account of the radiation energy and momentum contributions constitutes subject of investigation of “high-temperature radiation hydrodynamics”. More general definition of radiation gasdynamic implies consideration of coupled radiative and gasdynamic processes. In the partial case of the weak radiation-gasdynamic interaction there is possibility to study radiative and gasdynamic phenomena separately. For example, such a case is realized for spacecraft at entry velocities up to $6 \div 8$ km/s.

Radiative gas dynamics (RadGD) is the directions of physical gas dynamics which is connected to such challenging sciences as: astrophysics, physics of stars and Sun, research of a structure of substance (atomic and molecular spectroscopy), interaction of laser radiation and high-energy beams with materials, plasma generators, rocket engines (of chemical, plasma, electric, nuclear or laser types), spacecraft's thermal protection, heat exchange in steam boiler, in aircraft and rocket engines, in working volumes of various power installations (including nuclear).

Figure 1.1 shows hierarchical division of the Radiative gas dynamics. In order to solve any RadGD problem there is a necessity to create a *radiative model* of a gas or plasma. The radiative model is defined as the set of *optical model* and *radiation transfer model*.

The optical model includes spectral, group and integral absorption, emission and scattering coefficients, which are in turn based on cross-sections (or probabilities) of elementary radiative processes predicted by quantum mechanics and quantum chemistry. The absorption, emission and scattering coefficients can be determined only with use data on distribution functions for atomic and molecular particles, and also on their energy states. Thermodynamics and statistical physics provide all necessary information for these purposes.

The radiation transfer model, composing the second part of the radiative model, is based on the thermodynamics and statistical physics, and is designed for prediction such characteristics of a radiation field as the radiation energy density U, the radiation flux $\vec{W}$, and the divergence of the radiation flux $Q_{rad} = \mathrm{div}\vec{W}$. A spectral region of the electromagnetic radiation, which is of practical interest for various aerospace applications ranges from $\approx 0.05\,\mu$m until $\approx 20\,\mu$m. This spectral region is divided on the following sub regions:

- $\Delta\lambda \approx 0.05 \div 0.4\,\mu$m is the ultraviolet region;
- $\Delta\lambda \approx 0.4 \div 0.7\,\mu$m is the visible region;
- $\Delta\lambda \approx 0.7 \div 20.0\,\mu$m is the infrared region,

where $\Delta\lambda$ is the wavelength interval. A radiation emitted by matter in this spectral region is called as *heat radiation*.

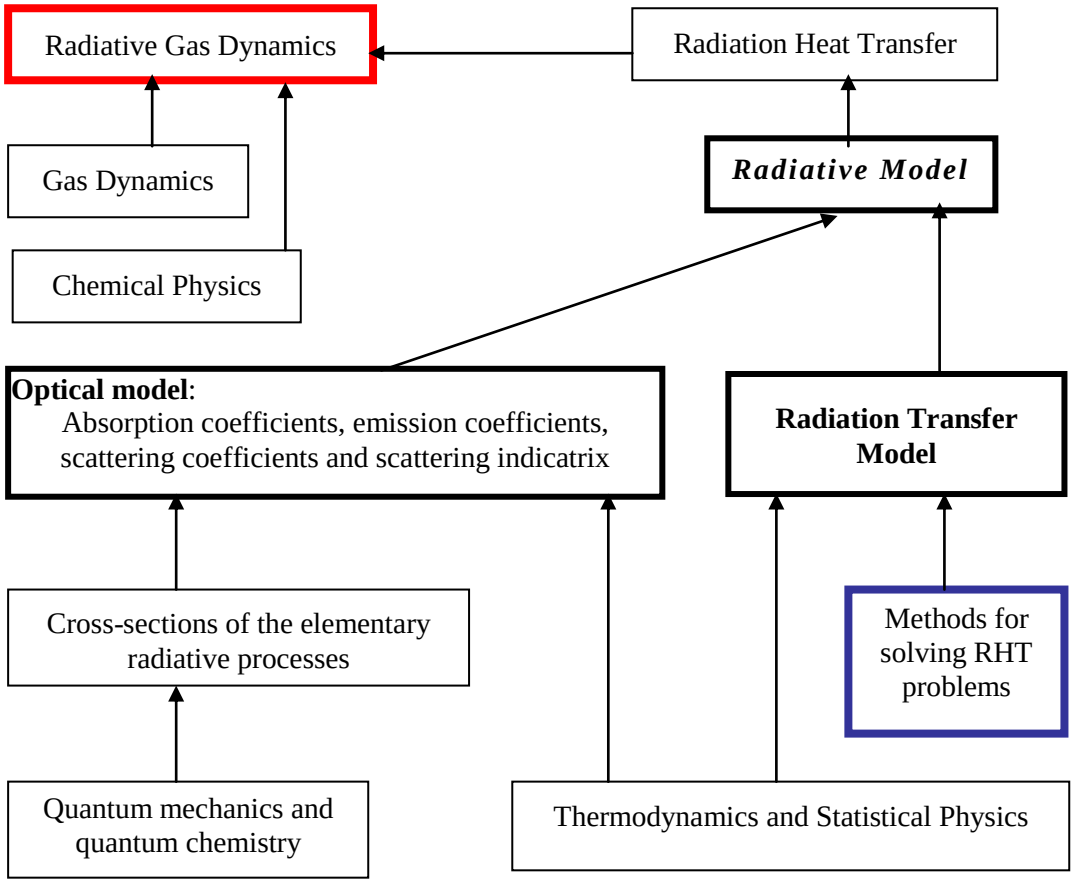

Figure 1.1: Basic scheme of Radiative Gas Dynamics

2.0 RADIATION HEAT TRANSFER EQUATION AND GENERAL CHARACTERISTICS OF HEAT RADIATION TRANSFER

2.1 Classification of spectral optical models

Classification of the spectral optical models was introduced in [1]:

1) *Optical model* $k_\omega(T,\varphi)$ is spectral, quasi-spectral, multigroup and combined models of absorption coefficients representing in the table, analytical, graphical or in a computer module form. Here ω is the Wavenumber; T is the temperature; φ is set of the parameters (pressure or density, concentration of the chemical components). In the case of a nonequilibrium medium instead of T we should use set of effective temperatures (electronic temperature, vibrational temperature, rotational temperature).

2) *Spectral* (*line-by-line*) *model* $k_\omega(T,\varphi)$ is the function with continuous and lines structure without any smoothing.

3) *Multigroup model* is the smoothing spectral model in a set of spectral ranges $\Delta\omega_i$. We suppose in the each spectral range $\Delta\omega_i$ the absorption coefficient is independent of wavenumber.

4) *Quasi-spectral (quasi-continuum) model* is the smeared rotational line model for a set of spectral ranges. The value $\Delta\omega_i$ in this model must be larger than maximal values of the rotational lines widths (that is not less than $25 \div 50$ cm^{-1}). As a rule, quasi-spectral model is included to multigroup model.

5) *Total absorption model* is the Planck mean absorption coefficient, or (and) the Rosseland mean absorption coefficient, or (and) the Chandrasekhar mean absorption coefficient.

6) *Combined model* is the sum of the spectral line absorption and the multigroup absorption model (as a rule the selective atomic lines absorption on the continuum or quasi-continuum background).

7) *Radiative heat transfer model* is the set of:

- conditions (the thermodynamic conditions in a medium, radiation heat transfer boundary conditions, the spectral resolution of numerical calculations);
- equation of radiation heat transfer;
- mathematical method using for solving this equation.

8) *Radiative model* is the set of the optical model and the radiation heat transfer model.

9) *Optimum radiative model* is the radiative model containing minimum number of the spectral groups and in the same time, permitting to obtain physical adequately results.

Figure 2.1 shows example of air low-temperature plasma.

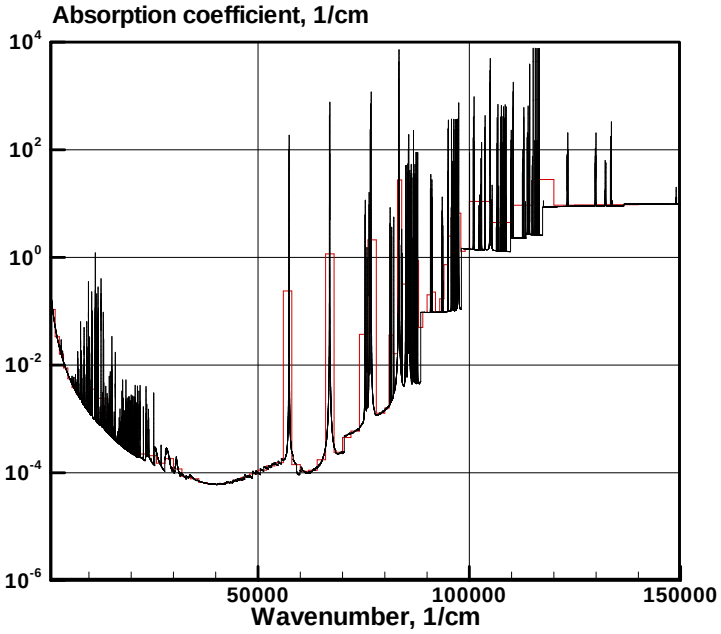

Figure 2.1: Line-by-line and group spectral model of absorption coefficient of air at *T* = 10000 K and *p* = 1 atm

2.2 General notations of the radiation heat transfer theory

The steady-state radiation heat transfer equation, which is taking into consideration scattering processes has the following form [2, 3]:

$$\frac{\partial J_\nu\left(s,\vec{\Omega}\right)}{\partial s}+\kappa_\nu J_\nu\left(s,\vec{\Omega}\right)+\sigma_\nu J_\nu\left(s,\vec{\Omega}\right)=j_\nu\left(s\right)+\frac{\sigma_\nu}{4\pi}\int_{4\pi}p_\nu\left(s,\vec{\Omega}'\to\vec{\Omega}\right)J_\nu\left(\vec{\Omega}'\right)\mathrm{d}\vec{\Omega}'\ , \qquad (1)$$

where $J_\nu\left(s,\vec{\Omega}\right)$ is the spectral radiation intensity; $\kappa_\nu(s)$ is the spectral absorption coefficient; $\sigma_\nu(s)$ is the spectral scattering coefficient; $j_\nu(s)$ is the spectral emission coefficient; $p_\nu\left(\vec{\Omega}'\to\vec{\Omega}\right)$ is the spectral

phase function for scattering (the scattering indicatrix), s is the physical co-ordinate along spatial direction $\vec{\Omega}$. Angular variables for unit vector $\vec{\Omega}$ are presented in Figure 2.2.

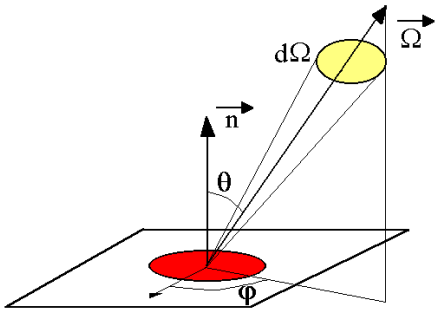

Figure 2.2: Angular co-ordinates for integration of a spectral radiation intensity on solid angle

The following type of the equation is especially often uses:

$$\vec{\Omega}\cdot\nabla J_\nu\left(s,\vec{\Omega}\right)+\kappa_\nu J_\nu\left(s,\vec{\Omega}\right)=\kappa J_{b,\nu}\left[T\left(s\right)\right], \tag{2}$$

where

$$J=J_{b,\nu}\left[T\left(s\right)\right]=\frac{2h\nu^3}{c^2\left[\exp\left(\frac{h\nu}{kT}\right)-1\right]}$$

is the Planck intensity (the spectral intensity of the black body emissivity); h,k are the Planck and Boltzman constants; c is the speed of light.

Equation (2) is correct for the Local Thermodynamic Equilibrium (LTE), and does not take into account scattering processes.

The following units for the electromagnetic spectra measurement are in common use: λ is the wavelength (in microns, Angstroms, nanometers; 1 μm = 10^{-6} cm, 1Å = 10^{-8} cm, 1 nm = 10^{-9} m); ν is the frequency (in s^{-1}); ω is the wavenumber (in cm^{-1}). These units are connected with the following relations (for radiative processes in vacuum): $\nu=c\omega,\ c=\nu\lambda$. This allows to write the following correlations for the Planck function: $J_\nu d\nu=J_\omega d\omega,\ J_\nu d\nu=-J_\lambda d\lambda$. To recalculate the wavelength to the wavenumber one can use the following relation: $\lambda_{\mu m}=10^4/\omega_{cm^{-1}}$.

The wavelength and wavenumber dependencies of the Planck function at different temperatures are shown in Figures 2.3. These data together with the Wien displacement law $\lambda_{max}T=2897.8$ μm·K are very suitable for express analysis of the radiation heat transfer problems. Here λ_{max} is the wavelength, in μm, at which the emissive power J is a maximum for a given temperature T (in K).

The spectral radiation intensity allows define the following general spectral and integral characteristics of the radiation field:

$U_\omega=\frac{1}{c}\int_{4\pi}J_\omega\left(s,\vec{\Omega}\right)d\Omega$ is the spectral energy density;

$\vec{W}_\omega=\frac{1}{c}\int_{4\pi}J_\omega\left(s,\vec{\Omega}\right)\vec{\Omega}\,d\Omega$ is the spectral flux;

$q_{R,n,\omega} = \left(\vec{W}_\nu \cdot \vec{n}\right) = \int\limits_{4\pi} J_\omega\left(s,\vec{\Omega}\right)\left(\vec{\Omega}\cdot\vec{n}\right)\mathrm{d}\Omega$ is the spectral hemispherical flux;

$U = \int\limits_0^\infty U\mathrm{d}\omega\,,\ \vec{W} = \int\limits_0^\infty \vec{W}\mathrm{d}\omega\,,\ q_{R,n} = \int\limits_0^\infty q_{R,n,\omega}\mathrm{d}\omega\,,$

are the integral energy density, integral radiation flux, and integral hemispherical flux.

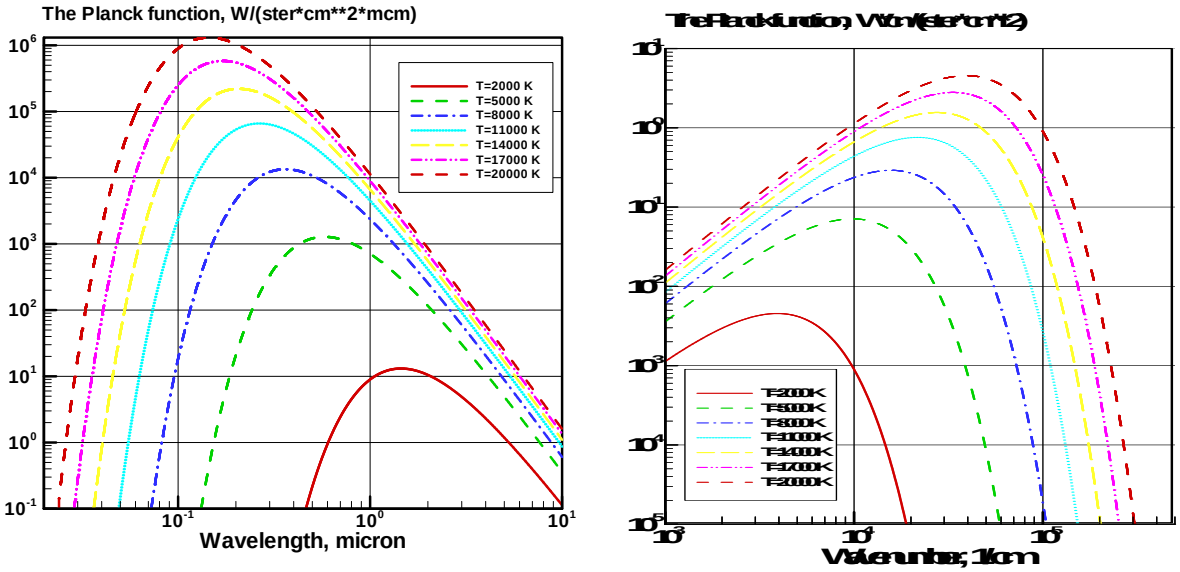

Figure 2.3: The wavelength (left) and wavenumber (right) dependence of the Planck function at different temperatures

The radiative energy balance in a gas and plasma can be calculated as follows:

$$\int\limits_{4\pi} \vec{\Omega}\cdot\nabla J\mathrm{d}\Omega = \int\limits_{4\pi} \kappa J_{b,\omega}\left[T\left(s\right)\right]\mathrm{d}\Omega - \int\limits_{4\pi} \kappa J_\omega\left(s,\vec{\Omega}\right)\mathrm{d}\Omega\,, \tag{3}$$

or

$$\nabla\cdot\vec{W}_\omega = 4\pi\kappa_\omega J_{b,\omega} - \kappa\int\limits_{4\pi} J_\omega\left(s,\vec{\Omega}\right)\mathrm{d}\Omega\,,$$

where the first summand in the right hand side corresponds to the spectral emission, and the second one corresponds to the spectral absorption.

If we integrate Equation (3) by spectrum, then

$$\left(\nabla\cdot\vec{W}\right) = 4\pi\mathrm{d}\omega - c\int\limits_0^\infty \kappa U\mathrm{d}\omega\,, \tag{4}$$

or

$$\left(\nabla\cdot\vec{W}\right) = 4\kappa_P\tilde{\sigma}T^4 - c\int\limits_0^\infty \kappa_\omega\, U_\omega\,\mathrm{d}\omega\ \text{, W/cm}^3,$$

where $\int J\mathrm{d}\omega = \dfrac{\tilde{\sigma}}{\pi}T$, $\tilde{\sigma} = 5.67\times10^{-12}$, $\dfrac{\mathrm{W}}{\mathrm{cm}^2\mathrm{K}^4}$ is the Stefan-Boltzmann constant;

$\kappa_P = \int \kappa J d\omega \Big/ \int J d\omega$ is the Planck mean absorption coefficient.

Other significant characteristics of radiation heat transfer are:

1) The group absorption coefficients are introduces as following:

$$\kappa_g = \kappa_{\Delta\omega} = \frac{1}{\Delta\omega}\int_{\Delta\omega} \kappa d\omega = \frac{1}{\Delta\omega}\sum_{i=1}^{N_{\Delta\omega_g}} \kappa \Delta\omega_i \quad \text{is the group absorption coefficient;} \tag{5}$$

$$\kappa_{P,g} = \frac{\pi}{\tilde{\sigma}T^4}\sum_{i=1}^{N_{\Delta\omega_g}} \kappa J \Delta\omega_i \quad \text{is the group Planck mean absorption coefficients;} \tag{6}$$

$$\kappa_P = \sum_{g=1}^{N_g} \kappa_{P,g}\,,$$

where $N_{\Delta\omega}$ is the number of the spectral points inside g-th spectral group, N_g is the number of the group, $\Delta\omega_i$ is the elementary spectral region. Actually, Equations (5) and (6) introduce the line-by-line model.

2) A photon mean free path

$$L_R = \frac{\pi}{4\tilde{\sigma}T^3}\int_0^\infty \frac{1}{\kappa_\omega}\frac{\partial J_{b,\omega}}{\partial T} d\omega, \text{cm}\,, \tag{8}$$

$$L_{R,g} = \frac{\pi}{4\tilde{\sigma}T^3}\sum_{i=1}^{N_{\Delta\omega_g}} \frac{1}{\kappa_{\Delta\omega_i}}\left(\frac{\partial J_{b,\omega}}{\partial T}\right)_i \Delta\omega_i\,, \quad L_R = \sum_{g=1}^{N_g} L_{R,g}\,.$$

3) The Rosseland mean absorption coefficients are calculated as following:

$$\kappa_{R,g} = \frac{1}{L_{R,g}}, \quad \kappa_R = \frac{1}{L_R}.$$

4) The radiative thermal conductivity is defined as

$$q_R = -\lambda_R \vec{\nabla} T, \quad \lambda_R = \frac{16}{3}\frac{1}{\kappa_R}\tilde{\sigma}T\,. \tag{9}$$

This approximation is correct only for $\tau_\omega \gg 1$, where $\tau_\omega = \int_0^L \kappa_\omega ds$ is the optical depth; L is the length of the optical path.

5) The spectral, group, and integral emissivities can be defined in the following form only for the LTE approximation:

$$Q_{em,\nu} = 4\pi\kappa J_{b,\nu}\frac{\text{W}}{\text{cm}^3\cdot\mu}, \quad Q_{\Delta\omega_g} = 4\kappa_{P,g}\sigma T\,, \quad Q_{em} = 4\kappa\tilde{\sigma}T^4, \frac{\text{W}}{\text{cm}^3}\,. \tag{10}$$

Because the Planck function is isotropic one, the integrated flux of the absolutely black body can be calculated as follows:

$$q_{b,n}(T)=\int_0^{\infty}\mathrm{d}\omega\int_0^{2\pi}\mathrm{d}\varphi\int_0^{\pi/2}J_{b\omega}\mathrm{Sin}\theta\mathrm{Cos}\theta\mathrm{d}\theta=\tilde{\sigma}T^4. \tag{11}$$

For estimation and comparison of emissivity of various mixes of high-temperature gases a spherical emissivity factor is used

$$\varepsilon_{\omega}(r,\Omega)=\frac{J_{\omega}(r,\Omega)}{J_{b\omega}(r)}. \tag{12}$$

In particular, the emissivity factor of a half-spherical homogeneous volume of a radius R can be calculated as

$$\varepsilon_{\omega,sph}=(\pi J_{b\omega})^{-1}\int_0^R\mathrm{d}r\int_0^{2\pi}\mathrm{d}\varphi\int_0^{\pi/2}\kappa_{\omega}J_{b\omega}\exp(-\kappa_{\omega}r)\mathrm{Cos}\theta\mathrm{Sin}\theta\,\mathrm{d}\theta=\frac{\varepsilon'_{\omega,sph}}{\pi J_{b\omega}}=1-\exp(-\kappa_{\omega}R). \tag{13}$$

The emissivity factor of a flat homogeneous layer is determined by the following expression

$$\varepsilon_{\omega,pl}=(\pi J_{b\omega})^{-1}\int_0^L\mathrm{d}x\int_0^{2\pi}\mathrm{d}\varphi\int_0^{\pi/2}\kappa_{\omega}J_{b\omega}\exp\left(-\frac{\kappa_{\omega}x}{\mathrm{Cos}\theta}\right)\mathrm{Sin}\theta\mathrm{d}\theta=\frac{\varepsilon'_{\omega,pl}}{\pi J_{b\omega}}=1-2E_3(\kappa_{\omega},L), \tag{14}$$

where $E_n(x)=\int_0^1\exp(-x/\mu)\mu^{n-2}\mathrm{d}\mu$ is the integro-exponential function of the n-th order, L is the depth of the flat layer.

An integral emissivity factors are calculated as following:

$$\varepsilon_{\Delta\omega}=\frac{1}{\tilde{\sigma}T^4}\int_{\Delta\omega}\varepsilon'_{\omega}\mathrm{d}\omega,\quad \varepsilon=\frac{1}{\tilde{\sigma}T^4}\int_0^{\infty}\varepsilon'_{\omega}\mathrm{d}\omega. \tag{15}$$

There is relation between spectral absorption coefficient κ_{ω} and spectral emission coefficient j_{ω} in the LTE conditions, which is based on the Kirchhoff law: $j_{\omega}=\kappa_{\omega}J_{b,\omega}$.

3.0 METHODS OF INTEGRATION OF RADIATION HEAT TRANSFER EQUATIONS

3.1 The P_N (Spherical Harmonic) approximation [2, 4]

A set of approximations to the equation of radiation transfer, which is capable of estimating the solution to the equation of transfer to within any desired accuracy criteria, is considered in the chapter. This is the so-called P_N-approximation of the spherical harmonic method, with N denoting the order of the approximation. For N infinite, the P_N-approximation is the exact solution to the radiation transfer equation.

The P_N-approximation will be considered for two calculation cases, which are of practical interest for aerospace applications.

1) Radiation heat transfer in infinite plane inhomogeneous layer with light-scattering media (1D radiation heat transfer problem).

2) Radiation heat transfer in axially symmetric two-dimensional volume (2D radiation heat transfer problem).

3.1.1 Plane-parallel calculation case

Let us consider radiation heat transfer equation for the 1D calculation case shown in Figure 3.1, which is described by the following equation:

$$\mu\frac{\partial J(\tau,\mu)}{\partial\tau}+J(\tau,\mu)=(1-\tilde{\omega})J_b(\tau)+\frac{\tilde{\omega}}{2}\int_{-1}^{1}\gamma(\mu',\mu)J(\tau,\mu')\,d\mu' \tag{1}$$

with the boundary conditions

$$\tau=0,\ \ \mu>0:\ \ J(0,\mu)=J_0^+(\mu), \tag{2}$$

$$\tau=\tau_H,\ \ \mu<0:\ \ J(\tau_H,\mu)=J_H^-(\mu). \tag{3}$$

where $J(\tau,\mu)$ is the spectral intensity of heat radiation (index of spectral dependence is omitted); τ is the spectral optical depth $d\tau=\kappa dx$; κ is the spectral absorption coefficient; $\mu=Cos\theta$; $\tilde{\omega}=\sigma/(\kappa+\sigma)$; σ is the spectral coefficient of scattering; γ is the scattering indicatrix; $J_b(\tau)$ is the spectral intensity of black body radiation. Intensities of radiation on boundaries $J_H^-(\mu)=J_\nu^-(\tau=\tau_H,\mu)$, $J_H^+(\mu)=J_\nu^+(\tau=0,\mu)$ are given for concrete calculation case.

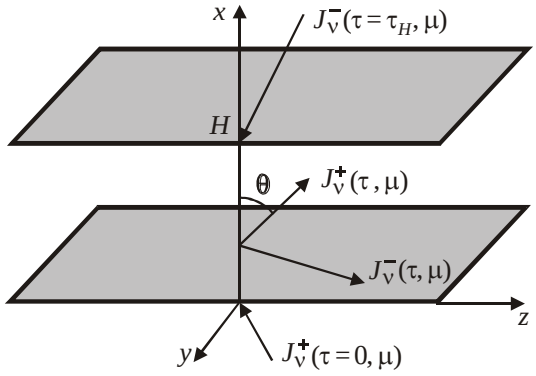

Figure 3.1: Schematic of radiation heat transfer in 1D geometry

It is assumed that radiation intensity may be presented in the following form:

$$J(\tau,\mu)=\sum_{m=0}^{\infty}\frac{2m+1}{4\pi}\varphi_m(\tau)P_m(\mu), \tag{4}$$

where $P_m(\mu)$ are the Legendre functions.

Let scattering indicatrix also may be presented in the form

$$\gamma(\mu',\mu)=\sum_{m=0}^{\infty}(2m+1)\gamma_m P_m(\mu)P_m(\mu'),\quad \gamma_0=1. \tag{5}$$

The Legendre functions have the ortogonality property:

$$\int_{-1}^{1}P_n(\mu)P_m(\mu)d\mu=\begin{cases}0, & m\neq n,\\ \dfrac{2}{2m+1}, & m=n\end{cases} \tag{6}$$

and these functions are associated also with the following recurrent formula:

$$\mu P_m(\mu) = \frac{mP_{m-1}(\mu) + (m+1)P_{m+1}(\mu)}{2m+1}. \tag{7}$$

The Legendre polynomials of low orders are:

$$\begin{aligned} &P_0(\mu) = 1, && P_1(\mu) = \mu, \\ &P_2(\mu) = \frac{1}{2}\left(3\mu^2 - 1\right), && P_3(\mu) = \frac{1}{2}\left(5\mu^3 - 3\mu\right), \\ &P_4(\mu) = \frac{1}{8}\left(35\mu^4 - 30\mu^2 + 3\right), && P_5(\mu) = \frac{1}{8}\left(63\mu^5 - 70\mu^3 + 15\mu\right). \end{aligned} \tag{8}$$

Substituting (4) and (5) into (1), and integrating with respect to total solid angle, one can obtain

$$\sum_{m=0}^{\infty} \frac{2m+1}{4\pi} P_m(\mu)\left[\mu \frac{d\varphi_m(\tau)}{d\tau} + \varphi_m(\tau)\right] = (1-\tilde{\omega}) J_b(\tau) + \tilde{\omega} \sum_{m=0}^{\infty} \frac{2m+1}{4\pi} \gamma_m P_m(\mu) \varphi_m(\tau),$$

and taking into account (7)

$$\sum_{m=0}^{\infty}\left[(m+1)\frac{d\varphi_{m+1}(\tau)}{d\tau} + m\frac{d\varphi_{m-1}(\tau)}{d\tau} + (2m+1)(1-\tilde{\omega}\gamma_m)\varphi_m(\tau) - 4\pi(1-\tilde{\omega}) J_b(\tau)\delta_{0,m}\right] P_m(\mu) = 0, \tag{9}$$

where $\delta_{0,m}$ is the Kronecker symbol.

Equation (9) must be satisfied at any μ, therefore

$$(m+1)\frac{d\varphi_{m+1}(\tau)}{d\tau} + m\frac{d\varphi_{m-1}(\tau)}{d\tau} + (2m+1)(1-\tilde{\omega}\gamma_m)\varphi_m(\tau) = 4\pi(1-\tilde{\omega}) J_b(\tau)\delta_{0,m}, \quad m = 0,1,2,\ldots \tag{10}$$

Unfortunately system of differential Equations (10) is not closed. At given *m*, each equation contains three functions: $\varphi_{m-1}(\tau), \varphi_m(\tau), \varphi_{m+1}(\tau)$.

For closing the infinite system of equations it is agreed that at $m \geq N$

$$\frac{d\varphi_{m+1}}{d\tau} = 0, \qquad m = N, N+1, \ldots, \tag{11}$$

where *N* is the order of the approximation. The system of Equations (10) is called as P_N approximation of the spherical harmonics expansion, or simply P_N approximation.

Most simple P_1 approximation is extensively used in radiative heat transfer theory. In this case ($N = 1$)

$$\frac{d\varphi_1(\tau)}{d\tau} + (1-\tilde{\omega}\gamma_0)\varphi_0(\tau) = 4\pi(1-\tilde{\omega}) J_b(\tau), \tag{12}$$

$$\frac{d\varphi_0(\tau)}{d\tau} + 3(1-\tilde{\omega}\gamma_1)\varphi_1(\tau) = 0, \tag{13}$$

where γ_0 and γ_1 are the coefficients in expansion of scattering indicatrix

$$\gamma(\mu',\mu)=\sum_{m=0}^{1}(2m+1)\gamma_m P_m(\mu)P_m(\mu')=1+3\gamma_1\mu\mu'. \tag{14}$$

This is so called linearly-non-isotropic indicatrix. For isotropic scattering ($\gamma_0=1;\gamma_m=0$ at $m\geq 1$) Equations (12) and (13) have the following form:

$$\frac{d\varphi_1(\tau)}{d\tau}+(1-\tilde{\omega})\varphi_0(\tau)=4\pi(1-\tilde{\omega})J_b(\tau), \tag{15}$$

$$\frac{d\varphi_0(\tau)}{d\tau}+3\varphi_1(\tau)=0. \tag{16}$$

If we take into account that

$$\varphi_0(\tau)=2\pi\int_{-1}^{1}J(\tau,\mu)d\mu=G(\tau)=cU(\tau),$$

$$\varphi_1(\tau)=2\pi\int_{-1}^{1}\mu J(\tau,\mu)d\mu=W(\tau),$$

because in the P_1 approximation

$$J(\tau,\mu)=\frac{1}{4\pi}\varphi_0(\tau)P_0(\mu)+\frac{3}{4\pi}\varphi_1(\tau)P_1(\mu),$$

$$P_0(\mu)=1,\quad P_1(\mu)=\mu,$$

then finally system of equations for radiation transfer in plane-parallel isotropically scattering media takes the form

$$\frac{dW(\tau)}{d\tau}+(1-\tilde{\omega}\gamma_0)G(\tau)=4\pi(1-\tilde{\omega})J_b(\tau), \tag{17}$$

$$W(\tau)=-\frac{1}{3(1-\tilde{\omega}\gamma_1)}\frac{dG(\tau)}{d\tau} \tag{18}$$

or $$-\frac{1}{3(1-\tilde{\omega}\gamma_1)}\frac{d^2G(\tau)}{d\tau^2}+(1-\tilde{\omega}\gamma_0)G(\tau)=4\pi(1-\tilde{\omega})J_b(\tau)$$

or $$-\frac{1}{3(1-\tilde{\omega}\gamma_1)}\frac{d^2U(\tau)}{d\tau^2}+(1-\tilde{\omega}\gamma_0)U(\tau)=(1-\tilde{\omega})U_b(\tau),$$

where $U_b(\tau)=\frac{4\pi}{c}J_b$.

Taking into account boundary conditions (2) and (3), one can get the following boundary-value problem:

$$\frac{d^2U(\tau)}{d\tau^2}=3(1-\tilde{\omega}\gamma_0)(1-\tilde{\omega}\gamma_1)U(\tau)-3(1-\tilde{\omega})(1-\tilde{\omega}\gamma_1)U_b(\tau), \tag{19}$$

$$x=0: \quad -\frac{c}{3\kappa}\frac{\mathrm{d}U}{\mathrm{d}x}\bigg|_{x=0} = 2\pi J_H^+ - \frac{c}{2}U(x=0),$$

$$x=H: \quad -\frac{c}{3\kappa}\frac{\mathrm{d}U}{\mathrm{d}x}\bigg|_{x=H} = -2\pi J_0^- + \frac{c}{2}U(x=H).$$

where $$\mathrm{d}\tau = \beta \mathrm{d}x = (\kappa+\sigma)\mathrm{d}x.$$

Let us consider some numerical solutions of the boundary-value problem.

Figures 3.2–3.4 show distributions of radiation energy density U, the x-projection of radiation flux W, and divergency of radiation flux Q_R in plane-parallel isotropically scattering layer with temperature distribution shown in Figure 3.5.
Note that once a boundary-value problem (19) has been integrated, the x-projection of radiation flux W is calculated with use of Equation (18). Divergence of radiation flux can be calculated by the following two manners:

- A formal differentiation of Equation (18) leads to the formula

$$\nabla\cdot\mathbf{W} = -\frac{1}{3(1-\tilde{\omega}\gamma_1)}\frac{\mathrm{d}^2 G(\tau)}{\mathrm{d}\tau^2};$$

- From Equation (17) one can get

$$\nabla\cdot\mathbf{W} = 4\pi(1-\tilde{\omega})J_b(\tau) - (1-\tilde{\omega}\gamma_0)G(\tau).$$

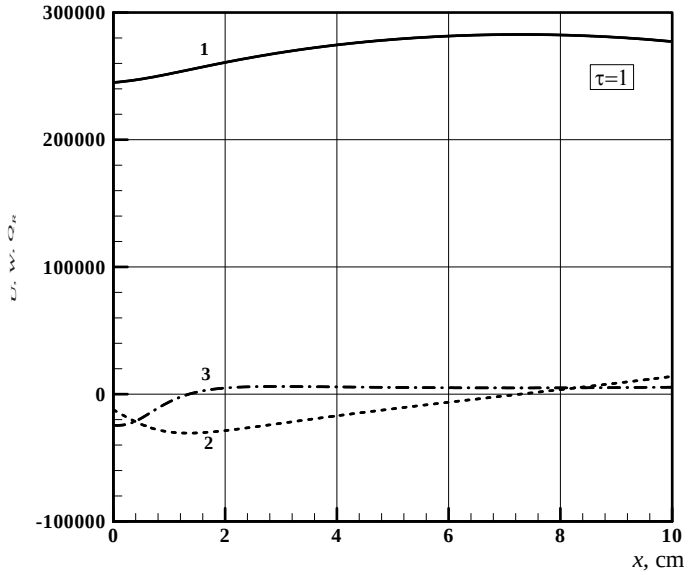

Figure 3.2: Volume density of radiative energy (1, U in J/cm^3), radiation flux (2, W in W/cm^2), and divergency of radiation flux (3, Q_R in W/cm^3); the optical depth $\tau = 1$

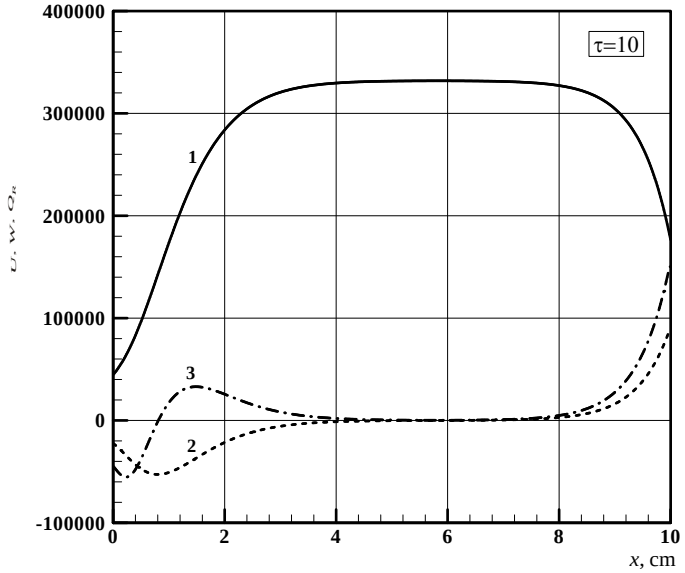

Figure 3.3: Volume density of radiative energy (1, *U* in J/cm^3), radiation flux (2, *W* in W/cm^2), and divergency of radiation flux (3, Q_R in W/cm^3); the optical depth $\tau = 10$

Figure 3.4 shows distributions of the functions for $\tau = 1$, $\sigma = 10\ \text{cm}^{-1}$.

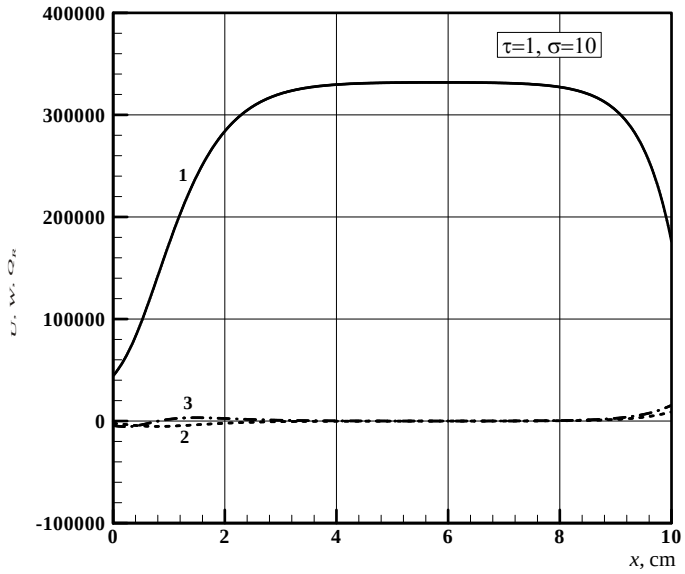

Figure 3.4: Volume density of radiative energy (1, *U* in J/cm^3), radiation flux (2, *W* in W/cm^2), and divergency of radiation flux(3, Q_R in W/cm^3); the optical depth $\tau = 1$, $\sigma = 10$ см$^{-1}$

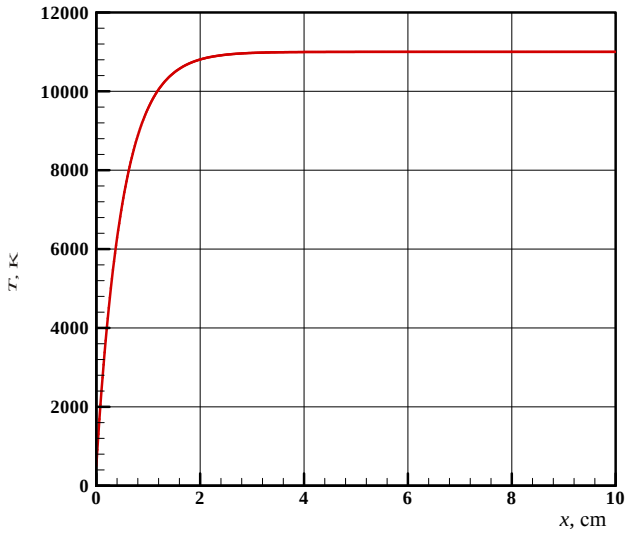

Figure 3.5: Temperature distribution in plane-parallel layer

3.1.2 Two-dimensional radiation heat transfer

Radiation transfer is considered here for axially symmetric cylindrical volume of radius R and length H (Figure 3.6). Such a schematic is in common use in different aerospace applications, for example, at study of entry space vehicles, rocket engines, plasma generators, electro-discharge devices, etc.

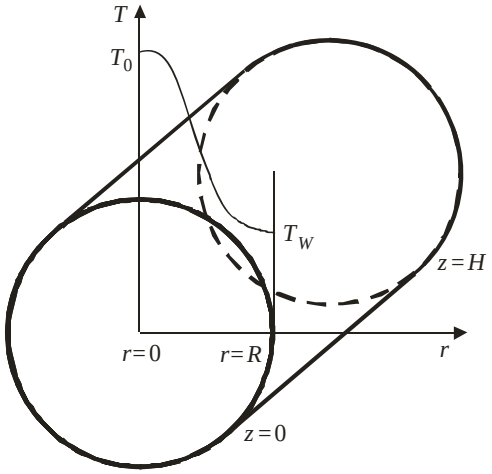

Figure 3.6: Schematic of two-dimensional axially symmetric problem

Radiation transfer equation in two-dimensional axially symmetric geometry has the following form:

$$\sqrt{1-\mu^2}\left[\gamma\frac{\partial J(r,z,\mu,\gamma)}{\partial r}+\frac{1-\gamma^2}{r}\frac{\partial J(r,z,\mu,\gamma)}{\partial\gamma}\right]+\mu\frac{\partial J(r,z,\mu,\gamma)}{\partial z}+\kappa J(r,z,\mu,\gamma)=\kappa J_b(r,z), \qquad (20)$$

and corresponding to Figure 3.6 boundary conditions are:

$$z=0,\ \ \mu>0:\ \ J(r,0,\mu,\gamma)=J_0^+(r,\mu,\gamma),$$

$$z = H\,,\ \ \mu < 0:\ \ J\left(r,H,\mu,\gamma\right) = J_0^-\left(r,\mu,\gamma\right),$$

$$r = R\,,\ \ \gamma < 0:\ \ J\left(R,z,\mu,\gamma\right) = J_R^-\left(z,\mu,\gamma\right),$$

where $\mu = \cos\theta,\ \gamma = \cos\varphi$; $J_0^+\left(r,\mu,\gamma\right),\ J_0^-\left(r,\mu,\gamma\right),\ J_R^-\left(z,\mu,\gamma\right)$ are the boundary intensities.

Let us suppose that the radiation intensity $J = J\left(R,z,\mu,\gamma\right)$ can be expanded into the spherical harmonic series:

$$J = \sum_{l=0}^{\infty}\left[\frac{1}{2}\alpha_{l,0}P_l\left(\mu\right) + \sum_{m=1}^{l}P_l^m\left(\mu\right)\left(\alpha_{l,m}\cos m\varphi + \beta_{l,m}\sin m\varphi\right)\right], \tag{21}$$

where $\alpha_{l,m}$ and $\beta_{l,m}$ are the unknown functions of spatial coordinates *r* and *z*; $P_l^m\left(\mu\right)$ are the associated Legendre functions. These functions have the following orthonormality relations [5].

$$\int_{-1}^{1}P_l^m P_{l'}^m\,\mathrm{d}\mu = \frac{2}{2l+1}\frac{\left(l+m\right)!}{\left(l-m\right)!}\delta_{ll'}\,, \tag{22}$$

$$\int_0^1\left(P_l^m\right)^2\mathrm{d}\mu = \frac{1}{2l+1}\frac{\left(l+m\right)!}{\left(l-m\right)!},$$

where $\delta_{ll'}$ is the Kronecker symbol.

The following recursion relations are also can be taken into account:

$$\left(2l+1\right)\mu P_l^m\left(\mu\right) = \left(l-m+1\right)P_{l+1}^m\left(\mu\right) + \left(l+m\right)P_{l-1}^m\left(\mu\right),$$

$$0 \le m \le l-1; \tag{23}$$

$$\left(2l+1\right)\sqrt{1-\mu^2}\,P_l^{m-1}\left(\mu\right) = P_{l+1}^m\left(\mu\right) - P_{l-1}^m\left(\mu\right),$$

$$0 \le m \le l-1; \tag{24}$$

$$\left(2l+1\right)\sqrt{1-\mu^2}\,P_l^{m+1}\left(\mu\right) = \left(l+m\right)\left(l+m+1\right)P_{l-1}^m\left(\mu\right) - \left(l-m\right)\left(l-m+1\right)P_{l+1}^m\left(\mu\right),$$

$$0 \le m \le l-1. \tag{25}$$

The moment procedure, which is well known in kinetic theory, is used for derivation of the P_N approximation equations. An application of integral operator

$$\Lambda_{l,m}\{\ \} = \int_0^{2\pi}\int_{-1}^{1}\{\ \}P_l^m\left(\mu\right)\left(\alpha_{l,m}\cos m\varphi + \beta_{l,m}\sin m\varphi\right)\mathrm{d}\varphi\,\mathrm{d}\mu\,,$$

$$l = 0,1,2,\ldots,\ \ m = -l,-l+1,\ldots,0,\ldots,l-1,l\,, \tag{26}$$

on Equation (20) leads to infinite system of ordinary differential equations, which takes the following form at fixation of $l = N$:

$$\frac{1+\delta_{m,0}}{2(2l+1)}\left[\frac{\partial F_{l+1}^{m+1}}{\partial r}+(m+1)\frac{F_{l+1}^{m+1}}{r}\right]-\frac{1+\delta_{m,0}}{2(2l+1)}\left[\frac{\partial F_{l-1}^{m+1}}{\partial r}+(m+1)\frac{F_{l-1}^{m+1}}{r}\right]+$$

$$+\frac{(l+m-1)(l+m)(1-\delta_{m,0})}{2(2l+1)}\left[\frac{\partial F_{l-1}^{m-1}}{\partial r}-(m-1)\frac{F_{l-1}^{m-1}}{r}\right]-$$

$$-\frac{(l-m+1)(l-m+2)(1-\delta_{m,0})}{2(2l+1)}\left[\frac{\partial F_{l+1}^{m-1}}{\partial r}-(m-1)\frac{F_{l+1}^{m-1}}{r}\right]-$$

$$+\frac{l-m+1}{2l+1}\frac{\partial F_{l+1}^{m}}{\partial z}+\frac{l+m}{2l+1}\frac{\partial F_{l-1}^{m}}{\partial z}+\kappa F_l^m=4\pi\kappa J_b\delta_{l,0}\delta_{m,0},\quad 0\le l<N, \tag{27}$$

$$-\frac{1+\delta_{m,0}}{2(2N+1)}\left[\frac{\partial F_{N-1}^{m+1}}{\partial r}+(m+1)\frac{F_{N-1}^{m+1}}{r}\right]+$$

$$+\frac{(N+m-1)(N+m)(1-\delta_{m,0})}{2(2N+1)}\left[\frac{\partial F_{N-1}^{m-1}}{\partial r}-(m-1)\frac{F_{N-1}^{m-1}}{r}\right]+\frac{N+m}{2N+1}\frac{\partial F_{N-1}^{m}}{\partial z}+\kappa F_N^m=0,\ \ l=N, \tag{28}$$

where
$$F_l^m=\int_{-1}^{1}\int_{0}^{2\pi}JP_l^m(\mu)\cos m\varphi\,d\varphi\,d\mu. \tag{29}$$

Some special cases are considered later.

1) P1-approximation of radiation transfer equation for the plane-parallel layer.

In this case $N=1$, and $\partial/\partial r=0$, therefore

- $l=0,\quad m=0$

  $\dfrac{\partial F_1^0}{\partial z}+\kappa F_0^0=4\pi\kappa J_b;$

- $l=N=1,\qquad m=0$

  $\dfrac{1}{3}\dfrac{\partial F_0^0}{\partial z}+\kappa F_1^0=0;$

- $l=N=1,\qquad m=1$

  $\dfrac{2}{3}\dfrac{\partial F_0^1}{\partial z}+\kappa F_1^1=0;$

In the case under consideration must be satisfied conditions of axially symmetry:

$$F_1^1=F_2^1=0,$$

because they contain integral over even on φ function

$$\int_0^{2\pi} J\cos\varphi d\varphi = 0 .$$

In addition $P_l^m(\mu) = 0$ at $l < m$,

therefore $F_0^1 = F_0^2 = 0$.

Finally one can get the desired system of equation:

$$\frac{\partial F_1^0}{\partial z} + \kappa F_0^0 = 4\pi\kappa J_b , \tag{30}$$

$$\kappa F_1^0 = -\frac{1}{3}\frac{\partial F_0^0}{\partial z} , \tag{31}$$

where $$F_0^0 = \int_{-1}^{1}\int_0^{2\pi} JP_0^0(\mu)d\mu d\varphi = 2\pi\int_{-1}^{1} Jd\mu = cU , \tag{32}$$

$$F_1^0 = \int_{-1}^{1}\int_0^{2\pi} JP_1^0(\mu)d\mu d\varphi = 2\pi\int_{-1}^{1} J\mu d\mu = W . \tag{33}$$

Note that these equations agree with Equations (12) and (13) at $\tilde{\omega}$.

2) P_1-approximation of radiation transfer equation for 1D cylindrical case.

In this case $N = 1$, and $\partial/\partial z = 0$, therefore

- $l = 0, \quad m = 0$

  $\frac{\partial F_1^1}{\partial r} + \frac{F_1^1}{r} + \kappa F_0^0 = 4\pi\kappa J_b ;$

- $l = N = 1, \qquad m = 0$

  $\frac{2}{2\cdot 3}\left(\frac{\partial F_0^1}{\partial r} + \frac{F_0^1}{r}\right) + \kappa F_1^0 = 0 ;$

- $l = N = 1, \qquad m = 1$

  $\frac{1}{2\cdot 3}\left(\frac{\partial F_0^2}{\partial r} + 2\frac{F_0^2}{r}\right) + \frac{2}{2\cdot 3}\frac{\partial F_0^0}{\partial r} + \kappa F_1^1 = 0 .$

Conditions of axial symmetry allow to get final system of the P_1-approximation for the 1D cylindrical case:

$$\frac{\partial F_1^1}{\partial r} + \frac{F_1^1}{r} + \kappa F_0^0 = 4\pi\kappa J_b ,$$

$$\frac{1}{3}\frac{\partial F_0^0}{\partial r}+\kappa F_1^1=0\,.$$

Let us take into account that

$$F_0^0=\int_{-1}^{1}\int_{0}^{2\pi} JP_0^0(\mu)\,d\mu d\varphi=2\pi\int_{-1}^{1} J d\mu=cU\,,$$

$$F_1^1=\int_{-1}^{1}\int_{0}^{2\pi} JP_1^1(\mu)\cos\varphi d\mu d\varphi=W\,,$$

therefore

$$\frac{1}{r}\frac{\partial}{\partial r}(rW)+c\kappa U=c\kappa U_b\,,$$

$$\frac{c}{3\kappa}\frac{\partial U}{\partial r}+W=0\,.$$

A boundary-value problem for 1D cylindrical volume with black body surfaces at temperature T_W is formulated in the following form:

$$\frac{1}{r}\frac{\partial}{\partial r}\left(\frac{r}{3\kappa}\frac{\partial U}{\partial r}\right)=\kappa(U-U_b),\tag{34}$$

$$r=0:\quad \frac{\partial U}{\partial r}=0;\tag{35}$$

$$r=R:\quad \frac{2}{3\kappa}\frac{\partial U}{\partial r}=U_b(T_W)-U\,.\tag{36}$$

2) P_1-approximation for two-dimensional cylindrical geometry.

In this case $N=1$, and with consideration of conditions of axially symmetry, one can derive

$$\frac{1}{r}\frac{\partial rF_1^1}{\partial r}+\frac{\partial F_1^0}{\partial z}+\kappa F_0^0=4\pi\kappa J_b;$$

$$F_1^0=-\frac{1}{3\kappa}\frac{\partial F_0^0}{\partial z},$$

$$F_1^1=-\frac{1}{3\kappa}\frac{\partial F_0^0}{\partial r}\,.$$

Because

$$F_0^0=\int_{-1}^{1}\int_{0}^{2\pi} JP_0^0(\mu)\,d\mu d\varphi=2\pi\int_{-1}^{1} J d\mu=cU\,,$$

$$F_1^0=\int_{-1}^{1}\int_{0}^{2\pi} JP_1^0(\mu)\cos\varphi d\mu d\varphi=W_z\,,$$

$$F_1^1 = \int_{-1}^{1}\int_{0}^{2\pi} JP_1^1(\mu)\cos\varphi \, d\mu d\varphi = W_r,$$

then the system of equations takes more opaque for:

$$\frac{1}{r}\frac{\partial}{\partial r}(rW_r) + \frac{\partial W_z}{\partial z} + c\kappa U = 4\pi\kappa J_b, \tag{37}$$

$$W_z = -\frac{c}{3\kappa}\frac{\partial U}{\partial z}, \tag{38}$$

$$W_r = -\frac{c}{3\kappa}\frac{\partial U}{\partial r}. \tag{39}$$

For closed cylindrical volume with black surfaces at temperature T_w there is the following boundary-value problem:

$$\frac{1}{r}\frac{\partial}{\partial r}\left(\frac{r}{3\kappa}\frac{\partial U}{\partial r}\right) + \frac{\partial}{\partial z}\left(\frac{r}{3\kappa}\frac{\partial U}{\partial z}\right) = \kappa(U - U_b), \tag{40}$$

$$r = 0: \ \frac{\partial U}{\partial r} = 0, \qquad z = 0: \ \frac{2}{3\kappa}\frac{\partial U}{\partial z} = U - U_b,$$

$$r = R: \ \frac{2}{3\kappa}\frac{\partial U}{\partial r} = U_b - U, \qquad z = H: \ \frac{2}{3\kappa}\frac{\partial U}{\partial z} = U_b - U.$$

3) P_3-approximation for 2D cylindrical geometry

In this case $N = 3$, and

- $l = 0, \quad m = 0$

$$\frac{1}{r}\frac{\partial r F_1^1}{\partial r} + \frac{\partial F_1^0}{\partial z} + \kappa F_0^0 = 4\pi\kappa J_b,$$

- $l = 1, \quad m = 0$

$$\frac{1}{3}\frac{1}{r}\frac{\partial r F_2^1}{\partial r} + \frac{2}{3}\frac{\partial F_2^0}{\partial z} + \frac{1}{3}\frac{\partial F_0^0}{\partial z} + \kappa F_1^0 = 0,$$

- $l = 1, \quad m = 1$

$$\frac{1}{6}\left(\frac{\partial F_2^2}{\partial r} + 2\frac{F_r^2}{r}\right) + \frac{1}{3}\frac{\partial F_0^0}{\partial r} - \frac{1}{3}\frac{\partial F_2^0}{\partial r} + \frac{1}{3}\frac{\partial F_2^1}{\partial z} + \kappa F_1^1 = 0,$$

- $l = 2, \quad m = 0$

$$\frac{1}{5}\frac{1}{r}\frac{\partial r F_3^1}{\partial r} - \frac{1}{5}\frac{1}{r}\frac{\partial r F_1^1}{\partial r} + \frac{3}{5}\frac{\partial F_3^0}{\partial z} + \frac{2}{5}\frac{\partial F_1^0}{\partial z} + \kappa F_2^0 = 0,$$

- $l = 2, \quad m = 1$

$$\frac{1}{10}\left(\frac{\partial F_3^2}{\partial r}+2\frac{F_3^2}{r}\right)+\frac{3}{5}\frac{\partial F_1^0}{\partial r}-\frac{3}{5}\frac{\partial F_3^0}{\partial r}+\frac{2}{5}\frac{\partial F_3^1}{\partial z}+\frac{3}{5}\frac{\partial F_1^1}{\partial z}+\kappa F_2^1=0,$$

- $l=2,\quad m=2$

$$\frac{1}{10}\left(\frac{\partial F_3^3}{\partial r}+3\frac{F_3^3}{r}\right)+\frac{12}{10}\frac{\partial F_1^1}{\partial r}-\frac{1}{5}\frac{\partial F_3^1}{\partial r}+\frac{1}{5}\frac{\partial F_3^2}{\partial z}+\kappa F_2^2=0,$$

- $l=N=3,\qquad m=0$

$$-\frac{1}{7}\frac{1}{r}\frac{\partial rF_2^1}{\partial r}+\frac{3}{7}\frac{\partial F_2^0}{\partial z}+\kappa F_3^0=0,$$

- $l=N=3,\qquad m=1$

$$-\frac{1}{14}\left(\frac{\partial F_2^2}{\partial r}+2\frac{F_2^2}{r}\right)+\frac{12}{14}\frac{\partial F_2^0}{\partial r}+\frac{4}{7}\frac{\partial F_2^1}{\partial z}+\kappa F_3^1=0,$$

- $l=N=3,\qquad m=2$

$$\frac{20}{14}\left(\frac{\partial F_2^1}{\partial r}-\frac{F_2^1}{r}\right)+\frac{5}{7}\frac{\partial F_2^2}{\partial z}+\kappa F_3^2=0,$$

- $l=N=3,\qquad m=3$

$$\frac{30}{14}\left(\frac{\partial F_2^2}{\partial r}-2\frac{F_2^2}{r}\right)+\kappa F_3^3=0.$$

Further simplification of the system is connected with the use of properties of axial symmetry.

3.1.3 Formulation of boundary conditions for P_N-approximation

Two kinds of boundary conditions are used as a rule for solving P_N-equations.

The first one is the Mark boundary conditions [6]. Mark suggested that boundary conditions for P_N-approximation must be satisfied at angles corresponded to roots of the Legendre functions:

$$P_{N+1}(\mu)=0. \tag{41}$$

As an example, for the following boundary conditions:

$$\begin{aligned}&\tau=0, \quad \mu>0: \quad J(0,\mu)=J^+(\mu),\\ &\tau=\tau_H, \quad \mu<0: \quad J(\tau_H,\mu)=J^-(\mu)\end{aligned}$$

the Mark boundary conditions are formulated in the following form:

$$\begin{aligned}&\tau=0, \quad \mu>0: \quad J(0,\mu_i)=J^+(\mu_i),\\ &\tau=\tau_H, \quad \mu<0: \quad J(\tau_H,-\mu_i)=J^-(-\mu_i),\end{aligned} \tag{42}$$

where μ_i are the positive roots of Equation (41).

For the P_1-approximation boundary conditions (42) are given at:

$$P_2(\mu) = 3\mu_*^2 - 1 = 0,$$

that is at $\mu_* = 1/\sqrt{3}$.

If the radiation transfer problem is solved relative to volume density *U*, then

$$J(\tau,\mu) = \frac{c}{4\pi}\left[U(\tau) - \mu\frac{\mathrm{d}U(\tau)}{\mathrm{d}\tau}\right],$$

and the boundary conditions are

$$\tau = 0: \quad J^+(\mu_*) = \frac{c}{4\pi}\left[U(\tau) - \frac{1}{\sqrt{3}}\frac{\mathrm{d}U(\tau)}{\mathrm{d}\tau}\right], \tag{43}$$

$$\tau = \tau_H: \quad J^-(\mu_*) = \frac{c}{4\pi}\left[U(\tau) + \frac{1}{\sqrt{3}}\frac{\mathrm{d}U(\tau)}{\mathrm{d}\tau}\right]. \tag{44}$$

The second kind of boundary conditions was suggested by R. Marshak [7].

If physical boundary conditions are given in the form

$$\tau = 0, \quad \mu > 0: \quad J(0,\mu) = J^+(\mu),$$

$$\tau = \tau_H, \quad \mu < 0: \quad J(\tau_H,\mu) = J^-(\mu),$$

then averaged moments of boundary intensities are calculated as following:

$$M_i^+ = \int_0^1 J^+(\mu)\mu^{2i-1}\mathrm{d}\mu, \quad \mu > 0, \tag{45}$$

$$M_i^- = \int_{-1}^0 J^-(\mu)\mu^{2i-1}\mathrm{d}\mu, \quad \mu < 0, \tag{46}$$

$$i = 1,2,\ldots,(N+1)/2.$$

For example, in the P_1-approximation for plane-parallel layer

$$J(\tau,\mu) = \frac{c}{4\pi}\left[U(\tau) - \mu\frac{\mathrm{d}U(\tau)}{\mathrm{d}\tau}\right],$$

and the Marshak boundary conditions are formulated in the form

$$M_1^+(\tau = 0) = \frac{c}{4\pi}\left[U(\tau) - \frac{1}{2}\frac{\mathrm{d}U(\tau)}{\mathrm{d}\tau}\right]_{\tau=0}, \tag{47}$$

$$M_1^-\left(\tau=\tau_H\right)=\frac{c}{4\pi}\left[U\left(\tau\right)+\frac{1}{2}\frac{\mathrm{d}U\left(\tau\right)}{\mathrm{d}\tau}\right]_{\tau=\tau_H}. \tag{48}$$

3.1.4 The P_1-approximation for arbitrary geometry

In the general case the radiation intensity is expanded into spherical harmonics series:

$$J_\nu\left(\mathbf{r},\boldsymbol{\Omega}\right)=\sum_{n=0}^{\infty}\left(2n+1\right)\sum_{m=-n}^{n}\frac{1}{2\pi\left(1+\delta_{0,m}\right)}\frac{\left(n-|m|\right)!}{\left(n+|m|\right)!}\varphi_{nm}\left(\mathbf{r}\right)Y_n^m\left(\mu,\psi\right), \tag{49}$$

where Y_n^m are the spherical functions, which are expressed in terms of associated Legendre polynomials

$$\begin{gathered}Y_n^m\left(\mu,\psi\right)=P_n^{(m)}\left(\mu\right)\sin m\psi,\quad m>0,\\ Y_n^{-m}\left(\mu,\psi\right)=P_n^{(m)}\left(\mu\right)\cos m\psi,\quad m\geq 0,\\ -1\leq\mu\leq 1,\quad 0\leq\psi\leq 2\pi,\end{gathered} \tag{50}$$

where $\delta_{0,m}$ is the Kronecker symbol.

The P_1-approximation is in common use in the radiation gasdynamic. To formulate equations of the approximation for arbitrary geometry we consider radiation heat transfer equation for non-scattering medium in local thermodynamic equilibrium

$$\boldsymbol{\Omega}\cdot\nabla J_\nu\left(\mathbf{r},\boldsymbol{\Omega}\right)+\kappa_\nu\left(\mathbf{r}\right)J_\nu\left(\mathbf{r},\boldsymbol{\Omega}\right)=\kappa_\nu\left(\mathbf{r}\right)J_{b,\nu}\left(\mathbf{r}\right). \tag{51}$$

Leaving in expansion (59) only two first terms one can get the following representation of intensity

$$J_\nu\left(\mathbf{r},\boldsymbol{\Omega}\right)=\left[\varphi_{1,\nu}\left(\mathbf{r}\right)+\boldsymbol{\varphi}_{2,\nu}\left(\mathbf{r}\right)\cdot\boldsymbol{\Omega}\right]/4\pi, \tag{52}$$

where $\varphi_{1,\nu}(\mathbf{r})$, $\boldsymbol{\varphi}_{2,\nu}(\mathbf{r})$ are the unknown functions.

Physical meaning of the functions is clearly defined at integration of radiation intensity over all solid angle:

$$\int_{4\pi}J_\nu\left(\mathbf{r},\boldsymbol{\Omega}\right)\mathrm{d}\Omega=\varphi_{1,\nu}\left(\mathbf{r}\right)=cU_\nu\left(\mathbf{r}\right), \tag{53}$$

$$\int_{4\pi}\boldsymbol{\Omega}J_\nu\left(\mathbf{r},\boldsymbol{\Omega}\right)\mathrm{d}\Omega=\boldsymbol{\varphi}_{2,\nu}\left(\mathbf{r}\right)=\mathbf{W}_\nu\left(\mathbf{r}\right). \tag{54}$$

So, in the P_1-approximation radiation intensity can be presented in the form

$$J_\nu\left(\mathbf{r},\boldsymbol{\Omega}\right)=\left[cU_\nu\left(\mathbf{r}\right)+3\mathbf{W}_\nu\left(\mathbf{r}\right)\boldsymbol{\Omega}\right]/4\pi. \tag{55}$$

The first equation of the required system is obtained by integration of radiation heat transfer Equation (51) over solid angle:

$$\nabla\cdot\mathbf{W}_\nu\left(\mathbf{r}\right)+\kappa_\nu\left(\mathbf{r}\right)cU_\nu\left(\mathbf{r}\right)=\kappa_\nu\left(\mathbf{r}\right)cU_{b,\nu}\left(\mathbf{r}\right), \tag{56}$$

where $$cU_{b,\nu}(\mathbf{r}) = \int_{4\pi} J_{b,\nu}(\mathbf{r})\,\mathrm{d}\Omega .$$

The second equation can be obtained after integration of Equation (51) with $\vec{\Omega}$:

$$\mathbf{W}_\nu(\mathbf{r}) = -\frac{1}{3\kappa_\nu(\mathbf{r})}\nabla U_\nu(\mathbf{r}) . \tag{57}$$

Relation (57) shows that radiation flux is proportional to gradient of volume density of radiative energy. Coefficient $D = 1/3\kappa_\nu(\mathbf{r})$ is called as radiation diffusion coefficient.

Equations (56) and (57) can be presented in the following form:

$$-\nabla\frac{1}{3\kappa_\nu(\mathbf{r})}\nabla U_\nu(\mathbf{r}) + \kappa_\nu(\mathbf{r})cU_\nu(\mathbf{r}) = \kappa_\nu(\mathbf{r})cU_{b,\nu}(\mathbf{r}) . \tag{58}$$

Typical boundary conditions in arbitrary geometry for the P_1-approximation are:

1) No external radiation at surfaces:

$J_\nu(\mathbf{r},\boldsymbol{\Omega}) = 0$, at $(\boldsymbol{\Omega}\cdot\mathbf{n}) < 0$, where $\mathbf{n}$ is the unit normal to surface *s*.

In this case

$$W_{\nu n}(\mathbf{r}) = \left(\mathbf{n}\cdot\mathbf{W}_\nu(\mathbf{r})\right)_s = -\frac{c}{2}U_\nu(\mathbf{r}) \tag{59}$$

or $$\frac{2}{3}c\kappa_\nu^{-1}(\mathbf{r})\nabla U_\nu(\mathbf{r})\Big|_s = -U_\nu(\mathbf{r}) . \tag{60}$$

2) Axial symmetry for cylindrical geometry or central symmetry for spherical geometry:

$$\mathbf{r}^\circ W_\nu(\mathbf{r}) = 0 , \tag{61}$$

where $\mathbf{r}^\circ$ is the unit vector in radial direction. Relation (61) can be rewritten:

$$\frac{\partial U_\nu(\mathbf{r})}{\partial r} = 0 .$$

It is of great practical interest to consider equations of the P_1-approximation in the cases of the extreme small and extreme large optical depths.

1. Approximation of optically thin medium.

From exact equation

$$\nabla\cdot\mathbf{W}_\nu(\mathbf{r}) = \kappa_\nu(\mathbf{r})c\left[U_{b,\nu}(\mathbf{r}) - U_\nu(\mathbf{r})\right] . \tag{62}$$

at $\tau_\nu \ll 1$ one can get (no external radiation)

$$\nabla\mathbf{W}_\nu(\mathbf{r}) = c\kappa_\nu(\mathbf{r})U_{b,\nu}(\mathbf{r}) . \tag{63}$$

Upon integrating of Equation (63) with respect to radiation frequency we obtain the association of integral divergency with the Planck integral coefficient:

$$\int_0^\infty \nabla \mathbf{W}_\nu(\mathbf{r})\,d\nu = \nabla \mathbf{W}(\mathbf{r}) = 4\pi\kappa_P(\mathbf{r})\sigma T^4(\mathbf{r}), \tag{64}$$

where

$$\kappa_P(\mathbf{r}) = \frac{c\int_0^\infty \kappa_\nu(\mathbf{r})U_{b,\nu}(\mathbf{r})\,d\nu}{\int_0^\infty\int_{4\pi} J_{b,\nu}(\mathbf{r})\,d\Omega\,d\nu} = \frac{\int_0^\infty \kappa_\nu(\mathbf{r})J_{b,\nu}(\mathbf{r})\,d\nu}{\int_0^\infty J_{b,\nu}(\mathbf{r})\,d\nu}.$$

2. Approximation of optically thick medium.

In this case

$$U_\nu(\mathbf{r}) \approx U_{b,\nu}(\mathbf{r}). \tag{65}$$

Note that in this case calculation of $\nabla\cdot\vec{W}_\nu(\vec{r})$ by Equation (56) may be in error because values $U_{b,\nu}(\vec{r})$ and $U_\nu(\vec{r})$ are very close. In this case one must use the following relation:

$$\mathbf{W}_\nu(\mathbf{r}) = -\frac{c}{3\kappa_\nu(\mathbf{r})}\nabla U_{b,\nu}(\mathbf{r}). \tag{66}$$

Upon integrating of Equation (76) with respect to radiation frequency we obtain the association of integral flux of radiation with the Rosseland mean coefficient

$$\mathbf{W}(\mathbf{r}) = -\int_0^\infty \frac{c}{3\kappa_\nu(\mathbf{r})}\nabla U_{b,\nu}(\mathbf{r})\,d\nu = -\frac{16}{3}\sigma T^3(\mathbf{r})\kappa_R^{-1}(\mathbf{r})\nabla T(\mathbf{r}), \tag{67}$$

where

$$\kappa_R^{-1}(\mathbf{r}) = \frac{\int_0^\infty \left[1/\kappa_\nu(\mathbf{r})\right]\left[dU_{b,\nu}(T)/dT\right]d\nu}{\int_0^\infty \left[dU_{b,\nu}(T)/dT\right]d\nu}. \tag{68}$$

It should be taken into account that the P_1-approximation of spherical harmonic method has a poor precision at small optical thicknesses. To get over the difficulties, one proceeds as follows: the P_1 method is used in that spectral regions where the optical thickness is thick, otherwise the emission approximation (radiation heat transfer with no absorption) is used.

Examples of the use of the P_1-approximation for radiation heat transfer problems are presented in Part 6.1.

3.2 The quadro-moment method

The quadro-moment method, suggested in [1], presents further development of P_1-approximation for two-dimensional geometry.

Spectral radiation intensity $J = J(x, r, \nu)$ obeys the following equation for non-scattering medium under LTE (frequency dependence is left out for charity)

$$\sqrt{1-\mu^2}\left(\gamma\frac{\partial J}{\partial r}+\frac{1-\gamma^2}{r}\frac{\partial J}{\partial \varphi}\right)+\mu\frac{\partial J}{\partial x}+\kappa J=\kappa J_b, \tag{69}$$

where $\mu=\cos\theta$, $\gamma=\cos\varphi$, $\Omega=(\omega_X,\omega_r)$, $\omega_X=\mu$, $\omega_r=\gamma\sqrt{1-\mu^2}$ are the cosine of vectors Ω with respect to radial *r* and axial *x* coordinates; J_b is the Plank intensity. Let the problem is mirror-symmetrical about the plane containing vectors $\mathbf{x}^0$ and $\mathbf{r}^0$. It allows to consider region for the azimuthal coordinate $0\le\varphi\le\pi$.

The essence of the method is that four angular domains are introduced (Figure 3.7) and Equation (69) is integrated over these domains with various weight functions. This is usually performed using the moment-based methods or multiple spherical harmonics approximations [3, 8].

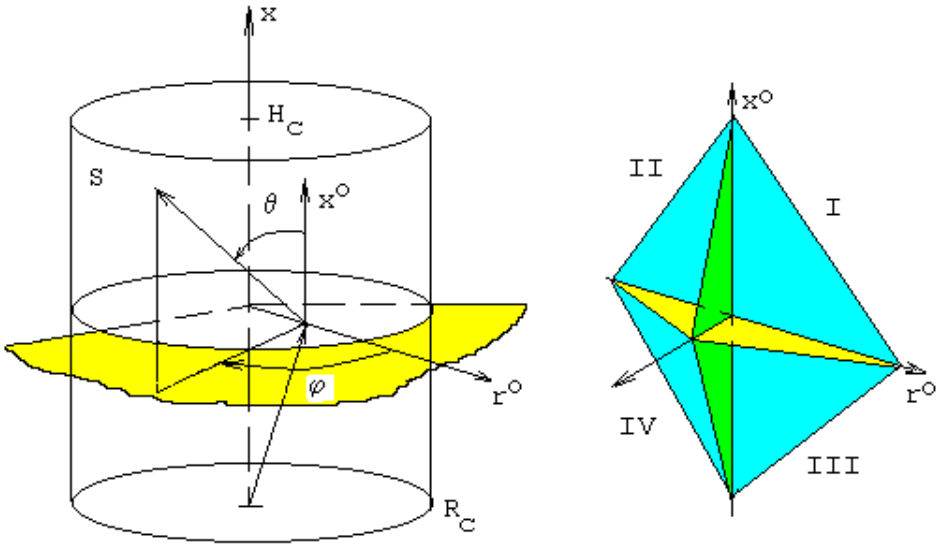

Figure 3.7: Schematic of the two-dimensional axial symmetry problem

In each of these angular zones volumetric spectral radiation densities are introduced by definition

$$\tilde{U}^{\pm}=\tilde{Q}^{\pm}\{J\}=2\int_0^1\frac{d\gamma}{\sqrt{1-\gamma^2}}\int_0^1 J\,d\mu\,. \tag{70}$$

The projections of spectral flux density in radial direction are expressed as

$$\tilde{W}_r^{\pm}=\pm\tilde{R}^{\pm}\{J\}=2\int_0^1\frac{\gamma d\gamma}{\sqrt{1-\gamma^2}}\int_0^1 J\sqrt{1-\mu^2}\,d\mu\,. \tag{71}$$

In the axial direction, the flux density is

$$\hat{W}_x^{\pm}=\hat{X}^{\pm}\{J\}=2\int_0^1\frac{d\gamma}{\sqrt{1-\gamma^2}}\int_0^1 J\mu\,d\mu\,, \tag{72}$$

$$\breve{W}_x^{\pm} = -\breve{X}^{\pm}\{J\} = 2\int_0^1 \frac{\mathrm{d}\gamma}{\sqrt{1-\gamma^2}} \int_0^1 J\mu \mathrm{d}\mu\,. \tag{73}$$

Formulas (70)–(73) include indexes {(~=∩,∪), +, –}, fixing the angular zones:

$$(\cap)-\mu \geq 0,\ (\cup)-\mu < 0,\ (+)-\gamma \geq 0,\ (-)-\gamma < 0\,.$$

Consecutive application of operators $\tilde{Q}^{\pm}, \tilde{R}^{\pm}, \tilde{X}^{\pm}$ to Equation (70) results in the following system of equations:

$$\frac{m}{r}\frac{\partial}{\partial r}\left(r\tilde{L}_1^{\pm}\right) - \frac{m}{r}\tilde{L}_2^{\pm} + n\frac{\partial \tilde{L}_3^{\pm}}{\partial x} + k\left(\tilde{W}_r^{\pm} - \frac{\pi}{2}J_b\right) = 0\,, \tag{74}$$

$$\frac{m}{r}\frac{\partial}{\partial r}\left(r\tilde{M}_1^{\pm}\right) - \frac{m}{r}\tilde{M}_2^{\pm} + n\frac{\partial M_3^{\pm}}{\partial x} + k\left(\tilde{W}_x^{\pm} - \frac{\pi}{2}J_b\right) = 0\,, \tag{75}$$

$$\frac{m}{r}\frac{\partial}{\partial r}\left(r\tilde{W}_r^{\pm}\right) + n\frac{\partial \tilde{W}_x^{\pm}}{\partial x} - \frac{2m}{r}\int_0^1 J(\gamma=0)k\sqrt{1-\mu^2}\mathrm{d}\mu + \left(\tilde{U}^{\pm} - \pi J_b\right) = 0\,, \tag{76}$$

where

$$\tilde{L}_1^{\pm} = 2\int_0^1 \frac{\gamma^2\mathrm{d}\gamma}{\sqrt{1-\gamma^2}} \int_0^1 J\left(1-\mu^2\right)\mathrm{d}\mu\ ,\quad \tilde{M}_1^{\pm} = 2\int_0^1 \frac{\gamma\mathrm{d}\gamma}{\sqrt{1-\gamma^2}} \int_0^1 J\mu\sqrt{1-\mu^2}\mathrm{d}\mu\,;$$

$$\tilde{L}_2^{\pm} = 2\int_0^1 \sqrt{1-\gamma^2}\mathrm{d}\gamma \int_0^1 J\left(1-\mu^2\right)\mathrm{d}\mu\,,\quad \tilde{M}_2^{\pm} = 2\int_0^1 J(\gamma=0)\mu\sqrt{1-\mu^2}\mathrm{d}\mu\,;$$

$$\tilde{L}_3^{\pm} = 2\int_0^1 \frac{\gamma\mathrm{d}\gamma}{\sqrt{1-\gamma^2}} \int_0^1 J\mu\sqrt{1-\mu^2}\mathrm{d}\mu\ ,\quad \tilde{M}_3^{\pm} = 2\int_0^1 \frac{\mathrm{d}\gamma}{\sqrt{1-\gamma^2}} \int_0^1 J\mu^2\mathrm{d}\mu\,;$$

$$\gamma > 0,\ m=1;\ \gamma < 0,\ m=-1;\ \mu > 0,\ n=1;\ \mu < 0,\ n=-1.$$

The resulting system of equations may be used to build a group of calculation methods. In spite of the fact that no simplifying assumptions were made for this system, it can not be considered as exact analogue of the transfer equation, because the resulting system contains of infinite number of ordinary differentials equations.

Closing of the system means that a finite number of components is used in decomposition of intensity into series by orthonormal functions. For the full solid angle 4π the convenient orthonormal basis is the system of spherical harmonics. The first two components of these series (which corresponds to the P_1 Spherical Harmonics approximation method) with regard to evenness at φ, provide:

$$J(x,r,\varphi,\theta) = c(x,r) + a(x,r)\mu + b(x,r)\gamma\sqrt{1-\mu^2}\,. \tag{77}$$

Approximation of radiation intensity by orthogonal polynomial at halved segments is given as

$$J(x,r,\varphi,\theta)=c(x,r)+a(x,r)\mu\left(2\mu^2-1\right)+2b(x,r)\mu^2\sqrt{1-\mu^2}\left(2\gamma^2-1\right)\ . \tag{78}$$

If decomposition similar to the Eq. (77) is used for calculation of functions $\tilde{U}^{\pm}$, $\tilde{W}_r^{\pm}$, $\tilde{W}_x^{\pm}$, $\tilde{L}_l^{\pm}$, $\tilde{M}_l^{\pm}$, then instead of Eqs. (74)–(76) one can obtain a system of equation in relation to coefficients *a*, *b*, *c*. It is reasonably to call this method as a *method of quadro-moments*, since it is analogous to moment methods, but corresponds to one quarter of a solid angle. Using the decomposition given by Eq. (77), coefficients of Eq. (74) to (76) can be calculated.

Let us consider equations for the zero-order equations of the quadro-moment method. Assume

$$\tilde{J}^{\pm}(x,r,\varphi,\theta)=\tilde{c}^{\pm}(x,r)\ . \tag{79}$$

Using (79), Equation (79) becomes

$$\frac{m}{r}\frac{\partial r\tilde{c}^{\pm}}{\partial r}+n\frac{\partial\tilde{c}^{\pm}}{\partial x}-\frac{m}{r}\tilde{c}^{\pm}+2k\tilde{c}^{\pm}=2kJ_b\,, \tag{80}$$

$$\tilde{U}^{\pm}=\pi\tilde{c}^{\pm},\quad \tilde{W}_r^{\pm}=\tilde{W}_x^{\pm}=\frac{\pi}{2}\tilde{c}^{\pm}\,. \tag{81}$$

The boundary conditions are formed for each of the four directions. Let isotropic radiation with intensity J^0 falls onto the external surface of a cylinder, then

at $r=R_c,\quad \hat{c}^{-}=\breve{c}^{-}=J^0$;

at $x=0,\quad \hat{c}^{-}=\hat{c}^{+}=J^0$;

at $x=H_c,\quad \breve{c}^{-}=\breve{c}^{+}=J^0$.

At the symmetry axle

$$\hat{c}^{+}(r=0)=\hat{c}^{-}(r=0),\quad \breve{c}^{+}(r=0)=\breve{c}^{-}(r=0)\ .$$

The zero-approximation of the quadro-moment method (80) in relation to spectral functions has the following form:

$$\frac{m}{r}\frac{\partial r\tilde{c}_\nu^{\pm}}{\partial r}+n\frac{\partial\tilde{c}_\nu^{\pm}}{\partial x}-\frac{m}{r}\tilde{c}_\nu^{\pm}+2k_\nu\tilde{c}_\nu^{\pm}=2k_\nu J_{b,\nu}\,, \tag{82}$$

$$\tilde{U}_\nu^{\pm}=\pi\tilde{c}_\nu^{\pm},\quad \tilde{W}_{\nu,r}^{\pm}=\tilde{W}_{\nu,x}^{\pm}=\frac{\pi}{2}\tilde{c}_\nu^{\pm}\,. \tag{83}$$

In group approximation (with the number of groups N_k) index ν should be replaced by an integer number index $k=1,2,...,N_k$, which denotes a number of spectral energy group. Instead of four Equations (80) the ($4N_k$) equations are formed. Integrating (82) over the whole spectral interval Δν yield

$$\frac{m}{r}\frac{\partial r\tilde{c}^{\pm}}{\partial r}+n\frac{\partial\tilde{c}^{\pm}}{\partial x}-\frac{m}{r}\tilde{c}^{\pm}+2\int_{\Delta\nu}k_\nu\tilde{c}_\nu^{\pm}\mathrm{d}\nu=2\int_{\Delta\nu}k_\nu J_{b,\nu}\mathrm{d}\nu\,, \tag{84}$$

where $\tilde{c}^{\pm} = \int_{\Delta\nu} \tilde{c}_{\nu}^{\pm} d\nu$. Effective integral absorption coefficient is given as

$$\tilde{k}^{\pm} = \frac{1}{\tilde{c}^{\pm}} \int_{\Delta\nu} k_{\nu} \tilde{c}^{\pm} d\nu . \tag{85}$$

Then Equation (84) becomes

$$\frac{m}{r}\frac{\partial r\tilde{c}^{\pm}}{\partial r} + n\frac{\partial \tilde{c}^{\pm}}{\partial x} - \frac{m}{r}\tilde{c}^{\pm} + 2\tilde{k}^{\pm}\tilde{c}^{\pm} = \frac{2}{\pi}k_p \sigma T^4, \tag{86}$$

where $k_p = \frac{\int_{\Delta\nu} k_b J_{b,\nu} d\nu}{\int_{\Delta\nu} J_{b,\nu} d\nu}$ is the average Planck coefficient.

The boundary conditions for Equation (84) are obtained by integration of corresponding spectral conditions with respect to the wave number. The advantage of such formulation of the quadro-moment method is that unlike methods of averaging by the full solid angle (for example, P_1-approximation), where the average integral absorption coefficient may have gaps of the second type, the given case presents a smooth continuous symbol function.

Examples of the use of the quadro-moment method for radiation heat transfer problems are presented in Section 6.2.

3.3 The ray-tracing method

The ray-tracing method (RTM) is usually used for calculation of radiation heat flux to surfaces of different energetic devices and space vehicles. Schematic of typical problem is shown in Figure 3.8. In the given case the researched model of Mars Sample Return Orbiter (MSRO) has the shape of a circular truncated cone (*a*), integrated with a spherical segment (*b*) on the part of an incident flow, and with the circular cylinder (*c*) in a base area. For the condition of axial symmetry to calculate a radiation heat flux on the MSRO surface it is enough to perform calculation along a contour on the surface shown in Figure 3.8.

Algorithm of the ray-tracing method consists in the following. To calculate of a radiation heat flux to any element of the MSRO surface, the local spherical coordinate system with a normal $\vec{n}$ is entered.

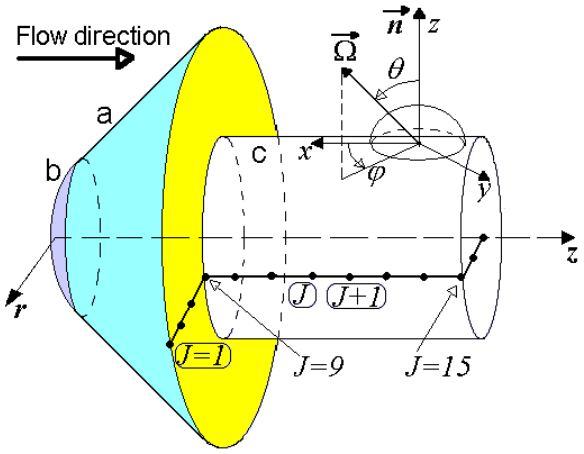

Figure 3.8: Schematic of research model of Mars Sampler Research Orbiter Each ray $\vec{\Omega}$ is defined in this local coordinate system by the following two angular coordinates: the latitude angle $\theta \in [0, \pi/2]$, and the azimuth angle $\varphi \in [0, 2\pi]$.

The radiation heat flux is defined by the following formula:

$$W_\nu(\vec{R}_j) = \int_0^{2\pi} d\varphi \int_0^{\pi/2} J_\nu(\vec{R}_j, \vec{\Omega}) \cos\theta \sin\theta d\theta = \int_0^{2\pi} d\varphi \int_0^{1} J_\nu(\vec{R}_j, \vec{\Omega}) \mu d\mu, \tag{87}$$

where $\mu = \cos\theta$, $\vec{R}_j = (r_j, z_j)$ is the radius-vector of the *j*-th point on the MSRO surface in the laboratory co-ordinates, r_j, z_j are the radial and axial coordinates of the *j*-th point, $J_\nu(\vec{R}_j, \vec{\Omega})$ is the spectral radiation intensity in the point $\vec{R}_j$ corresponding to direction $\vec{\Omega}$.

Introduction of finite-difference mesh of angular directions allows to integrate the spectral intensity in Equation (87) on angular variables and to calculate the spectral radiation flux:

$$W_\nu(\vec{R}_j) = \sum_{m=1}^{N_\varphi - 1} (\varphi_{m+1} - \varphi_m) \sum_{n=1}^{N_\theta - 1} J_\nu(\Omega_{m,n}) (\mu_n - \mu_{n+1}). \tag{88}$$

The direction cosines of the vector $\vec{\Omega}_{m,n} = (\omega_x)_{m,n} \vec{i} + (\omega_y)_{m,n} \vec{j} + (\omega_z)_{m,n} \vec{k}$ are calculated by the following formulas:

$$(\omega_x)_{m,n} = \sqrt{1 - \bar{\mu}_n^2} \cos\bar{\varphi}_m, \quad (\omega_y)_{m,n} = \sqrt{1 - \bar{\mu}_n^2} \sin\bar{\varphi}_m, \quad (\omega_z)_{m,n} = \bar{\mu}_n, \tag{89}$$

where

$$\bar{\mu}_n = 0.5(\mu_n + \mu_{n+1}), \ \bar{\varphi}_m = 0.5(\varphi_m + \varphi_{m+1}).$$

The *z* axis of the local coordinate system of angular directions coincides with the local normal to the MSRO surface.

To calculate spectral radiation intensity a radiation heat transfer equation should be integrated through inhomogeneous optical path. The following solution of the radiation heat transfer equation can be used for this purpose:

$$J_\nu\left(\vec{\Omega}_{m,n}\right)=\int_{s=0}^{s=L} J_{b,\nu}(s)\kappa_\nu(s)\exp\left[-\int_0^s \kappa_\nu(s')\mathrm{d}s'\right]\mathrm{d}s\,, \tag{90}$$

where $s=0$ and $s=L$ are the initial (on the MSRO surface) and final (on the outer surface of the calculation region or on the MSRO conjugate surface) coordinates of the segment with directing vector $\vec{\Omega}_{m,n}$.

Finite-difference scheme on *s*-axis is formulated for each ray $\vec{\Omega}_{m,n}$. The coordinates of the intersections of the ray $\vec{\Omega}_{m,n}$ with all surfaces of the spatial finite-difference mesh should be calculated. This is illustrated by Figure 3.9 (see points on the ray *a*).

Relations of the analytical geometry should be used for these purposes. However, this algorithm is not effective due to very high time consuming, especially for non-structured meshes. More effective algorithm of the quasi-random sampling was suggested in [1]. A segment with directional vector $\vec{\Omega}$ (between the initial and final points) is divided on N_s sub regions as it is shown in Figure 3.9 (see points on ray *b*). Then, the nearest node or elemental volume of a spatial computational grid is searched for each node s_k. In that way temperatures and spectral absorption coefficients are set to each node of the segment $[s=0,\ s=L]$.

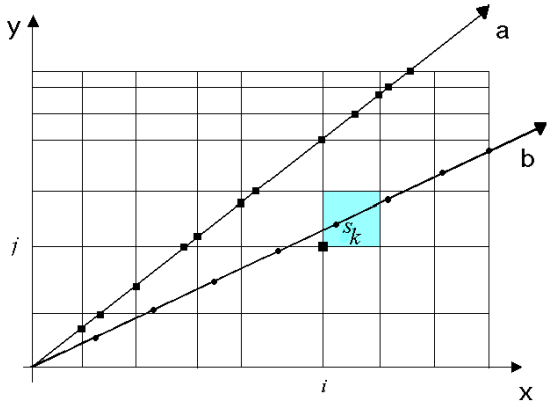

Figure 3.9: Two alternative finite-difference schemes along *s*-axis

Numerical integration of the solution (90) of radiation heat transfer equation is realized as follows:

$$J_\nu\left(\vec{\Omega}_{m,n}\right)=\sum_{k=1}^{N_s-1} J_{b,\nu,k+1/2}\left(T_k-T_{k+1}\right),$$

where $J_{b,\nu,k+1/2}$ is the spectral intensity of the black body, which is calculated using average temperature of the segment $[s_k, s_{k+1}]$; $T_k=\exp\left[-\int_{s_1}^{s_k}\kappa_\nu(s')\mathrm{d}s'\right]$ is the spectral transmission factor.

Examples of the use of the P_1-approximation for radiation heat transfer problems are presented in Part. 6.1.

3.4 Discrete Ordinates Method (DOM)

The DOM on three-dimensional rectangular [9] and cylindrical [10] computational grids was used successfully for calculation radiative transport in a participating media. Ramankutty and Crosbie [11] presented a modified discrete ordinates solution of three-dimensional radiative transfer in enclosures with localized boundary loading situations. Another method, SN-DOM, was used in [12] to find the spectral characteristics of thermal radiation for a two-dimensional, axisymmetric, free-burning argon arc. Such a method was also used to study radiative heating of internal surface of the air and hydrogen laser supported plasma generator in [13], [14].

Sakami et al. [15] proposed a modification of the standard DOM for non-orthogonal computational grids (for the tetrahedral grids). Further development of the DOM algorithm was used to predict of radiative heat fluxes on back surface of Mars Sample Return Orbiter [16].

Computational domain in a rectangular Cartesian geometry is divided into finite numbers of non overlapping tetrahedral cells. The radiation heat transfer equation in a discrete ordinates representation is given by

$$\eta_m \frac{\partial I_\varpi^m}{\partial x} + \mu_m \frac{\partial I_\varpi^m}{\partial y} + \xi_m \frac{\partial I_\varpi^m}{\partial z} = \kappa_\varpi \left(I_{b,\varpi} - I_\varpi^m \right), \tag{91}$$

where I_ϖ^m is the spectral radiation intensity, which is a function of position and direction $\vec{\Omega}_m$; $I_{b,\varpi}$ is the spectral blackbody radiation at the temperature of the medium; κ_ϖ is the spectral absorption coefficient of the medium; η_m, μ_m, ξ_m are the directional cosines of the direction $\vec{\Omega}_m$; ϖ is the wave number.

The condition at the boundary Γ of computational domain is given as

$$I_\varpi^m = 0, \qquad \vec{r} \in \Gamma. \tag{92}$$

If the surface of the space vehicle Γ' is assumed gray and emits and reflects diffusely, then the radiative boundary condition at the MSRO surface is given by

$$I_\varpi^m = \varepsilon I_{b\Gamma} + \frac{1-\varepsilon}{\pi} \sum_{\vec{n}_\Gamma \vec{\Omega}_{m'} < 0} \omega_{m'} \left| \vec{n}_\Gamma \vec{\Omega}_{m'} \right| I_\varpi^{m'}, \qquad \vec{r} \in \Gamma'. \tag{93}$$

Spectral values are replaced by group values. A control volume form of Equation (91) can be obtained by integrating over the tetrahedral volume as follows:

$$\sum_{i=1}^{4} \left(\vec{n}_i \vec{\Omega}_m \right) S_i I_i^m = \kappa_p V_p \left(I_{b,p} - I_p^m \right), \tag{94}$$

where $I_i^m = \frac{1}{S_i} \int_{S_i} I^m \mathrm{d}\sigma$ is the side area averaged group intensity; the number of the tetrahedral face is i and the area of the face is S_i; $I_p^m = \frac{1}{V_p} \int_{V_p} I^m \mathrm{d}\upsilon$ is the cell volume averaged group intensity; V_p is the volume of tetrahedral cell; $\vec{n}_i$ is the normal to the side i of the tetrahedral cell; κ_p is the group absorption coefficient in the cell; $I_{b,p}$ is the group blackbody radiation at the temperature in the cell p.

Solving Equation (94) for cell center group intensity, I_p^m may be evaluated as

$$I_p^m = I_{b,p} - \frac{1}{\kappa_p V_p} \sum_{i=1}^{4} \left(\vec{n}_i \vec{\Omega}_m \right) S_i I_i^m \,. \tag{95}$$

Therefore, to solve equation (95), auxiliary relations among average intensities on sides of tetrahedral cell are necessary. Tree cases arise with a tetrahedral cell (Figure 3.10), depending on the manner the cell is approached by radiation. These cases were derived in detail in [15].

If the one face receives radiation from the three other faces (Figure 3.10,*a*), then intensity on receiving face 4 is given as

$$I_4^m = \left(\frac{S_{14}}{S_4} I_1^m + \frac{S_{24}}{S_4} I_2^m + \frac{S_{34}}{S_4} I_3^m \right) \chi_p + I_{b,p} \left(1 - \chi_p \right). \tag{96}$$

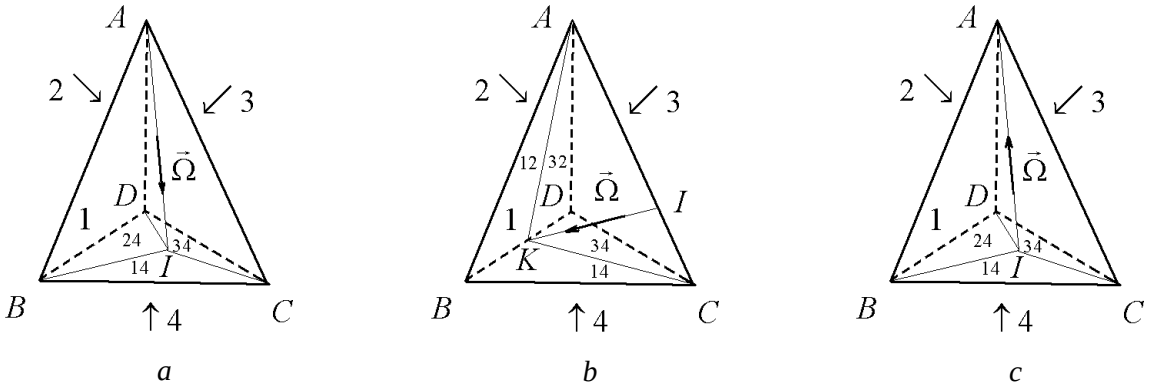

Figure 3.10: Three possible cases of the radiative transport in a tetrahedral cell

For the second case, when two faces receive radiation from other two faces (Figure 3.10,*b*), intensities on receiving faces are

$$I_2^m = \left(\frac{S_{12}}{S_2} I_1^m + \frac{S_{32}}{S_2} I_3^m \right) \chi_p + I_{b,p} \left(1 - \chi_p \right), \tag{97}$$

$$I_4^m = \left(\frac{S_{14}}{S_4} I_1^m + \frac{S_{34}}{S_4} I_3^m \right) \chi_p + I_{b,p} \left(1 - \chi_p \right). \tag{98}$$

Third case describes the situation, when three faces receive radiation from the fourth one. Intensities on receiving faces are given as

$$I_1^m = I_2^m = I_3^m = I_4^m \chi_p + I_{b,p} \left(1 - \chi_p \right). \tag{99}$$

Equations (96)–(99) include function χ_p which can be expressed as

$$\chi_p = \frac{2}{\tau_p}\left(1 - \frac{1 - e^{-\tau_p}}{\tau_p}\right), \tag{100}$$

where τ_p is the maximum optical thickness in the cell p in direction $\vec{\Omega}_m$.

To predict the fluid flow and convective heat transfer in the geometrically complex systems of practical interest, computational methods are normally implemented on non orthogonal boundary-fitted meshes. Many such problems also require prediction of the radiant heat transfer, where the medium affects the heat transfer through emission and absorption. Radiation heat transfer equation governs this radiant exchange. It is desirable to solve this equation on the same computational grid used for the fluid flow.

The DOM on tetrahedral grids can be applied to find the radiation field in the complex computational domain. In the case of three dimensional geometry octahedral cell is divided into six tetrahedrons *ABCF*, *AFDE*, *FCDA*, *DEGH*, *GEFD*, *GFCD* (Figure 3.11, *a*). The cylindrical meshes also have hexahedral cells adjoining *z* axis (Figure 3.12, *a*). Hexahedrons are divided into three tetrahedral cells *ABCD*, *BCEF*, *CDEB* (Figure 3.11, *b*). Using quasi uniform meshes (Figure 3.12, *b*) is preferable in the case of axial symmetry.

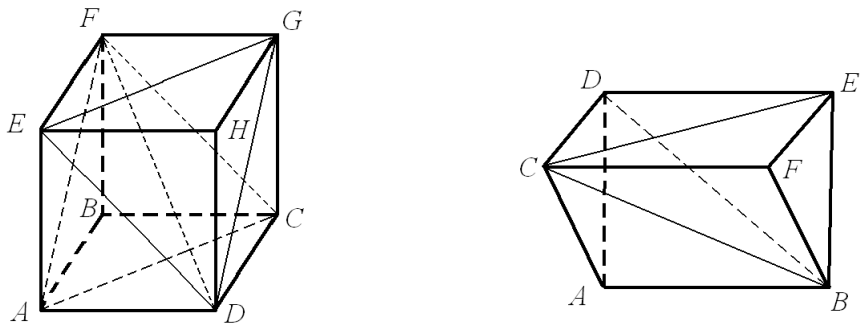

a *b*

Figure 3.11: Tetrahedral cell partition

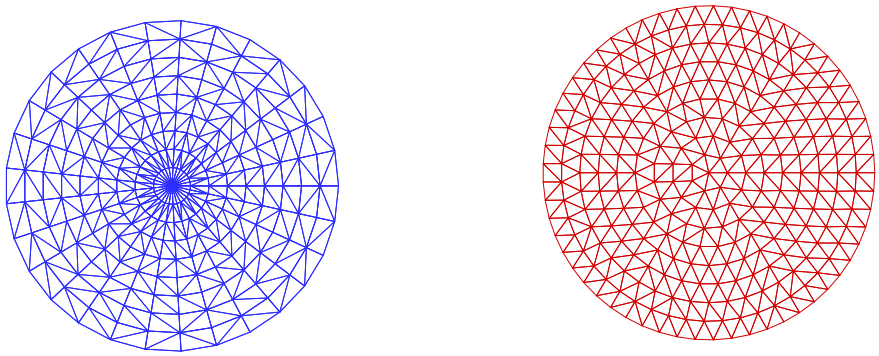

a *b*

Figure 3.12: Cross section of cylindrical computational domain that is perpendicular to the *z* axis (*a*). Cross section of quasi uniform grid constructed in cylindrical computational domain

The accuracy of the discrete ordinates solution depends on the choice of the quadrature scheme. Although this choice, in principle, arbitrary, a completely symmetric quadrature is preferred in order to preserve geometric invariance of the solution. The quadrature schemes used in [16] are based on the "moment-matching" technique, whereby the ordinates are chosen so as to integrate as many moments of intensity

distribution as possible. Although any type of the quadrature can be applied the SN quadrature sets were used in [16]. The recognition algorithm was created to identify the type of $\vec{\Omega}_m$ orientation in the cell. This algorithm permits to apply appropriate characteristic Equations (96)–(99) for finding unknown average face intensity. If the solver visits the cells in the correct order, all terms on the right side of the Equation (95) will be known so center intensity can be found by direct substitution. This allows the solution to be obtained by moving from cell to cell in the optimal "matching order".

For the irregular grid the order is not obvious. To find a solution on irregular grids the equation could be solved by repeatedly sweeping across the grid without regard to the optimal order. Creating of a "marching order map" gives the optimal order in which the cells will be visited. Once the quadrature scheme is fixed, a marching order map can be constructed for each intensity direction, and this map can be written to file for repeated use. To create the map, the boundary cells are swept first to find the starting location. The map is easy to generate, it needs to be revised only when the spatial grid or quadrature scheme have been changed. Because it reduces solution costs, the creation of the map is the preferred alternative.

Examples of the use of the P_1-approximation for radiation heat transfer problems are presented in Section 6.4.

4.0 THE RANDOM MODELS

4.1 Formulation of Random Models for Atomic Lines

Random model of molecular lines was originally offered and investigated in the Refs. [17,18]. Detailed description of the random approach is presented in [19]. Being based on the specified references, we shall obtain formulas of generalized random model of rotational molecular lines and spectral atomic lines. Note that the distinctive property of band of atomic lines is that the half-widths of the atomic lines differ significantly. In the case of rotational molecular lines, theirs half-widths differ insignificantly.

Let a spectral range $\Delta\omega$ contains N atomic lines. Then spectral transmission along the homogeneous optical path L is calculated as follows:

$$T(\omega) = \prod_{i=1}^{N} T(\omega, \omega_i), \tag{1}$$

where $T(\omega, \omega_i) = \exp\left[-\kappa_i(\omega, \omega_i) L\right]$, $\kappa_i(\omega, \omega_i)$ is the spectral absorption coefficient of i-th line, ω_i is the wavenumber of i-th line.

Integrated transmission in the spectral range $\Delta\omega$ is determined under the formula

$$T = \int_{\Delta\omega} T(\omega) \mathrm{d}\omega, \tag{2}$$

and average transmission is determined as follows

$$T_{\Delta\omega} = \frac{1}{\Delta\omega} \int_{\Delta\omega} T(\omega) \mathrm{d}\omega. \tag{3}$$

It is obvious, that average transmission (3) will depend on how the lines are placed inside the range $\Delta\omega$. Intuitively also it is clear that at large number N this dependence is not strong. The truth of such an assumption easily to check up by means of line-by-line integration for any set of lines. This fact allows give a probabilistic interpretation for averaged transmission. For this purpose it is necessary to formulate probability of realization of just given configuration of lines inside the range $\Delta\omega$, and then to estimate mathematical expectation of averaged transmission for every possible configurations.

Let us define probability for i-th line to have intensity in the range $\mathrm{d}S_i$ in the vicinity of S_i, half-width in the range $\mathrm{d}\gamma_i$ in the vicinity of γ_i, and location in the limits $\mathrm{d}\omega_i$ in the vicinity of ω_i as follows:

$$\mathrm{d}P_i = \mathrm{d}P_i(\omega_i, S_i, \gamma_i) = p_i(\omega_i)\, p_i(S_i)\, p_i(\gamma_i)\mathrm{d}\omega_i\, \mathrm{d}S_i\, \mathrm{d}\gamma_i, \tag{4}$$

where statistical independence of realization of the location, intensity and half-width of the line is supposed, $p(\omega_i), p(S_i), p(\gamma_i)$ are the probability densities for realization of the location, intensity and half-width of the line. Then the mathematical expectation of the integrated transmission can be determined as follows:

$$\overline{T} = \int_{\Delta\omega}\left\{\int_{\Delta\omega_1}\int_{\Delta S_1}\int_{\Delta\gamma_1}\ldots\int_{\Delta\omega_N}\int_{\Delta S_N}\int_{\Delta\gamma_N}\left\{T(\omega)\prod_{i=1}^{N} p_i(\omega_i)\mathrm{d}\omega_i\, p_i(S_i)\mathrm{d}S_i\, p_i(\gamma_i)\mathrm{d}\gamma_i\right\}\right\}\mathrm{d}\omega. \tag{5}$$

Now, let us assume that the probability of realization of the parameters of each line $(\omega_i, S_i, \gamma_i)$ do not depend on realization of the parameters of any other line. It allows simplify last relation:

$$\overline{T} = \int_{\Delta\omega}\left\{\prod_{i=1}^{N}\int_{\Delta\omega_i}\int_{\Delta S_i}\int_{\Delta\gamma_i} T(\omega, \omega_i, S_i, \gamma_i)\, p_i(\omega_i)\, p(S_i)\, p(\gamma_i)\mathrm{d}\omega_i\, \mathrm{d}S_i\, \mathrm{d}\gamma_i\right\}\mathrm{d}\omega, \tag{6}$$

where the explicit dependence from S_i and γ_i is entered into the list of arguments of spectral transmission.

Among lines located in the spectral range can be as strongly differing lines, and the lines with rather close parameters. Let us enter conditional division of the lines into groups, in limits of which the probabilities of realization of the lines parameters can be described by the uniform law. Thus we shall remind, that in the limits of any allocated group all lines are indiscernible (the statistical independence of the lines parameters already was used at transition from Equation (5) to Equation (6)). Then, Equation (6) can be rewritten

$$\overline{T} = \int_{\Delta\omega}\left\{\prod_{g=1}^{G}\prod_{i=1}^{N_g}\int_{\Delta\omega_i}\int_{\Delta S_i}\int_{\Delta\gamma_i} T(\omega, \omega_i, S_i, \gamma_i)\, p_i(\omega_i)\, p_i(S_i)\, p_i(\gamma_i)\mathrm{d}\omega_i\, \mathrm{d}S_i\, \mathrm{d}\gamma_i\right\}\mathrm{d}\omega, \tag{7}$$

where N_g is the number of lines in g-th group, G is the number of the groups.

The further analysis of Equation (7) will be connected with concrete definition of the probability densities. We shall accept, that all spectral ranges $\Delta\omega_i$ are equal among themselves $\Delta\omega_i = \Delta\omega, i = 1, 2, \ldots, N_g$ thus they are distributed equiprobably, that is $p_i(\omega_i) = 1/\Delta\omega$, then

$$\overline{T} = \int_{\Delta\omega}\prod_{g=1}^{G}\left[\frac{1}{\Delta\omega}\int_{\Delta\omega}\int_{\Delta S_g}\int_{\Delta\gamma_g} T(\omega, \omega', S', \gamma')\, p(S')\, p(\gamma')\mathrm{d}\omega'\mathrm{d}S'\mathrm{d}\gamma'\right]^{N_g}\mathrm{d}\omega, \tag{8}$$

where ΔS_g and $\Delta\gamma_g$ are the ranges of change of the intensity and half-width in limits of the g-th group.

Expression in square brackets has meaning of the average transmittance in spectral group

$$T_g(\omega)=\left[\frac{1}{\Delta\omega}\int\limits_{\Delta\omega}\int\limits_{\Delta S_g}\cdot\int\limits_{\Delta\gamma_g}T(\omega,\omega',S',\gamma')\,p(S')\,p(\gamma')\,\mathrm{d}\omega'\mathrm{d}S'\mathrm{d}\gamma'\right]^{N_g}. \tag{9}$$

Let us enter a new scale of wave numbers, connected to centre of the spectral range

$$\Delta\omega=\omega_{\max}-\omega_{\min}:\ \nu=\omega-\Omega_0, \tag{10}$$

where $\omega_0=0.5(\omega_{\min}+\omega_{\max})$, $\omega_{\min},\omega_{\max}$ are the boundaries of the spectral region. Then

$$\nu_{\min}=-0.5\Delta\omega\quad,\ \nu_{\max}=+0.5\Delta\omega. \tag{11}$$

If the average distance between lines in g-th group to define under the formula

$$\delta_g=\Delta\omega/N_g, \tag{12}$$

then $\nu_{\min}=-0.5N_g\delta_g$, $\nu_{\max}=+0.5N_g\delta_g$.

Now it is possible to copy (9) in the following form:

$$T_g(\omega)=\left[\frac{1}{N_g}\int\limits_{\Delta S_g}\int\limits_{\Delta\gamma_g}\frac{1}{\delta_g}\cdot\int\limits_{-\frac{1}{2}N_g\delta_g}^{+\frac{1}{2}N_g\delta_g}T(\omega,\omega',S',\gamma')\,p(S')\,p(\gamma')\,\mathrm{d}\nu'\mathrm{d}S'\mathrm{d}\gamma'\right]^{N_g}=$$

$$=\left\{1-\frac{1}{N_g}\frac{1}{\delta_g}\int\limits_{-\frac{1}{2}N_g\delta_g}^{+\frac{1}{2}N_g\delta_g}\left[1-\int\limits_{\Delta S_g}\int\limits_{\Delta\gamma_g}T(\omega,\omega',S',\gamma')\,p(S')\,p(\gamma')\,\mathrm{d}S'\mathrm{d}\gamma'\right]\mathrm{d}\nu'\right\}^{N_g}. \tag{13}$$

At rather large number N_g it is possible to pass to the exponential form in the Equation (13):

$$T_g(\nu)=\exp\left(-W_g/\delta_g\right),$$

where

$$W_g(\nu)=\int\limits_{-\frac{1}{2}N_g\delta_g}^{+\frac{1}{2}N_g\delta_g}\left[1-\int\limits_{\Delta S_g}\int\limits_{\Delta\gamma_g}T(\omega,\omega',S',\gamma')\,p(S')\,p(\gamma')\,\mathrm{d}S'\mathrm{d}\gamma'\right]\mathrm{d}\nu'\approx$$

$$\approx\int\limits_{-\infty_g}^{+\infty}\left[1-\int\limits_{\Delta S_g}\int\limits_{\Delta\gamma_g}T(\omega,\omega',S',\gamma')\,p(S')\,p(\gamma')\,\mathrm{d}S'\mathrm{d}\gamma'\right]\mathrm{d}\nu'. \tag{14}$$

where W_g is the equivalent width of lines of g-th group. The transition from final limits of integration in

(14) to infinite can be carried out formally, by requiring that $N_g \to \infty$.

However, it is enough, that the following condition should be satisfied

$$\gamma \ll \Delta\omega. \tag{15}$$

Therefore such transition can be made basically even at $N_g = 1$.

Above already was spoken that it is possible to divide all lines in the range $\Delta\omega$ on number of groups. For example, it is possible to use the assumption of affinity of half-width of lines in limits of each group and about identical probability law of lines intensity distribution:

$$p(\gamma') = \delta(\gamma' - \gamma_g), \tag{16}$$

$$p(S') = S_g^{-1} \exp(-S'/S_g). \tag{17}$$

Condition (16) means that inside given group all lines have identical half-widths. The relation (17) is frequently used in the theory of random modeling of rotational lines of a molecular spectrum and physically is substantiated in Ref. [17]. With regard to (16) and (17) one can obtain instead of Equation (14) the following relation:

$$W_g(\nu) = \int_{-\infty}^{+\infty} \left[1 - \int_0^{\infty} T(\gamma, \gamma', S', \gamma_g) \frac{1}{S_g} \exp\left(-\frac{S'}{S_g} \right) \mathrm{d}S' \right] \mathrm{d}\nu'. \tag{18}$$

The intensity of a line *S*, by definition, is integrated absorption coefficient in this line, therefore

$$\kappa(\nu, \nu', S', \gamma_g) = S' f(\nu, \nu', \gamma_g), \tag{19}$$

where the function of the line contour satisfies to the following condition $\int_{-\infty}^{+\infty} f(\nu, \nu', \gamma_g) \mathrm{d}\nu' = 1$.

Therefore, by substituting (19) in (18), one can obtain:

$$W_g(\nu) = \int_{-\infty}^{+\infty} \left\{ \int_0^{\infty} \frac{1}{S_g} \exp\left(-\frac{S'}{S_g} \right) \left[1 - \exp\left(-S' f(\nu, \nu', \gamma_g) \right) L \right] \mathrm{d}S' \right\} \mathrm{d}\nu' = \int \frac{S_g f(\nu, \nu', \gamma_g) L}{1 + S_g f(\nu, \nu', \gamma_g) L} \mathrm{d}\nu'. \tag{20}$$

The further transformation (20) is possible at detailing of spectral dependence of absorption coefficient in atomic lines. Exact and approximation expressions for equivalent width of lines of Lorentzian, Doppler, and Voigt contours were obtained in the theory of statistical modelling of spectral lines [17,18].

Thus, the mathematical expectation of integrated transmission in a range $\Delta\omega$ takes the following form:

$$\bar{T} = \Delta\omega \prod_{g=1}^{G} \exp\left(-\frac{W_g}{\delta_g} \right). \tag{21}$$

Hence, average transmission in any range does not depend on wave number

$$\bar{T}_{\Delta\omega} = \prod_{g=1}^{G} \exp\left(-\frac{W_g}{\delta_g} \right) = \prod_{g=1}^{G} T_g \ . \tag{22}$$

The given formulation of random model contains a large variety of random models: from simple random model ($G=1$) up to generalized random model ($G=N$) of superposition of lines of various bands. In conformity to the formulation of generalized random model, given by Goody [17], now it is possible to assume, that the size of the spectral range, in which the average transmission is sought, coincides with average distance between lines in group. It means that the ***random model may be used even for one line***. In other words, it is possible to determine average transmission in a spectral range, containing only one line, being the member of a spectral band with average distance $\Delta\omega$ between lines.

4.2 Numerical Simulation Method for Calculation of Radiative Heat Transfer in Plane-Parallel Non-Uniform Layers

Now, let us consider how it is possible to use the generalized random model for calculation radiative heat transfer in plane-parallel non-uniform layers of low-temperature plasma. For a basis let us consider the equation for radiation transfer in the following form:

$$\frac{\partial J_\omega}{\partial s} = \kappa_\omega \left(J_{b,\omega} - J_\omega \right), \tag{23}$$

where $J_\omega, J_{b\omega}$ are the spectral intensity of radiation of the plasma and absolutely black body; κ_ω is spectral volumetric absorption coefficient; s is a direction of radiation distribution.

For determination of the spectral and integrated radiating characteristics in a plane-parallel non-uniform layer the method of half-moment is used [8]. The Equation (23) can be approximated by equivalent system of the differential equations for spectral half-moment characteristics $M^{\pm}_{n,\omega}$:

$$\frac{\mathrm{d}M^{+}_{n+1,\omega}}{\mathrm{d}\tau_\omega} = -M^{+}_{n,\omega} + \frac{2\pi}{n+1} J_{b,\omega}, \ n = 1, 2, \ldots, \tag{24}$$

$$\frac{\mathrm{d}M^{-}_{n+1,\omega}}{\mathrm{d}\tau_\omega} = -M^{-}_{n,\omega} + \frac{2\pi(-1)^n}{n+1} J_{b,\omega}, \ n = 1, 2, \ldots, \tag{25}$$

where $\mu = \cos\theta, \quad \mathrm{d}\tau_\omega = \kappa_\omega \mathrm{d}x; \quad M^{+}_{n,\omega} = 2\pi M^{-}_{n,\omega} = 2\pi(-1)^n \int_0^1 J^{-}_{\omega} \mu^n \mathrm{d}\mu;$

$$J_\omega = \begin{cases} J^{+}_{\omega}, & 0 \le \theta \le \pi/2, \\ J^{-}_{\omega}, & \pi/2 \le \theta \le \pi; \end{cases} \tag{26}$$

θ is the angle between direction of radiation distribution and x-axis.

Let us assume that external radiation is characterized by the following spectral intensity:

$$x=0,\quad J_\omega(\mu,x=0)=J_\omega^+(x=0),\qquad \mu\subset[0,1],$$
$$x=H,\quad J_\omega(\mu,x=H)=J_\omega^-(x=H),\quad \mu\subset[-1,0],$$

where H is the thickness of the layer.

To limit number of the solved equations in system (24) it is necessary to use any closing condition, by putting all half-moment functions equal to zero since some number. Such closing condition is possible to obtain approximating an angular dependence of intensity by a series on cosines with limited number N of terms. Having integrated this series over two half-spherical angles ($0\le\theta\le\pi/2$, and $\pi/2<\theta\le\pi$) with different weight functions μ^n, it is possible to obtain the following closing relations:

$$M_{n,\omega}^+(\tau_\omega)=\sum_{j=1}^{N}2\pi\frac{a_j^+(\tau_\omega)}{N-j+n+1}, \tag{27}$$

$$M_{n,\omega}^-(\tau_\omega)=\sum_{j=1}^{N}2\pi\frac{(-1)^{N-j+n}\,a_j^-(\tau_\omega)}{N-j+n+1}, \tag{28}$$

where $a_j^+(\tau_\omega)$ and $a_j^-(\tau_\omega)$ are the coefficients of the decomposition. By excluding them from system (27), (28), it is possible to find connection between half-moment characteristics:

$$M_{2,\omega}^+=-\frac{1}{6}M_{0,\omega}^++M_{1,\omega}^+,\quad M_{2,\omega}^-=-\frac{1}{6}M_{0,\omega}^--M_{1,\omega}^-$$

In the second approximation of the half-moment method ($N=2$, $n=0,1,2$) the systems of equations has the following solution:

$$M_{0,\omega}^+(x)=\sum_{m=1}^{2}\beta_m\int_0^x I_{b,\omega}(x')\kappa_\omega(x')\exp\left[-\beta_m\int_{x'}^{x}\kappa_\omega(x'')\mathrm{d}x''\right]\mathrm{d}x'+\sum_{m=1}^{2}\beta_m C_m^+\exp\left[-\beta_m\int_0^x\kappa_\omega(x')\mathrm{d}x'\right], \tag{29}$$

$$M_{1,\omega}^+(x)=\sum_{m=1}^{2}\int_0^x I_{b,\omega}(x')\kappa_\omega(x')\exp\left[-\beta_m\int_{x'}^{x}\kappa_\omega(x'')\mathrm{d}x''\right]\mathrm{d}x'+\sum_{m=1}^{2}C_m^+\exp\left[-\beta_m\int_0^x\kappa_\omega(x')\mathrm{d}x'\right], \tag{30}$$

$$M_{0,\omega}^-(x)=\sum_{m=1}^{2}\beta_m\int_x^H I_{b,\omega}(x')\kappa_\omega(x')\exp\left[-\beta_m\int_{x}^{x'}\kappa_\omega(x'')\mathrm{d}x''\right]\mathrm{d}x'-\sum_{m=1}^{2}\beta_m C_m^-\exp\left[-\beta_m\int_x^H\kappa_\omega(x')\mathrm{d}x'\right], \tag{31}$$

$$M_{1,\omega}^-(x)=-\sum_{m=1}^{2}\int_x^H I_{b,\omega}(x')\kappa_\omega(x')\exp\left[-\beta_m\int_{x}^{x'}\kappa_\omega(x'')\mathrm{d}x''\right]\mathrm{d}x'+\sum_{m=1}^{2}C_m^-\exp\left[-\beta_m\int_x^H\kappa_\omega(x')\mathrm{d}x'\right], \tag{32}$$

where

$$I_{b,\omega}=\pi J_{b,\omega}(x),\quad \beta_1=3-\sqrt{3},\quad \beta_2=3+\sqrt{3},$$

$$C_1^+=-\frac{F_0^+-\beta_2F_1^+}{\beta_2-\beta_1},\quad C_2^+=\frac{F_0^+-\beta_1F_1^+}{\beta_2-\beta_1},\quad C_1^-=\frac{F_0^-+\beta_2F_1^-}{\beta_2-\beta_1},\quad C_2^-=-\frac{F_0^-+\beta_1F_1^-}{\beta_2-\beta_1},$$

$$F_0^+ = 2\pi\int_0^1 J_\omega^+(x=0)\,\mathrm{d}\mu, \quad F_1^+ = 2\pi\int_0^1 J_\omega^+(x=0)\,\mu\mathrm{d}\mu,$$

$$F_0^- = 2\pi\int_0^1 J_\omega^-(x=H)\,\mathrm{d}\mu, \quad F_1^- = 2\pi\int_0^1 J_\omega^+(x=H)\,\mu\mathrm{d}\mu.$$

Let us now find integrated half-moment characteristics in the spectral range $\Delta\omega$. Calculations for the four half-moment functions (29)–(32) are identical, therefore we shall obtain a required relation only for $M_{1,\omega}^+(x)$.

Integrating of Equation (30) in the limits of the $\Delta\omega$ one can derive:

$$M_{1,\Delta\omega}^+(x) = \int_{\Delta\omega} M_{1,\omega}^+(x)\,\mathrm{d}\omega = \sum_{m=1}^{2}\int_0^x\int_{\Delta\omega} I_{b,\omega}(x')\kappa_\omega(x')\exp\left[-\beta_m\int_{x'}^x \kappa_\omega(x'')\mathrm{d}x''\right]\mathrm{d}\omega\mathrm{d}x' +$$

$$+\sum_{m=1}^{2}\int_{\Delta\omega} C_m^+\exp\left[-\beta_m\int_0^x \kappa_\omega(x')\mathrm{d}x'\right]\mathrm{d}\omega. \qquad (33)$$

The first term in the right hand side of Equation (33) correspond to own radiation of the medium:

$$I_1 = \int_0^x\int_{\Delta\omega} I_{b,\omega}(x')\kappa_\omega(x')\exp\left[-\beta_m\int_{x'}^x \kappa_\omega(x'')\mathrm{d}x''\right]\mathrm{d}\omega\mathrm{d}x' = -\int_0^x \bar{I}_{b,\omega}(x')\frac{1}{\beta_m}\frac{\mathrm{d}W_m(x',x)}{\mathrm{d}x'}\mathrm{d}x', \qquad (34)$$

where

$$W_m(x',x) = \int_{\Delta\omega}\left\{1-\exp\left[-\beta_m\int_{x'}^x \kappa_\omega(x'')\mathrm{d}x''\right]\right\}\mathrm{d}\omega, \qquad (35)$$

$$\bar{I}_{b,\omega}(x) = \frac{1}{\Delta\omega}\int_{\Delta\omega} I_{b,\omega}(x)\,\mathrm{d}\omega.$$

At calculation of integral I_1, conveniently to use the following formula

$$I_1 = -\frac{1}{\beta_m}\sum_{i=1}^{i=f-1}\bar{I}_{b,\omega}(x_i)\cdot\left[W_m(x_{i+1},x_f) - W_m(x_i,x_f)\right], \qquad (36)$$

where f is the number of a mesh nodes.

Let us present the absorption coefficient $\kappa_\omega(x)$ as the sum of absorption coefficient in lines $\kappa_\omega^l(x)$ and one in a continuous spectrum $\kappa_\omega^c(x)$. It is assumed, that $\kappa_\omega^c(x) = \kappa^c(x)$, that is it does not depend on wave number in the limits of the $\Delta\omega$. Then the expression for equivalent width (35) can be presented in the following form:

$$W_m\left(x_i,x_f\right)=\left\{1-\exp\left[-\beta_m\int\limits_{x_i}^{x_f}\kappa_\omega^c\left(x'\right)\mathrm{d}x'\right]\right\}\Delta\omega+\exp\left[-\beta_m\int\limits_{x_i}^{x_f}\kappa_\omega^c\left(x'\right)\mathrm{d}x'\right]W_m^*\left(x_i,x_f\right), \tag{37}$$

$$W_m^*\left(x_i,x_f\right)=\int\limits_{\Delta\omega}\left\{1-\exp\left[-\beta_m\int\limits_{x_i}^{x_f}\kappa_\omega^l\left(x'\right)\mathrm{d}x'\right]\right\}\mathrm{d}\omega\,. \tag{38}$$

For calculation of the equivalent width of lines $W_m^*\left(x_i,x_f\right)$ one can use the group random model:

$$W_m^*\left(x_i,x_f\right)=\sum_{g=1}^{G}W_{g,m}^*\left(x_i,x_f\right), \tag{39}$$

where $W_{g,m}^*\left(x_i,x_f\right)$ is the equivalent width of the *g*-th group; *G* is number of atomic lines groups.

Now consider transformation of integral corresponding to the contribution of external radiation. If intensity of external radiation poorly changes in the spectral region $\Delta\omega$, the factors $c_m^{\pm}$ may be considered as constants, then

$$I_2=\int\limits_{\Delta\omega}\exp\left[-\beta_m\int\limits_{0}^{x_f}\kappa_\omega\left(x'\right)\mathrm{d}x'\right]\mathrm{d}\omega\,.$$

Because $\kappa_\omega\left(x'\right)=\kappa_\omega^c\left(x'\right)+\kappa_\omega^l\left(x'\right)$, then

$$I_2=\exp\left[-\beta_m\int\limits_{0}^{x_f}\kappa_\omega^c\left(x'\right)\mathrm{d}x'\right]\cdot\int\limits_{\Delta\omega}\exp\left[-\beta_m\int\limits_{0}^{x_f}\kappa_\omega^l\left(x'\right)\mathrm{d}x'\right]\mathrm{d}\omega\,.$$

In this formula integration over wavenumber gives total transmission in the region $\Delta\omega$, that is in conformity with (21)

$$T\left(x_1=0,x_f\right)=\Delta\omega\prod_{g=1}^{G}\exp\left[-\frac{W_{g,m}\left(x_1=0,x_f\right)}{\Delta\omega}\right].$$

Then

$$I_2=\exp\left[-\beta_m\int\limits_{0}^{x_f}\kappa_\omega^c\left(x'\right)\mathrm{d}x'\right]\cdot\prod_{g=1}^{G}\exp\left[-\frac{W_{g,m}\left(x_1=0,x_f\right)}{\Delta\omega}\right]. \tag{40}$$

Thus, the required formula for determination of the half-moment characteristic $M_{1,\Delta\omega}^{+}\left(x_f\right)$ has the following form:

$$M_{1,\Delta\omega}^{+}\left(x_f\right)=\sum_{m=1}^{2}\frac{1}{\beta_m}\sum_{i=1}^{i=f-1}\bar{I}_{b,\omega}\left(x_i\right)\left[W_m\left(x_{i+1},x_f\right)-W_m\left(x_i,x_f\right)\right]+$$

$$+\sum_{m=1}^{2}\exp\left[-\beta_m\int\limits_{0}^{x_f}\kappa_\omega^c\left(x'\right)\mathrm{d}x'\right]\prod_{g=1}^{G}\exp\left[-\frac{W_{g,m}\left(x_1=0,x_f\right)}{\Delta\omega}\right]\Delta\omega, \tag{41}$$

where the equivalent width may be calculated by the following approximate formulas [19]:

$$W_m^*\left(x_f,x_j\right)=A_{\Delta\omega,m}\Delta\omega=\left[1-T_{\Delta\omega,m}\left(x_f,x_j\right)\right]\Delta\omega=\left\{1-\prod_{k=1}^{K}\exp\left[-D_k^m\left(x_f,x_j\right)\right]\right\}\Delta\omega,$$

$$D_k^m\left(x_f,x_j\right)=\sqrt{\left(D_{L,k}^m\right)^2+\left(D_{D,k}^m\right)^2+\left(\frac{D_{L,k}^m D_{D,k}^m}{\chi_{m,k}}\right)^2},\qquad D_{L,k}^m=D_{L,k}^m\left(x_f,x_j\right)=\frac{\chi_{m,k}}{\sqrt{1+\left(\chi_{m,k}/4a_{L,k}^m\right)}},$$

$$D_{D,k}^m=D_{D,k}^m\left(x_f,x_j\right)=1.7a_{D,k}^m\sqrt{\ln\left[1+\left(\frac{\chi_{m,k}}{1.7a_{D,k}^m}\right)^2\right]},\qquad \chi_{m,k}=\chi_{m,k}\left(x_f,x_j\right)=\frac{\beta_m}{\Delta\omega}\int_{x_f}^{x_j}N_aF_k\left[T\left(x\right)\right]\mathrm{d}x,$$

Atomic parameters of the model are calculated as follows:

$$a_{L,k}^m=\frac{\beta_m}{\Delta\omega^2\chi_{m,k}}\int_{x_f}^{x_j}N_aF_k\left[T\left(x\right)\right]N_eG_{L,k}\left[T\left(x\right)\right]\mathrm{d}x,\qquad a_{D,k}^m=\frac{\beta_m}{\Delta\omega^2\chi_{m,k}}\int_{x_f}^{x_j}N_aF_k\left[T\left(x\right)\right]G_{D,k}\left[T\left(x\right)\right]\mathrm{d}x,$$

$$F_k\left(T\right)=\frac{1}{N_a}\sum_{j=1}^{N_k}\alpha_j=\frac{\pi e^2}{mc^2}\frac{1}{Q}\sum_{j=1}^{N_k}f_jg_j\exp\left(-\frac{E_j}{kT}\right),$$

$$G_{L,k}\left(T\right)=\frac{1}{N_e}\sum_{j=1}^{N_k}\gamma_{L,j}=\begin{cases}4.57\times10^{-17}T^{1/6}\sum_{j=1}^{N_k}C_{4,j}^a,\\ 1.11\times10^{-16}T^{-1/2}\sum_{j=1}^{N_k}C_{4,j}^i,\end{cases}$$

$$G_{D,k}\left(T\right)=\sum_{j=1}^{N_k}\gamma_{D,j}=3.58\times10^{-7}\sqrt{\frac{T}{M}}\sum_{j=1}^{N_k}\omega_{0,j},$$

where N_a, N_e are the concentrations of atoms and electrons; f_j is the oscillator strength; g_j is the statistical weight of the level with energy E_j; $C_{4,j}^a, C_{4,j}^i$ are the Stark constants for atomic (*a*) and ionic (*i*) lines; $\omega_{0,j}$ is wavenumber of the atomic line centre; *M* is atomic weigh; *k* is the Boltzmann constant; *Q* is the total partition function.

It must be stressed, that the group functions depend only on temperature and do not depend from population of absorbing energy levels. It means that at calculation of radiation transfer they can be determined at once beforehand. Using of the group functions allows reach appreciable economy of computer resources.

Examples of the use of the random models of atomic lines for radiation heat transfer problems are presented in Section 6.5.

4.3 The Macro-Random Model for Describing of Radiative Heat Transfer with Vibrational Band Structure

The general idea of the Macro-Random model is that each vibrational band is considered as an isolated line of absorption. The average transition in a spectral region is obtained by multiplication of separate band transitions. The macro-random model is computationally very effective as it allows determine averaged radiative characteristics without the use of *"line-by-line"* integration or any group models. The calculations are performed as if there is a single spectral region. For calculation of radiative heat transfer in non-uniform volumes the Curtis – Godson method is used.

Basic peculiarity of the Macro-Random model is the fact that the model is formulated with reference to one line within a spectral range $\Delta\omega$. Such a random model was introduced and justified above. Any contradiction with the traditional formulation of random models is not present, since in the given random model it is supposed, that in a considered spectral range $\Delta\omega$ only one spectral line has got from some large population, average distance between lines in which equally $\Delta\omega$.

The opportunity of application of such a model to calculation of averaged spectral characteristics was checked by comparison with results of "line-by-line" calculations [20,21].

As it was mentioned above, the basic idea of the macro-random model is that the vibrational band averaged on rotational structure is considered as an isolated line of absorption. To use the generalized random model it is necessary to set a contour function of the absorption band $f(\nu,\nu',S,\gamma')$, where the intensity S and the half-width γ are parameters, specifying the integrated absorption coefficient and half-width of the band. It is necessary also to fulfil the condition that the half-width of the band should be much less, than size of the spectral range $\Delta\omega$.

In the study the approximation of the function of vibrational bands absorption offered by Edwards [22] is used:

$$\kappa(\nu,\nu') = \frac{C_1}{C_3}\exp\left[-\frac{|\nu-\nu'|}{C_3}\right], \tag{42}$$

where ν' is the centre of the band of absorption, C_1 and C_2 are parameters, determining intensity and half-width of the band. Let us assume that $\nu' = 0$, then easily to show that

$$S = 2\int_0^\infty \frac{C_1}{C_3}\exp\left(-\frac{\nu}{C_3}\right)d\nu = 2C_1. \tag{43}$$

The approximation (42) allows to accept that $\gamma' = C_3$, then

$$\kappa(\nu,\nu') = \frac{S'}{2\gamma'}\exp\left[-\frac{|\nu-\nu'|}{\gamma'}\right]. \tag{44}$$

If to assume, that the probability density of intensities distribution of vibrational bands has the same kind, as well as for rotational lines in vibrational bands, i.e.

$$p(S') = \frac{1}{S_g}\exp\left(-\frac{S'}{S_g}\right),$$

then for obtaining the required equivalent width it is necessary to calculate integral (18), by substituting in it the following contour function

$$f\left(\nu,\nu',\gamma_g\right)=\frac{1}{2\gamma'}\exp\left[-\frac{|\nu-\nu'|}{\gamma_g}\right].$$

Then
$$W_g=2\gamma_g\ln\left(1+\frac{S_gL}{2\gamma_g}\right). \tag{45}$$

Thus, average transmission of the spectral range $\Delta\omega$, containing vibrational bands can be calculated under the formula

$$\overline{T}_{\Delta\omega}=\prod_{g=1}^{G}\exp\left(-\frac{W_g}{\Delta\omega}\right),$$

where the equivalent width of the *g*-th vibrational band W_g can be calculated under the formula (45).

To calculate an average transmission of a non-uniform optical path the Curtis – Godson method is used [23,24]. The general idea of this method consists in introduction for each line (or each band) averaged parameters on the optical path: average intensity of the line $\overline{S}_g$ and the average half-width $\overline{\gamma}_g$.

The introduction of averaged parameters $\overline{S}_g$ and $\overline{\gamma}_g$ actually means transition to consideration of some effective optical path. As it was offered by Curtis and Godson, to find averaged parameters it is necessary to equate the integrated absorption (or, that same, equivalent width) of the effective optical path and one for the true non-uniform path in two limiting cases: in the cases of optically thin and optically thick layers.

Let us consider obtaining of the Curtis – Godson relations with reference to one isolated line. An exact expression for the equivalent width has the following form:

$$W_T=\int_{-\infty}^{+\infty}\left\{1-\exp\left[-\int_L\kappa\left(\nu,S(x),\gamma(x)\right)dx\right]\right\}d\nu=2\int_0^{\infty}\left\{1-\exp\left[-\int_L\kappa\left(\nu,S(x),\gamma(x)\right)dx\right]\right\}d\nu \tag{46}$$

Then, for the effective homogeneous path one can write

$$\overline{W}=2\int_0^{\infty}\left\{1-\exp\left[-\kappa\left(\nu,\overline{S},\overline{\gamma}\right)L\right]\right\}d\nu. \tag{47}$$

In either case, the wave number ν is measured from centre of the line.

For obtaining of the averaged parameters $\overline{S}$ and $\overline{\gamma}$ the following condition $W_T\approx\overline{W}$ must be satisfied, or

$$\int_0^{\infty}\exp\left[-\kappa\left(\nu,\overline{S},\overline{\gamma}\right)L\right]d\nu\approx\int_0^{\infty}\exp\left[-\int_L\kappa\left(\nu,S(x),\gamma(x)\right)dx\right]d\nu. \tag{48}$$

It is obvious, that from this relation it is possible to determine required values only approximately. Let us consider the following two opposite approximations: the optically thin $\left(\kappa\left(\nu,\overline{S},\overline{\gamma}\right)L\ll 1\right)$ and the optically thick $\left(\kappa\left(\nu,\overline{S},\overline{\gamma}\right)L\gg 1\right)$ paths.

The equivalent formulation for these approximations looks as follows:

$$\int_L \kappa\left(\nu, S(x), \gamma(x)\right) dx \gg 1 \quad \text{for any } \nu, \text{ and } \int_L \kappa\left(\nu, S(x), \gamma(x)\right) dx \ll 1, \text{ at } \nu < \nu_1 .$$

The sense of the last inequality is that one can find the wave number $\nu_1 \gg \max\{\gamma(x)\}$, at which the optical thickness of the volume will become less unit. In this case the radiation transfer must be investigated only in far wings of the line ($\nu > \nu_1$).

Let us consider the following integral

$$\int_0^\infty \left\{ \exp\left[-\kappa\left(\nu, \overline{S}, \overline{\gamma}\right) L \right] - \exp\left[-\int_L \kappa\left(\nu, S(x), \gamma(x)\right) dx \right] \right\} d\nu = 0 . \tag{49}$$

In the case of optically thin path one can obtain

$$L \int_0^\infty \kappa\left(\nu, \overline{S}, \overline{\gamma}\right) d\nu = \int_L dx \int_0^\infty \kappa\left(\nu, S(x), \gamma(x)\right) d\nu$$

or using the definition of intensity (19):

$$\overline{S} = \frac{1}{L} \int_L S(x) dx . \tag{50}$$

In the case of optically thick path (at $\nu < \nu_1$) the total absorption of radiation will be observed, so both exponents in (49) are practically equal to zero and it is possible to write the following approximate relation:

$$\int_{\nu_1}^\infty \left\{ \exp\left[-\kappa\left(\nu, \overline{S}, \overline{\gamma}\right) L \right] - \exp\left[-\int_L \kappa\left(\nu, S(x), \gamma(x)\right) dx \right] \right\} d\nu = 0 . \tag{51}$$

For some kinds of function of the line contour instead of (51) it is possible to require, that integrand expression was equalled to zero at any wave number, namely

$$\exp\left[-\kappa\left(\nu, \overline{S}, \overline{\gamma}\right) L \right] = \exp\left[-\int_L \kappa\left(\nu, S(x), \gamma(x)\right) dx \right]$$

or

$$\kappa\left(\nu, \overline{S}, \overline{\gamma}\right) = \frac{1}{L} \int_L \kappa\left(\nu, S(x), \gamma(x)\right) dx .$$

For example, for the Lorentzian line one can obtain the following well known relation (with the account of $\nu_1 \gg \max\{\gamma(x)\}$):

$$\overline{S}\,\overline{\gamma} = \frac{1}{L} \int_L S(x) \gamma(x) dx . \tag{52}$$

The situation is different for lines with exponential contours. It is not here possible to equate to zero integrand function. Therefore for averaging half-width it is necessary to use an additional approximation.

The integral (51) can be presented in the following form:

$$\int_{\nu_1}^{\nu_2}\left\{\exp\left[-\kappa\left(\nu,\bar{S},\bar{\gamma}\right)L\right]-\exp\left[-\int_L\kappa\left(\nu,S(x),\gamma(x)\right)dx\right]\right\}d\nu=0\,, \tag{53}$$

where ν_2 is the wave number, at which the exponent in (53) becomes equal to zero by virtue of exponential reduction of absorption coefficient at large ν. Then, started from the theorem about average, it is possible to prove, that the integrand expression will be equal to zero though in one point ν^* of the spectral range $[\nu_1,\nu_2]$, that is

$$\kappa\left(\nu^*,\bar{S},\bar{\gamma}\right)=\frac{1}{L}\int_L\kappa\left(\nu^*,S(x),\gamma(x)\right)dx$$

or

$$\frac{\bar{S}}{2\bar{\gamma}}\exp\left(-\frac{\nu^*}{\bar{\gamma}}\right)=\frac{1}{L}\int_L\frac{S(x)}{2\gamma(x)}\exp\left(-\frac{\nu^*}{\gamma(x)}\right)dx\,.$$

Now, one can replace the function $\gamma(x)$ in the exponent by its average value $\bar{\gamma}$

$$\frac{1}{\bar{\gamma}}=\frac{1}{\bar{S}L}\int_L\frac{S(x)}{\gamma(x)}dx\,. \tag{54}$$

5.0 EXAMPLES OF THE USE OF THE RANDOM MODELS OF MOLECULAR LINES FOR RADIATION HEAT TRANSFER PROBLEMS ARE PRESENTED IN SECTION 6.6. 5.0 THE MONTE-CARLO METHODS

Monte-Carlo simulation methods have great potential for creation of the universal computational codes intended for prediction of spectral emissivity of different aerospace objects. First of all, these are: light-scattering plumes of rocket motors (signatures of rocket plumes), emissivities of entering space vehicles in light-scattering and non-scattering atmospheres, meteors, etc. Performance of modern computers and parallel computing technologies allow solve radically the main problem of the Monte-Carlo imitating algorithms, namely reduce dispersion of numerical simulation results.

Basic Monte-Carlo imitative algorithms of radiation transfer of heat radiation in arbitrary inhomogeneous volumes of light-scattering media will be considered in sections 5.1–5.8. Next a peculiarity of the Monte-Carlo algorithms to solve some applied problems which are of practical interest for aerospace applications will be considered in sections 5.9–5.10.

Investigations of efficiency of different simulation algorithms with reference to problem of calculation of spectral signatures were performed in [25–28]. Analysis of five simulation algorithms is given in [25]:

- The LBL-method of integration of radiation heat transfer equation on spectrum of rotational lines;
- Hybrid statistical model;
- Method of smoothed coefficients;

- The two-group method;
- The LBL-method with small number of trajectories of photons.

Brief description of the algorithms is presented below (sections 5.1–5.5). Further developments of the imitative algorithms are presented in sections 5.6–5.10.

5.1 Line-by-line integration of radiation heat transfer equation on spectrum of rotational lines

The given spectral range is divided on N of spectral sub regions $\Delta\omega_g$. In limits of each sub region the following averaged absorption coefficient is introduced:

$$\kappa_g = \frac{1}{\Delta\omega_g} \int_{\Delta\omega_g} \left[\kappa^p(\omega) + \kappa^c(\omega) + \sum_i^{N_l} \kappa_i^l(\omega) \right] d\omega, \tag{1}$$

where $\kappa_i^l(\omega)$ is the spectral volumetric absorption coefficient of i-th line; N_l is the number of lines located in the sub region $\Delta\omega_g$; $\kappa^c(\omega)$, $\kappa^p(\omega)$ are the spectral volumetric absorption coefficient of gas (in continuum spectra) and solid (liquid) particles.

Let us assume, that all lines have Lorentzian contour, therefore

$$\kappa_i(\omega) = \frac{S_i \gamma_{L,i}}{\pi \left[\left(\omega - \omega_{0,i}\right)^2 + \gamma_{L,i}^2 \right]}, \tag{2}$$

where S_i, γ_{Li} are the intensity and half-width of i-th Lorentzian line; $\omega_{0,i}$ is the wavenumber of centre of the i-th line.
Imitative Monte-Carlo simulation of photon trajectories can be performed for each spectral group $\Delta\omega_g$ as for any "grey" medium [28]. It should be emphasize, that in the case of non-uniform medium coefficients κ_g, $\kappa^p, \kappa_i^c, \kappa^l, \kappa_i(\omega)$; S_i, γ are functions of coordinates.

5.2 Hybrid Statistical Method [26]

The idea of the method is extremely simple. The Monte-Carlo imitative algorithms are applied not for simulation of monochromatic photon groups, but for simulation of the propagation of photon groups whose energy is determined by averaging over spectral band. The averaged energy of photon groups for various optical paths is determined with the use of random models of real linear spectra. The Curtis – Godson method is used to take into account inhomogeneity of the optical path. Detailed description of the random models is presented in Chapter 3. The following works [17,19] can be recommended for more deep studying of the models.

This approach has the following advantages:

3) The integration over wave number in this approach is the analytical one, and it can be performed for a separate spectral band that contains from one to hundreds and thousands of spectral lines. Another words, it means that the spectral problem is solved just once for the entire spectral band.
4) To implement this random method into regular Monte-Carlo algorithm, it is enough to modify the subroutine for calculation of free path of photon groups and insignificantly the geometrical module.

5) The type of the spectral lines taking into account (atomic or molecular), their location in spectral region (regular or chaotic), their contours (the Lorenz, the Doppler, the Voigt) are of no significance. All the above-mentioned peculiarities are taken into account by the random models that can be used without any restrictions.

6) If it is necessary to take into account strong inhomogeneity of optical paths, the Curtis – Godson approximation can be applied with any other model that would describe the environmental inhomogeneity along the optical path more adequately [23,24].

7) The method does not lose any advantages as compared with the Monte-Carlo simulation method, in particular, in respect to solution of problems for volumes with complex geometries.

The drawback of the hybrid Monte-Carlo simulation algorithm is the typical for the classical imitative Monte-Carlo algorithms and random models. These are:

1) High computational intensity of the Monte-Carlo algorithms;

2) The intrinsic error of random band models which does not allow an asymptotic transition to precise line-by-line integration.

Let us now consider some details of the hybrid method. As it was mentioned above, the basis of the method is the simplest Monte-Carlo simulation method. This method simulates trajectories of photon groups inside each homogeneous element of volume, which is introduced by finite difference grid overlying the whole calculation domain.

We consider fixed spectral band $\Delta\omega_g$ after dividing the spectrum under consideration into such bands. We can enter, for example, ~ $50 \div 250$ cm^{-1} for $\Delta\omega_g$ in the infra-red region of the spectrum. Spectral lines of molecules and continuous (or quasi-continuous) absorption spectra may exist in each band.

Calculation by the hybrid statistical method starts from the formulation of the position vector of linear homogeneous section in the direction of motion of corresponding photons in the inhomogeneous media under consideration (l_j, $j = 1,2,3,...,N$; $l_1 = 0$; l_N is the coordinate of the point of intersection between the beam and the boundary surface). The nodes of the calculation grid l_j correspond to the points of intersection between the photon direction with all the boundary surfaces of homogeneous volume elements.

Each homogeneous volume element has associated coordinates l_j, vectors of gas temperature T_j^g, temperatures of particles T_j^p, molar concentrations of optically active components of gas mixture $x_{k,j}^g$, concentrations of optically active liquid and solid mixture components $n_{k,j}^p$ ($n_{k,j}^p$ is the number density of particles of given dimensions, if the mixture is dispersive, then $n_{k,j}^p$ is the number density of particles with a certain average dimension), and the total pressure in gas mixture p_j. The dimensionality of vectors $T_j^g, T_j^p, x_{k,j}^g, n_{k,j}^p$ amounts to N–1, since the properties inside each elementary zone are assumed to be constant.

This allows calculations of the following optical properties that determine the character of radiation transfer along the beam within the limits of each section of vector l_j :

3) Coefficients of absorption κ_j^p and scattering σ_j^p of the condensed phase (in this particular case the calculation is made according to the Mie theory [29]), as well as the scattering phase- function or average scattering cosine $\overline{\mu}_j$ that characterizes the extent of asymmetry of the phase function. The given functions are considered to be independent of wave number within the limits of spectral band $\Delta\omega_g$;

4) Absorption coefficients κ_j^c in the continuous spectrum;

5) The average absorption coefficient in spectral lines $(S/d)_{k,b,j}$;

6) Line broadening parameter $\beta_{k,b,j}$;

7) Effective pressure $(P_e)_{k,b,j}$.

The average absorption coefficient in the spectral lines, the spectral line broadening parameter and the effective pressure are calculated for each molecular band *b* of each component *k* that contributes to radiation absorption in band $\Delta\omega_g$. These functions were calculated using the wide band model [22].

The next stage of the algorithm is to build a vector of effective optical thicknesses for each band of the spectral lines, for which the Curtis – Godson method is used. Let us assume that collision broadening dominates so the lines have a Lorentzian profile:

$$\tau_{k,b,j} = \frac{\chi_{k,b,j}}{\sqrt{1+\dfrac{\chi_{k,b,j}}{4a^L_{k,b,j}}}}, \tag{3}$$

$$\chi_{k,b,j} = \int_{l_1}^{l_j} \rho_k \left(\frac{S}{d}\right)_{k,b} dl \approx \sum_{m=2}^{j} \rho_{k,m} \left(\frac{S}{d}\right)_{k,b,m} (l_m - l_{m-1}), \tag{4}$$

$$a^L_{k,b,j} = \left\langle \left(\frac{\gamma_L}{d}\right)_{k,b,j} \right\rangle = \frac{\displaystyle\int_{l_1}^{l_j} \left(\frac{S}{d}\right)_{k,b} \left(\frac{\gamma_L}{d}\right)_{k,b} \rho_k \mathrm{d}l}{\displaystyle\int_{l_1}^{l_j} \left(\frac{S}{d}\right)_{k,b} \rho_k \mathrm{d}l}, \tag{5}$$

where ρ_k is the density of the *k*-th component of the mixture; S, γ are the averaged intensity and half-width of rotational lines in the *b*-th lines band of the *k*-th species.

Assuming that the principle of statistical independence of transmission in spectral line bands is correct, and accounting for continuum absorption, the full optical thickness is

$$\tau_j^a = \sum_k \sum_b \tau_{k,b,j} + \sum_k \tau_{k,j}^c + \sum_k \tau_j^p , \tag{6}$$

$$\tau^c_{k,j} = \sum_{m=2}^{j} \kappa^c_m \left(l_m - l_{m-1}\right), \quad \tau^p_j = \sum_{m=2}^{j} \kappa^p_m \left(l_m - l_{m-1}\right). \tag{7}$$

If the Doppler broadening dominates, the calculation of $\tau_{k,b,j}$ is changed by substituting the Doppler profile for Equation (3) (see, for example, [19]).

Simultaneously with calculation of the optical absorption thickness, calculation of optical scattering thickness is performed as following

$$\tau^s_j = \sum_{m=2}^{j} \sigma^p_m \left(l_m - l_{m-1}\right), \tag{8}$$

which enables later estimation of the probability of absorption (or scattering) of photons by particles of a media.

The photons mean free path is identified as usual. However, to find the point of collision between the photons and particles of the environment, additional calculations have to be made. The main reason for this is the non-linear relationship for transmission in spectral groups with spectral lines (the square-root low for the equivalent width of molecular lines [17]). This is because inequality of total transmission of the entire section to the sum of individual transmissions of its components.

Assume that after generation of a random number it was established that optical thickness τ^c, that corresponds to the mean free path, satisfies the inequality:

$$\tau^t_j \le \tau^c \le \tau^t_{j+1}, \quad \tau^t_j = \tau^a_j + \tau^s_j. \tag{9}$$

It is then necessary to find coordinate l^c corresponding to value τ^c. In a general, it is necessary to organize an iterative process to find the value of l^c. A non-iterative method can be used if it was assumed that Equation (9) corresponds to a linear relationship between the optical thickness and the physical coordinate which is accurate for low optical thicknesses of the volume elements. Then:

$$l^c = l_j + \frac{\left(l_{j+1} - l_j\right)\left(\tau^c - \tau^t_j\right)}{\left(\tau^t_{j+1} - \tau^t_j\right)}. \tag{10}$$

Now one can estimate the probability of absorption (scattering) in the point where the photon collides with particles. As opposed to the Monte-Carlo calculation of monochromatic radiation transfer, where the probability of absorption (scattering) is estimated as a relation of the absorption (scattering) coefficient to the full attenuation coefficient, in this case the procedure applies to corresponding optical thicknesses. For instance, the probability of scattering is estimated as follows

$$P_s = \frac{\tau^s_c}{\tau^s_c + \tau^a_c}, \quad \tau^s_c = \tau^s_{j+1} - \left(l_{j+1} - l^c\right)\sigma^p_j, \quad \tau^a_c = \tau^a_j + \frac{l^c - l_j}{l_{j+1} - l_j}\left(\tau^a_{j+1} - \tau^a_j\right).$$

The rest of the Monte-Carlo procedure is the same as for monochromatic radiation.

There is one more peculiarity of the calculation algorithm with molecular lines. It is connected with the problem of a choice of energy for each simulated photon group.

There are two algorithms. In the first algorithm the energy is determined as uniform for all photon groups. This algorithm is realized in the following steps:

1. The integrated emissivity E of the whole researched volume V and separate its parts E_n (on which the volume is broken by the finite difference grid) are calculated;
2. The energy of each photon group e_f is determined by dividing of complete energy E on quantity of simulated groups N_f;
3. The relative probability p_n of photon emission in different volume elements is determined by the relation of the emissivity of the given zone to integrated emissivity: $p_n = E_n / E$. According to this relative probability number of photon groups emitted by the given volume element is determined as follows: $N_{f,n} = p_n N_f$.

So, in this algorithm all photon groups have identical energy, but different volume zones emit various number of the photon groups.

In the second algorithm each photon group gains different energy, determined by the emissivity of given spatial zone (volume element) from which this photon group is emitted. In this algorithm it is expedient for each spatial zone to determine identical number of emitted photon groups. This algorithm is realized in the following steps:

1. The values E_n and E are calculated;
2. The number of photon groups emitted by each spatial zone is determined under the formula
$$N_{f,n} = N_f / N_V ,$$
where N_V is the number of spatial zones.
3. The energy of the given photon group is calculated under the formula
$$e_f = E_n / N_{f,n} .$$

Both stated algorithms can be modified by weight algorithm of modelling, when the energy of groups photon changes during collisions [1].

The mentioned above peculiarity consists in a way of estimation of energy E_n:

$$E_n = 4\pi \int_{V_n} \int_{\Delta\omega_g} \kappa(\omega) J_{b,\omega} \mathrm{d}\omega \mathrm{d}V , \tag{11}$$

where V_n is the volume of n-th spatial zone; J_b is the spectral intensity of the Planck radiation; $\kappa(\omega)$ is the volumetric spectral absorption coefficient. As properties of medium are averaged in limits of each zone, and the spectral ranges $\Delta\omega_g$ are usually slender, so in their limits with good accuracy it is possible to enter average spectral Planck intensity

$$\overline{J}_{b,n} = \frac{1}{\Delta\omega_g} \int_{\Delta\omega_g} J_{b,\omega,n} \mathrm{d}\omega . \tag{12}$$

Then the expression (11) is much simplified

$$E_n = 4\pi \bar{J}_{b,n} V_n \int\limits_{\Delta\omega_g} \kappa_{\omega,n} d\omega \,. \tag{13}$$

If the volumetric spectral absorption coefficient $\bar{\kappa}_n$ does not depend on wave number in limits $\Delta\omega_g$ (approximation of "grey" medium), then

$$E_n = 4\pi \bar{J}_{b,n} \cdot \Delta\omega_g V_n \bar{\kappa}_n \,. \tag{14}$$

When spectral region $\Delta\omega_g$ contains N_l spectral lines, then integral in the formula (13) may be calculated as follows:

$$\int\limits_{\Delta\omega_g} \kappa_{\omega,n} d\omega = \kappa_n^p \Delta\omega_g + \kappa_n^c \Delta\omega_g + \int\limits_{\Delta\omega_g} \sum_{i=1}^{N_l} \kappa_{i,n}^l(\omega) \approx \kappa_n^p \Delta\omega_g + \kappa_n^c \Delta\omega_g + \sum_{i=1}^{N_l} S_{i,n} \,, \tag{15}$$

It is assumed also, that the half-width of lines (with spectral volumetric absorption coefficient $\kappa_{i,n}^l(\omega)$) satisfy to the following condition:

$$\gamma_{i,n} \ll \Delta\omega_g \,,$$

then

$$S_{i,n} = \int\limits_0^\infty \kappa_{i,n}^l(\omega) d\omega \approx \int\limits_{\Delta\omega_g} \kappa_{i,n}^l(\omega) d\omega \,. \tag{16}$$

Thus, the integrated emissivity is calculated as follows:

$$E_n = 4\pi \bar{J}_{b,n} V_n \left(\kappa_n^p \Delta\omega_g + \kappa_n^c \Delta\omega_g + \sum_{i=1}^{N_l} S_{i,n} \right). \tag{17}$$

Formulas (13) and (17) are easily generalized on the case, when the temperatures of gas and solid (liquid) phases differ:

$$E_n = 4\pi V_n \left(\bar{J}_{b,n}^p \bar{\kappa}_n^p + \bar{J}_{b,n}^g \bar{\kappa}_n^g \right) \Delta\omega_g \,,$$

or

$$E_n = 4\pi V_n \left[\bar{J}_{b,n}^p \bar{\kappa}_n^p \Delta\omega_g + \bar{J}_{b,n}^g \left(\kappa_n^c \Delta\omega_g + \sum_{i=1}^{N_l} S_{i,n} \right) \right], \tag{18}$$

where $\bar{J}_{b,n}^p, \bar{J}_{b,n}^g$ are the Planck intensities at temperatures of particles T^p and gas T^g; $\bar{\kappa}_n^p, \bar{\kappa}_n^g$ are the overage volume absorption coefficients of particles and gas.

It is necessary to pay attention on the fact, that the stated way of estimation of emissivity is well reasonable in cases, when the volume V_n is optically thin. If the optical thickness τ_n of the volume V_n does not satisfy to this condition, i.e. $\tau_n > 1$, the specified way of calculation of emissivity can result in significant errors (in particular by use of a hybrid Monte-Carlo method).

5.3 Method of the smoothed coefficients

This method is actually equivalent to the hybrid Monte-Carlo method, but here the following simplification is used

$$\tau_{k,b,j} = \chi_{k,b,j}\,. \tag{19}$$

This relation is correct under the following condition:

$$\frac{\chi_{k,b,j}}{4a^{L}_{k,b,j}} \ll 1.$$

It is obvious, that with increase of optical thickness it is necessary to expect increase of the error of the method. However, as it was shown in [25], at very large optical thickness this method gives more physically reasonable result, than hybrid Monte-Carlo method.

5.4 The two-group method

Let spectral range $\Delta\omega_g$ contains N_l molecular lines. Let us assume, that integrated emission in the given spectral range does not depend on location of the molecular lines.

Average intensity and half-width for all lines from the range $\Delta\omega_g$ in each spatial zone is calculated as follows:

$$\langle S_n \rangle = \frac{1}{N_l}\sum_{i}^{N_l} S_{i,n}, \quad \langle \gamma_n \rangle = \frac{1}{N_l}\sum_{i}^{N_l} \gamma_{i,n}\,. \tag{20}$$

Then the average half-width on all spatial zones is determined as follows:

$$\langle \gamma \rangle = \frac{1}{N_n}\sum_{n=1}^{N_n} \langle \gamma_n \rangle\,. \tag{21}$$

Let us enter two spectral ranges inside the spectral range $\Delta\omega_g$ such that:

$$\begin{aligned} \Delta\omega_1 &= \min\left\{2N_l\langle\gamma\rangle, \Delta\omega_g\right\}, \\ \Delta\omega_2 &= \Delta\omega_g - \Delta\omega_1. \end{aligned} \tag{22}$$

The average absorption coefficient in the spectral ranges $\Delta\omega_1$ and $\Delta\omega_2$ are determined under the formulas

$$\bar{\kappa}_{1,n} = \kappa^{p}_{n} + \kappa^{c}_{n} + \frac{\langle S_n \rangle}{\pi\langle\gamma\rangle}, \quad \bar{\kappa}_{2,n} = \kappa^{p}_{n} + \kappa^{c}_{n} + \left(\langle S_n \rangle N - \bar{\kappa}_{1,n}\Delta\omega_1\right)\frac{1}{\Delta\omega_2}\,. \tag{23}$$

Now everything is ready to imitative simulation of the two group photons with the averaged absorption coefficients (23). Emissivity of each volume elements is determined in this case as follows:

- $E_n = 4\pi V_n \bar{J}_{b,n}\bar{\kappa}_{1,n}\Delta\omega_1$ – for the first spectral region;
- $E_n = 4\pi V_n \bar{J}_{b,n}\bar{\kappa}_{2,n}\Delta\omega_2$ – for the second spectral region.

5.5 Line-by-line integration with little number of trajectories

Estimations of dispersion of direct statistical simulation results, and also experience, accumulated at the solution of similar problems in "grey" statement show, that for obtaining of satisfactory accuracy of the simulation it is enough, as a rule, to simulate about $N_f = 10^4 \div 5 \times 10^4$ trajectories. For the case of relative low albedo ($\omega = \dfrac{\sigma}{\sigma + \kappa} < 0.9$) with moderate optical thickness ($\tau < 1$) this number can be reduced yet by the order. And on the contrary, for multi-scattering medium of large optical thickness this number is necessary yet to increase.

When there is a need to find averaged over the spectral region $\Delta\omega_g$ radiating characteristics, it is possible to use the following algorithm. Let us try to find the solution of the problem, simulating trajectories only of $N_f \sim 10^4$ photon groups. The energy of each new photon group will be estimated statistically. For this purpose spectral absorption coefficient is calculated in any spectral point inside the region $\Delta\omega_g$.

The stated algorithm can be modified as follows. We shall break the range $\Delta\omega_g$ on elementary spectral sub regions. The number of these sub regions must be sufficient for the detailed description of line structure of the spectrum. For example, at $\Delta\omega_g = 20\,\text{cm}^{-1}$ and average size of half-width $\gamma = 0.1\,\text{cm}^{-1}$ it is enough to enter ~ 1000 spectral sub regions $\Delta\omega'_g$.

Further to calculate averaged radiating characteristics one can apply usual procedures of line-by-line integration, but within the bounds of the each spectral sub region $\Delta\omega'_g$ to simulate trajectories not of ~ 10^4 photon groups (as in the regular line-by-line method), but only ~10–15 photon groups. It should be stressed, that it is impossible to determine the spectral characteristics inside $\Delta\omega_g$ by this way, but the averaged characteristics in the region $\Delta\omega_g$ can be obtained with rather good accuracy.

5.6 The Monte-Carlo imitative method based on the Maximum Cross Section (MCS) method

Regular imitative Monte-Carlo algorithms considered above were developed for calculation of averaged radiation transfer over rotational lines in spectral range $\Delta\omega_g$ on the orthogonal calculation grids in 2D cylindrical geometry. These imitative algorithms were used for test calculations of signatures of model rocket motor plumes [28] and for comparison with computational data [30]. These algorithms were used also at study of different optical models for prediction of rocket motor plume signatures [27]. It was shown, that considered imitative Monte-Carlo algorithms can be used quite really even with "line-by-line" (LBL) models of rotational line structure. Development of these imitative Monte-Carlo algorithms with reference to non-orthogonal grids, which are usually used at the solution of gasdynamic problems, is presented in the Ref. [31]. Three imitative algorithms on non-orthogonal grids were considered there:

8) The LBL-method based on the imitative Monte-Carlo algorithm and the MCS method;
9) The LBL-method based on the imitative Monte-Carlo algorithm and the method of quasi-random sampling for formation of straight-line trajectory segments (further we will use also the term "direct Monte-Carlo simulation");
10) Hybrid method based on the method of quasi-random sampling.

The Maximum Cross-Section method is based on the obvious statement that adding any quantity of δ-scatterer (δ-diffuser of light) into investigated volume of the light-scattering media does not change the process of photons diffusion (by the definition, the δ-scatterer is the scatterer without changing direction).

Let us introduce the maximum total extinction coefficient of the multi-component multiphase polydisperse medium, using the following definition:

$$\beta_{t,\max} = \max_{l}\left\{\beta_{t,l}\right\}, \quad \beta_{t,l} = \kappa_{g,l} + \kappa_{p,l} + \sigma_l , \tag{24}$$

where l is the number of the volume elements defined by four nodes indexes of introduced calculation grid; $\kappa_{g,l}, \kappa_{p,l}$ are the gas and particles absorption coefficients; σ_l is the averaged scattering coefficient of polydisperse solid phase; $\beta_{t,l}$ is the extinction coefficient.

For each *l*-th elementary volume of the computational grid there may be introduced also the δ-scattering coefficient:

$$\beta_{\delta,l} = \beta_{t,\max} - \beta_{t,l} . \tag{25}$$

The use of introduced functions ($\beta_{t,\max}$, $\beta_{t,l}$, and $\beta_{\delta,l}$) allows simulate the photons diffusion in a heterogeneous medium as well as in a homogeneous one. In so doing it is agreed that at each photon's collision with particles of the medium the δ-scattering occurs with the probability of $\beta_{\delta,l}/\beta_{t,\max}$, and the real interaction occurs with the probability of $1-\beta_{\delta,l}/\beta_{t,\max}$. Another words, in the maximum cross-section method the delta-scattering probability is determined as $p_\delta = \beta_\delta/\beta_{t,\max}$, and the real interaction probability is determined as $p_{s,\kappa} = 1 - p_\delta$. Thus for simulation of collision type one should check the fact of satisfaction of the following condition $p_\delta > \gamma$ (γ is the quasi-random number from the equally probable distribution in segment [0,1]). In this case the delta-scattering has been occurred. Otherwise the true collision has been occurred.

The true collision may be both absorption and scatter. Generating new random number γ and comparing it with the scattering probability $p_s = \sigma/\beta_t$ one can make a conclusion concerning the type of the collision. If $\gamma < p_s$ there has been occurred scattering; and if $\gamma > p_s$ or, what is the same, $\gamma < p_\kappa = 1 - p_s$ it is considered that there has been occurred absorption.

The use of the maximum cross-section method with the transport approximation of scattering processes simplifies simulation algorithm to a greater degree. The total "delta-scattering" coefficient can be presented in these cases as follows:

$$\beta_\delta = \beta_{t,\max} - \left[\kappa + (1-\bar{\mu})\sigma\right] \quad \text{or} \quad \beta_\delta = \beta_{t,\max} - \beta_t + \sigma\bar{\mu} .$$

Another word, in the transport approximation anisotropy of any scattering may be taken into account at the level of collision type modeling (true or not the given collision). If the following inequality

$$p_{\delta,s} = \frac{\sigma - \sigma(1-\bar{\mu})}{\sigma} = \bar{\mu} > \gamma ,$$

is true, then this is the δ-scattering; and if $p_{\delta,s} < \gamma$ is true, then this is the real scattering.

5.7 Imitative Monte-Carlo algorithm based on the quasi-random sampling of photon trajectory parameters

To calculate radiation transfer through any optical path with directional vector $\vec{\Omega}$ there is necessity to know optical properties along this path. For this purposes the coordinates of the ray $\vec{\Omega}$ intersections with

all surfaces of the spatial finite-difference mesh should be calculated. This is illustrated in Figure 3.9. Relations of the analytical geometry should be used for these purposes. As it was shown above, at consideration the ray-tracing method (see section 3.3), this algorithm is not effective due to very high laboriousness, especially for non-structured meshes. Algorithm of the quasi-random sampling can be used with the Monte-Carlo imitative algorithms, as it was used with ray-tracing method.

5.8 The hybrid method based on the quasi-random sampling method

This is the hybrid simulation method (see section 5.2 and [25,26]), which is united in the given case together with the method of quasi-random sampling.

5.9 Three-dimensional simulation algorithms

Imitative algorithms considered above can be applied for prediction of spectral emissivity of axially-symmetric volumes, for examples, rocket plumes. Calculation of the directed radiating ability of a single plume is of significant practical interest for comparison of the results with experimental and calculation data of other authors. The overwhelming majority of all calculations were based on the model of axially symmetric plume [26–28,31]. But very often radiating aerospace objects must be considered as the three-dimensional objects. For example, heat radiation of single and multi-block plumes or light scattering volumes illuminated by sources of external radiation, for example sunny [32]. It is presumed in this case, that the plane-parallel flux of radiation illuminates one of the planes of calculation area under any angle of attack. Heat radiation of Sun can be compared to radiation of absolutely black body at temperature ~ 6000 K. Spectral dependence of scattered sunlight is formed under action of absorption of gas and solid phases of the plume.

Spectral radiating ability of multi-block jets even in relation to self-radiation is the three-dimensional problem. Three-dimensional imitative Monte-Carlo codes were developed and tested in [33]. Figures 6.40–6.44 of section 6.7 show example of distribution of gas temperatures and concentration of condensed phase in three-block plumes. Examples of numerical simulation results for such a configuration of multi-block radiating plume are also presented in the section 6.7.

5.10 Monte-Carlo Local Estimation of Directional Emissivity (MCLEDE)

The Monte-Carlo method considered above is useful when it is necessary to find the angular distribution of radiation intensity over whole solid angle. In this case each photon leaving the radiating volume adds its contribution into the number of the photons moving in a concrete zone of calculation grid over angular variables, and at the contraction of this angular zone it is necessary to increase the number of modelled photons so that the statistical error of the calculation won't increase. However, in practice it is often necessary to know the radiation intensity in the strictly determined direction. In that case it is possible to speed up the performance of the calculation code considerably, at the same time having made the angular range infinitesimal. Numerical simulation algorithm for such a case was presented in [34]. Here we will consider a substantiation of the algorithm.

Suppose we need to find radiation intensity in any strictly determined direction μ_1. We shall establish counters not for the number N of the photons moving in the range $d\mu$, but for their density $N/d\mu$. For each photon we shall set initial energy E_0. After each collision the energy of a photon will decrease: $E = \omega E_0$. That corresponds to the estimation of probability for the given photon to continue the movement in any direction (for the case of isotropic scattering).

If we count the photons moving in the range $[\mu_1 - d\mu;\ \mu_1 + d\mu]$, the photon with energy $E d\mu$ will move in the direction μ_1, and the energy of the photons moving in all directions $\mu_2 \neq \mu_1$ will be $E \cdot (1 - d\mu)$. The direction μ_2 is determined by any algorithm of scattering simulation. After that it is necessary to trace both of these photons.

The photon with the energy $E d\mu = \omega E_0 d\mu$ moves in the direction μ_1 before the following collision occurs. After this collision the energy of the photon, moving along μ_1, becomes equal to $\omega^2 E_0 (d\mu)^2$. All the counters in computational cells between these collisions increase by ωE_0. After the next collision the counters will increase by $\omega^2 E_0 d\mu$, and at $d\mu \to 0$ we can neglect this increase. Due to this fact, we shall trace the photon with energy $E d\mu$ only until the first collision occurs. At the same time we shall trace the photon with the energy $E(1 - d\mu)$ (moving in the direction μ_2) by a common algorithm. This photon won't affect the counter directly, but will create new photons with energy $E(1 - d\mu) d\mu \approx E d\mu$ after each collision. The radiation intensity corresponding to the value of the counter E_Σ in the given cell is $J = E_\Sigma / 4\pi\mu_1$.

It should be stressed that if we want to find radiation intensity only on the layer border, we don't need to determine the free path of the photon with the energy $E d\mu$. Instead, we can just multiply this energy by $e^{-(\tau_H - \tau)/\mu_1}$.

Let's estimate the ratio of the performance of the probabilistic algorithm t_1 to the performance of the regular Monte Carlo algorithm (at the statistical error ε fixed). It is obvious that

$$t_2 / t_1 \sim N_2 / N_1 , \tag{21}$$

where N_1 and N_2 are the numbers of the photons required by the probabilistic and the common methods correspondingly to reach the error ε. This error can be given by

$$\varepsilon = c / \sqrt{n} , \tag{22}$$

where n is the number of the photons which have made the contribution to our statistics, and c is a constant, almost identical for both algorithms at small $d\mu$. For the probabilistic method $n_1 = N_1$, and for the common algorithm $n_2 = N_2 d\mu \cdot f(\mu)$, where $f(\mu)$ is a factor with the meaning of about 1. Having assumed $f(\mu) \approx 1$, from (21) we shall have

$$t_2 / t_1 \sim 1 / d\mu . \tag{23}$$

In tree-dimensional case we shall have (24) instead of (23):

$$t_2 / t_1 \sim 1 / d\mu d\varphi . \tag{24}$$

To compare regular algorithm with the local estimation algorithm a special test case was considered [34]. The specified test case has been offered in work [30]. The radiating cylinder is filled with a homogeneous high-temperature mixture of gases H_2O, CO_2, CO at temperature $T = 2000\,\mathrm{K}$ and with particles Al_2O_3 with an average radius of 2 microns. The radius of the cylinder is taken equal to 10 cm, and its height to 600 cm. For calculations of spectral optical properties the optical model [35–39] of the molecular lines averaged on rotary structure was used.

Figure 5.1 shows the spectral radiation signature of the cylinder without scattering at the observation angle of 90 degrees. Calculations were performed using two imitating algorithms.

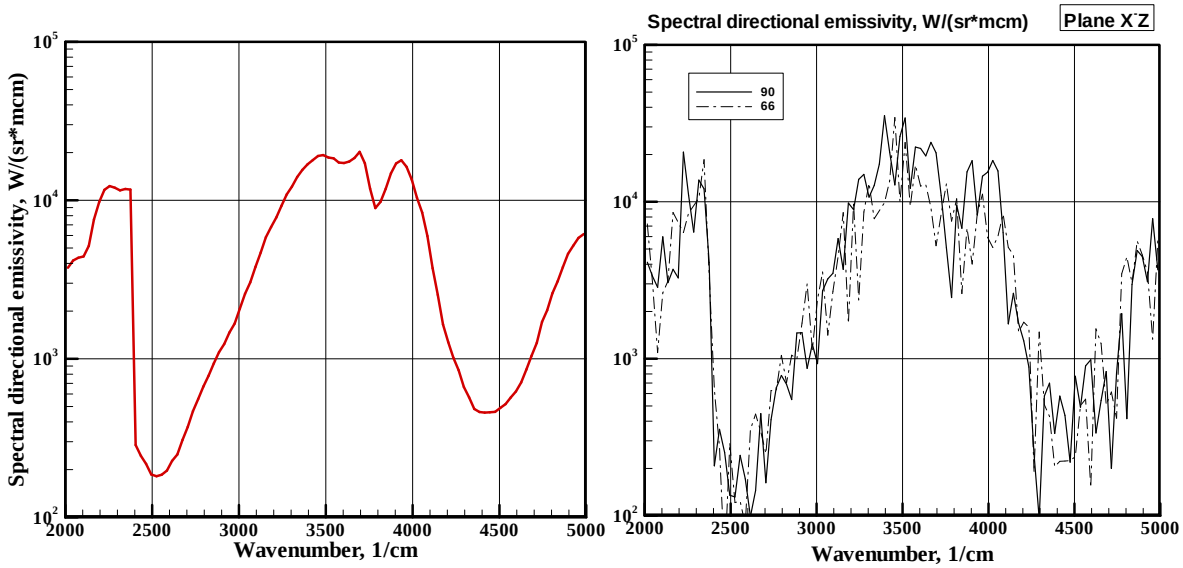

Figure 5.1: Spectral signatures predicted by two different Monte-Carlo algorithms. No scattering. Results obtained by the regular Monte-Carlo algorithm are presented for the two angles of observation

One of them the Monte-Carlo local estimation of directional emissivity algorithm and another one is the regular Monte-Carlo imitative algorithm [26,28]. The method of the local estimation of emissivity has shown high efficiency. This method reaches 5% accuracy of statistical modeling approximately 100 times faster.

Figures 5.2 show spectral directional emissivity at solid particle concentration 10^7 cm^{-3}. In this case, histories of 10^4 photons were simulated. One can see advantage of the local estimation method for the problem under consideration. Details of these calculations are presented in [34].

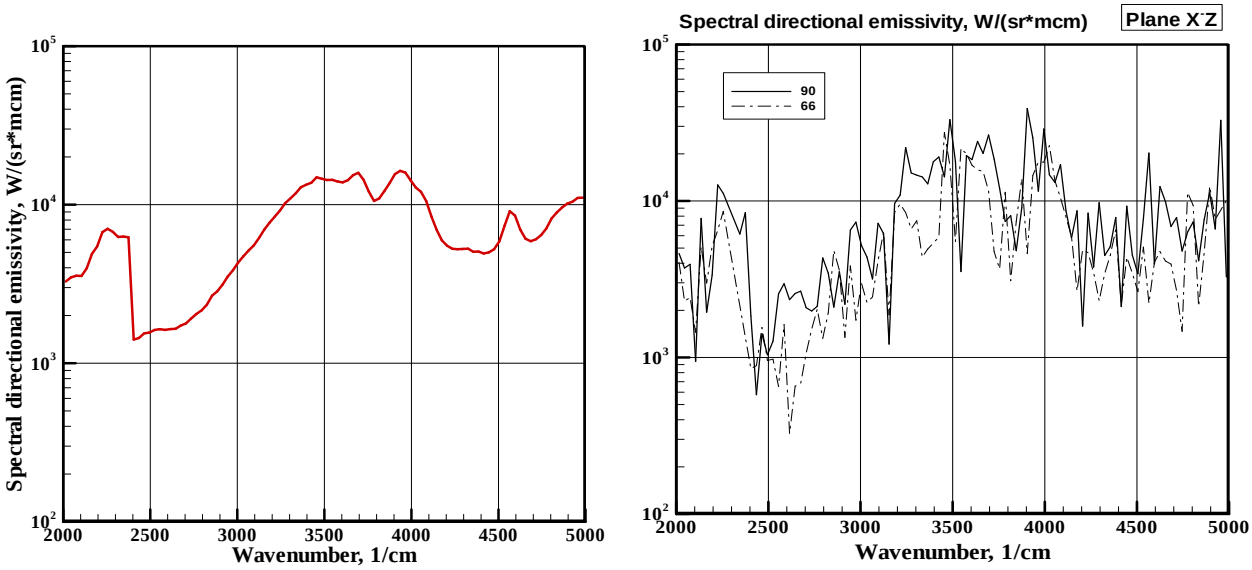

Figure 5.2: Spectral signatures of light-scattering volume predicted by two different Monte-Carlo algorithms at number of photon histories 10^4. Results obtained by the regular Monte-Carlo algorithm are presented for the two angles of observation

6.0 EXAMPLES OF APPLICATION OF METHODS FOR SOLVING RADIATION HEAT TRANSFER EQUATIONS

6.1 P_1-approximation [4]

The radiation heat transfer problem was considered for two-dimensional axially-symmetric geometry to analyze typical solutions of the P_1-equations. Temperature distribution in such a volume is shown in Figure 6.1. Note that such a spherically symmetric radiating region, localized in space, allows test wide class of methods developed in the radiation heat transfer theory.

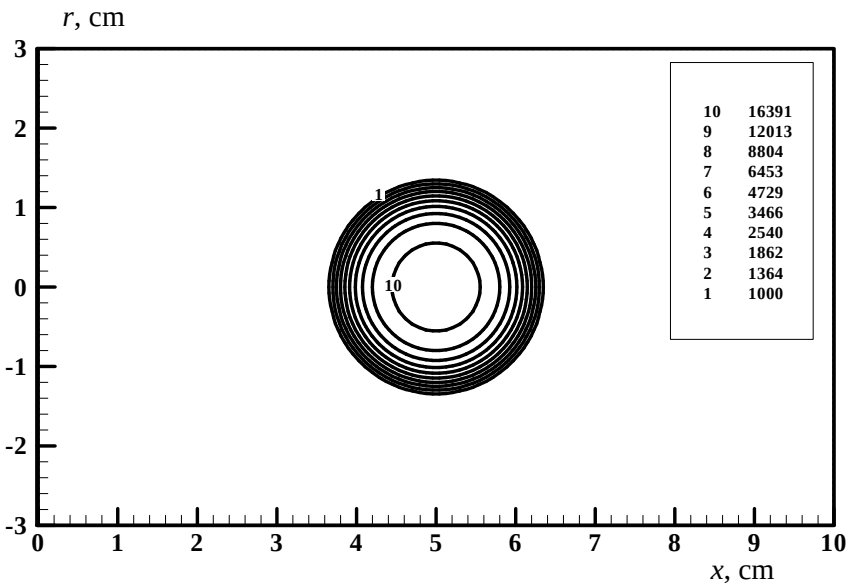

Figure 6.1: Temperature inside two-dimensional cylindrical volume

Temperature field shown in Figure 6.1 was calculated by

$$T(x,r) = T_{\min} + (T_{\max} - T_{\min}) \exp\left(-\frac{R^m}{R_0}\right),$$

where

$$T_{\min} = 300\,\text{K}, \quad T_{\max} = 18000\,\text{K}, \quad m = 4,$$

$$R = \sqrt{(x - x_0)^2 + (r - r_0)^2},$$

$$x_0 = 5\,\text{cm}, \; r_0 = 0, \; R_0 = 1\,\text{cm}.$$

Functions of radiation field corresponded to this temperature distribution and $\kappa = 0.1\,\text{cm}^{-1}$ obtained by the P_1-approximation (see Equation (3.40)) are shown in Figures 6.2–6.5.

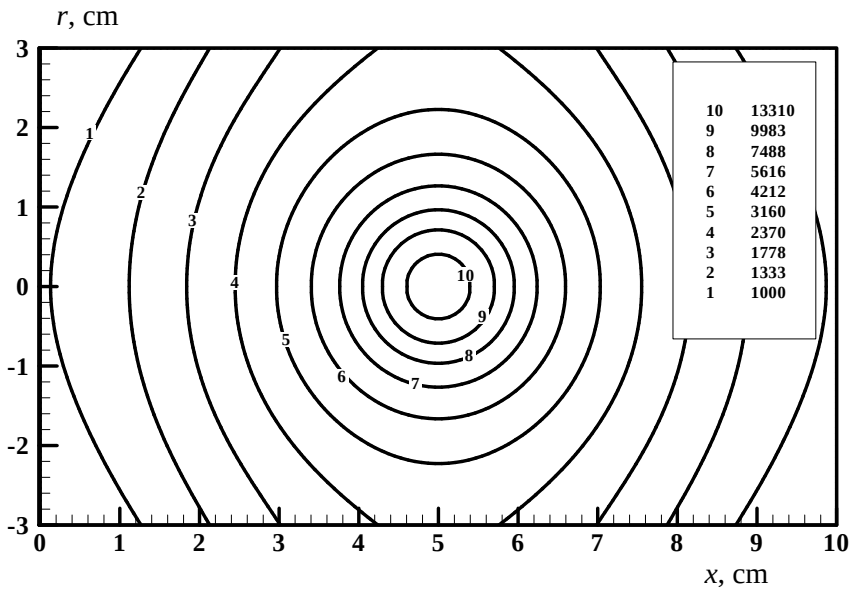

Figure 6.2: Volume density of radiation, J/cm3; $\kappa = 0.1 cm^{-1}$

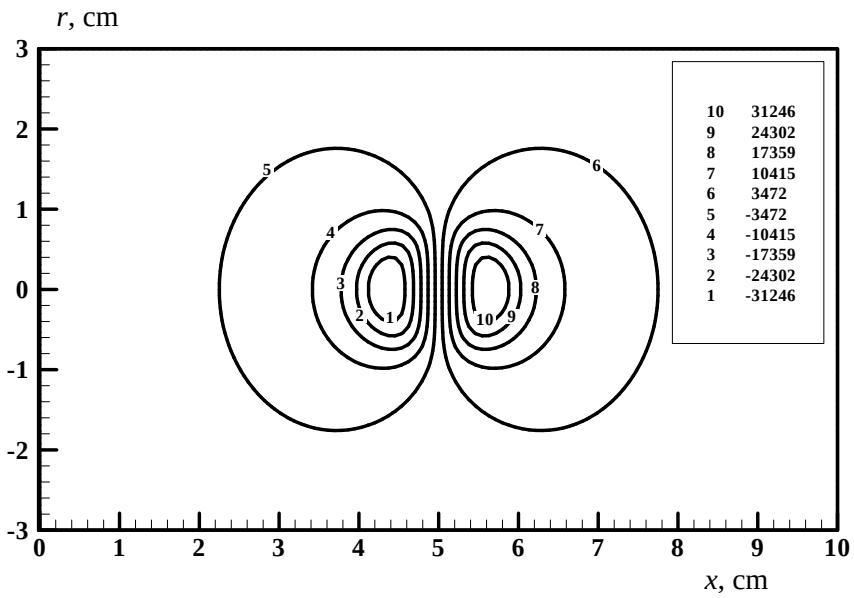

Figure 6.3: Radiation flux W_x , W/cm2; $\kappa = 0.1 cm^{-1}$

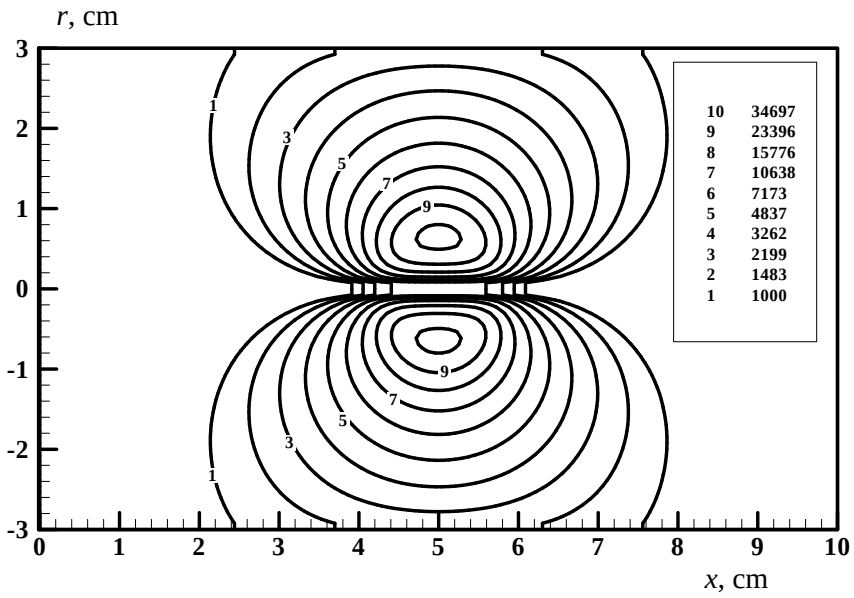

Figure 6.4: Radiation flux W_r , W/cm^2; $\kappa = 0.1\,\text{cm}^{-1}$

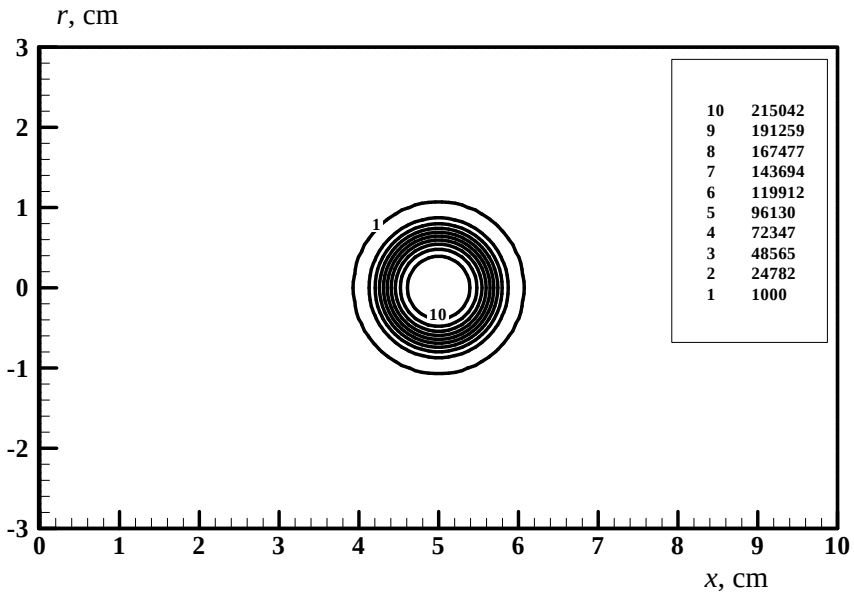

Figure 6.5: Divergency of radiation flux $Q_r = \text{div}\,\vec{W}$, W/cm^2; $\kappa = 0.1\,\text{cm}^{-1}$

Finite-difference grid used at these calculations is shown in Figure 6.6. Calculated data presented here may be used at verification of other methods and codes of radiation heat transfer theory.

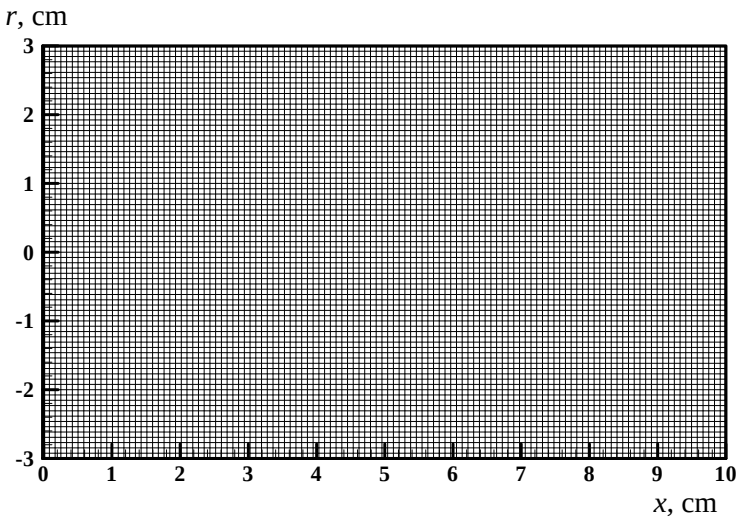

Figure 6.6: Finite different grid

6.2 The quadro-moment method [40]

The quadro-moment method was applied to integration of two-dimensional radiation heat transfer problem similar to those considered in the previous section. Temperature distribution with the centre located at the symmetry axis of cylindrical volume was calculated as follows (Figure 6.7):

$$T(x,r) = T_0 + T_1 \cdot \exp\left[\left(\frac{r}{b_r}\right)^2 + \left(\frac{x - x_c}{b_x}\right)^2\right],$$

where $T_0 = 300\,\mathrm{K}$, $T_1 = 10000\,\mathrm{K}$; x_c is the axial coordinate of the high temperature area centre, b_r, b_x are the shape form parameters of the temperature distribution along axes *r* and *x*.

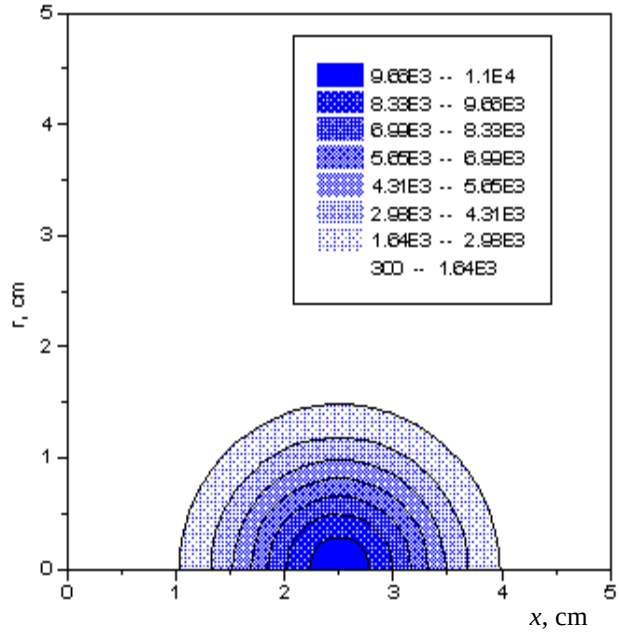

Figure 6.7: Temperature distribution

The radius and height of the cylinder were entered as 5 cm. These calculations were performed with the P_1 approximation of the spherical harmonics method and with the zeroth-order approximation of the quadro-moment method. Different calculation grids, absorption coefficients k and coefficients defining the value of artificial calculation diffusion ε were used. At all figures representing the isometric lines of divergence of the radiant flux integral at $0.5 \div 0.6$ μm, the figures at the curves denote the values of Q in W/cm^3. Symbol (+) here means emission of radiation, while the symbol (–) means absorption.

Comparison of calculated data presented in Figure 6.8. It is clear from this figure and it was shown [40] that the zero approximation of the quadromoment method allows obtain results close to those obtained with the P_1-approximation of the spherical harmonics. But it should be taken into account that the quadro-moment method has some advantages as compared to P_1-approximation at the use of the methods with multi-group spectral method.

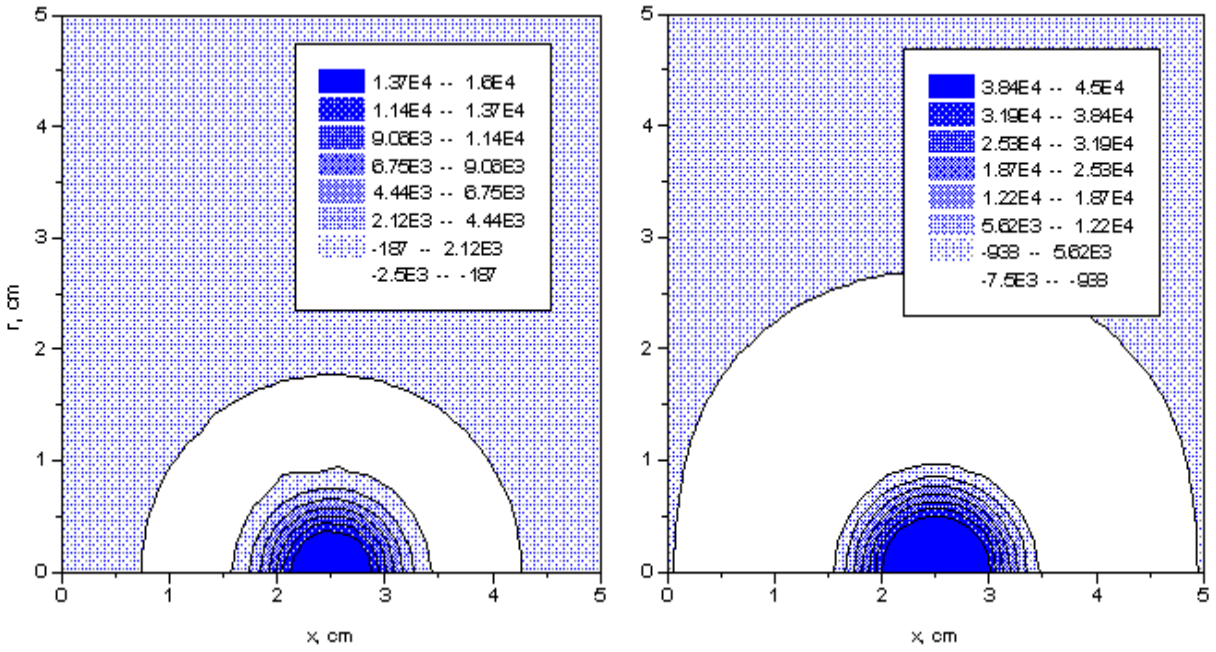

Figure 6.8: Radiation flux divergence: P_1-method (left), the quadro-moment method (right); $\kappa = 0.1\,\text{cm}^{-1}$

6.3 The ray-tracing method

6.3.1 Radiative heating of internal surface of the laser plasma generator [41,42]

Radiation heat transfer was considered in working zone of laser plasma generator (LSPG). Calculations were performed for the following input data: the capacity of the CW CO_2-laser is $P_L = 200$ kW, the focal length of the focusing lens is $f = 3$ cm, the divergence of the laser radiation is $\theta = 0.1$ mradian, the initial radius of the laser beam is $R_b = 1.0$ cm, the pressure in the LSPG channel is $p_0 = 1$ atm, the gas velocities in the input section is $u_0 = 30$ m/s, the length and radius of the LSPG channel are $L_c = 11$ cm and $R_c = 1.3$ cm. Calculation domain was covered by inhomogeneous calculation grid $NJ = 120$, $NI = 40$ (NJ is the number of calculation grid nodes along x-axis; NI is the number of nodes along r-axis).

Temperature profile is shown in Figure 6.9 for laminar gas flows in LSPG [42].

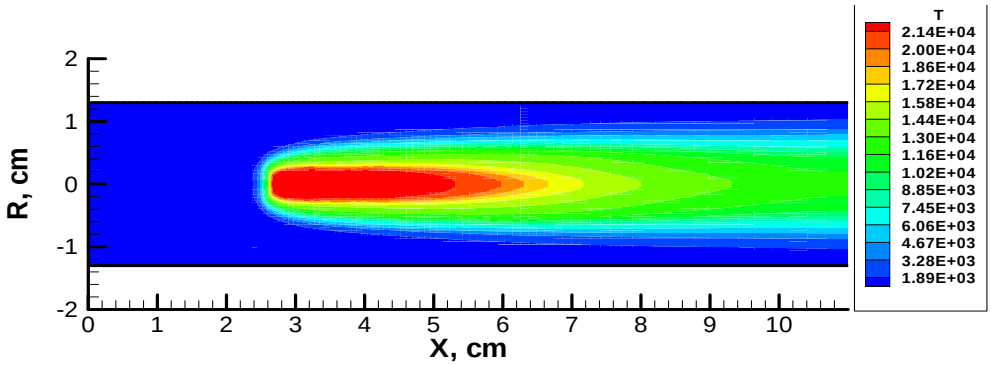

Figure 6.9: Temperature distribution (in K) at entrance velocity $u_0 = 30$ m/s and $P_L = 200$ kW in air LSPG; the laminar gas flow

Integral radiation flux presented in Figure 6.10 calculated for 148-group spectral model. The ray-tracing method was used for prediction of the group spectral fluxes on the internal surface. Example of such calculations is presented in Figure 6.11, where the 148-group radiation fluxes are presented for the five points on the LSPG internal surface. Numbers of presented points correspond to the following coordinates along internal surface: 1 – $x = 0.46$ cm, 2 – $x = 0.93$ cm, 3 – $x = 1.79$ cm, 6 – $x = 4.1$ cm, 11 – $x = 10.8$ cm.

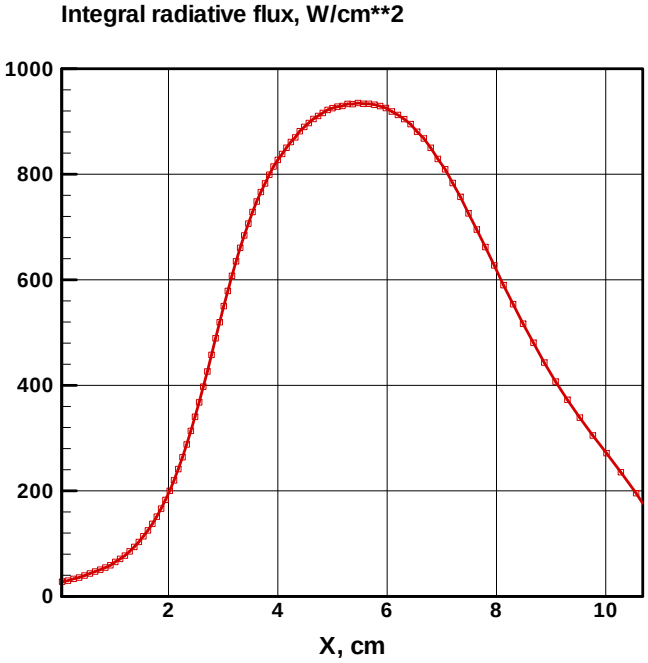

Figure 6.10: Integral radiation heat flux along internal cylindrical surface of hydrogen LSPG, W/cm^2. The ray-tracing method. Number of angular points 41. Number of spectral groups 148

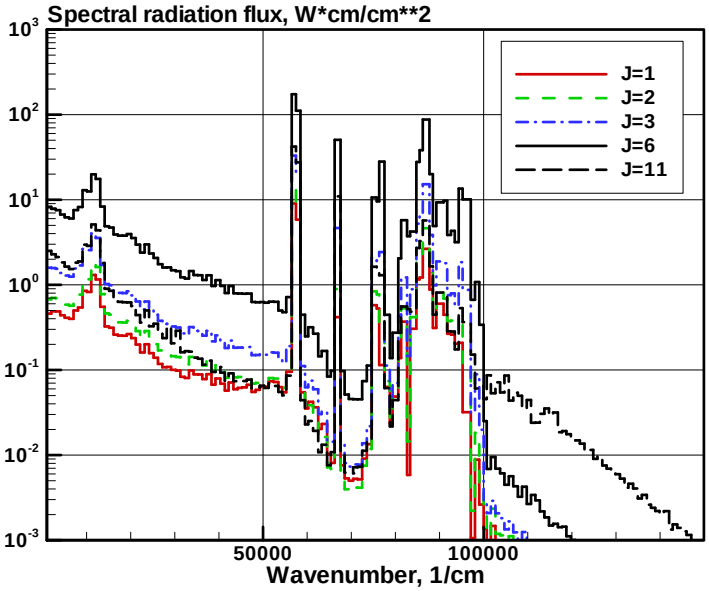

Figure 6.11: Group radiation heat fluxes at different points of internal surface of air LSPG, W/cm^2. The Ray-tracing method. Number of angular points 41. Number of spectral groups 148

6.3.2 Radiative heating of space vehicle surface [43,44]

Computational code NERAT-2D was used for prediction of radiative heating of whole surface and spectral signature of space vehicles, entering into planet atmospheres. The models which are realized in the computational code NERAT-2D include description of general physical-chemical processes which can be significant for solving problem under consideration, namely: the complicated gasdynamic structure appearing at streamline of space vehicles of complex geometry is described by the Navier – Stokes equations for viscous heat conducting gas; the non-equilibrium physical and chemical kinetics of gas behind shock wave and in wake are described by the equations of energy conservations for different internal degrees of freedom and by the species mass conservation equations; the spectral radiation transfer in whole disturbed area is described by the P_1-approximation and by the ray-tracing method.

Prediction of the radiation heating of MSRO surface was performed in [43,44] for four trajectory points, and for two assumptions concerning the space vehicle wall catalicity effects. In the first case the surface was presumed as non-catalytic, and the pseudo-catalytic surface with 97% CO_2 and 3% N_2 at the wall was presumed for the second case.

Examples of numerical simulation results are presented in Figures 6.12–6.14. These calculation data correspond to the following trajectory point in Martian atmosphere (see Table 6.1 and [43,44]): $\rho_\infty = 3.07\times10^{-7}$ g/cm^3, $p_\infty = 82.3$ erg/cm^3, $V_\infty = 3998$ m/s. Total radiation flux on MSRO surface is shown in Figure 6.13. Figure 6.13 shows also the spectral radiation fluxes at five points on the surface. Location of marked points one can determine by Figure 6.14. Also radial and axial coordinates of marked points (in cm) are shown on the field of each figure. Legends for the figures showing total and spectral radiation fluxes contain also the following data: N_g is the number of spectral groups; N_m is the number of points along each ray emitting from MSRO point; N_θ is the minimal number of rays emitting in the θ-angle direction (θ is the angle of latitude in local coordinate system connected with an elemental area on MSRO surface); N_φ is the minimal number of rays emitting in the φ-angle direction (φ is the azimuth angle in local coordinate system). It should be noted that a special numerical study was performed for substantiation of the chosen numbers of angle directions.

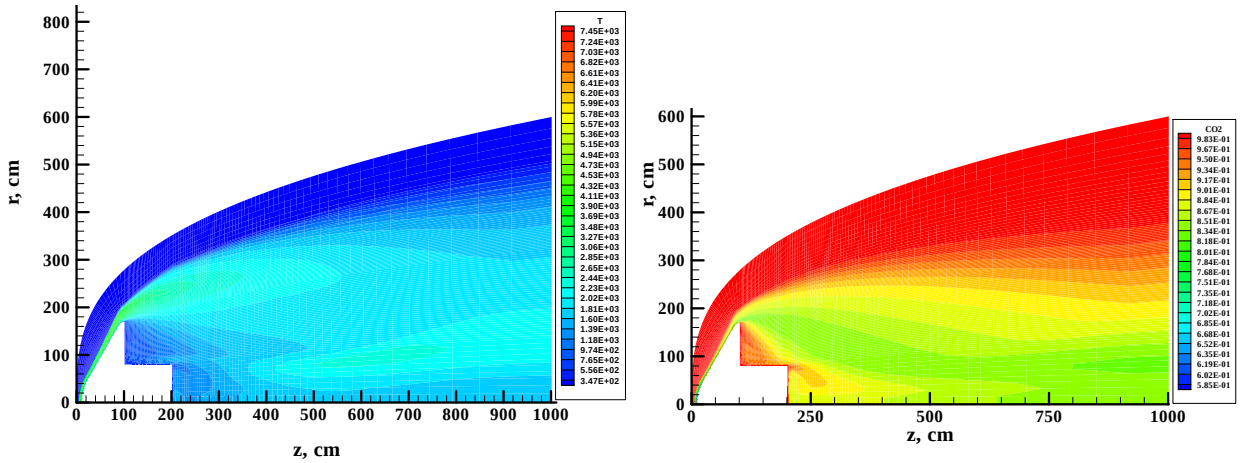

Figure 6.12: Temperature distribution (left) and mass fraction of CO_2 (right). Trajectory point No.3. Pseudo-catalytic surface

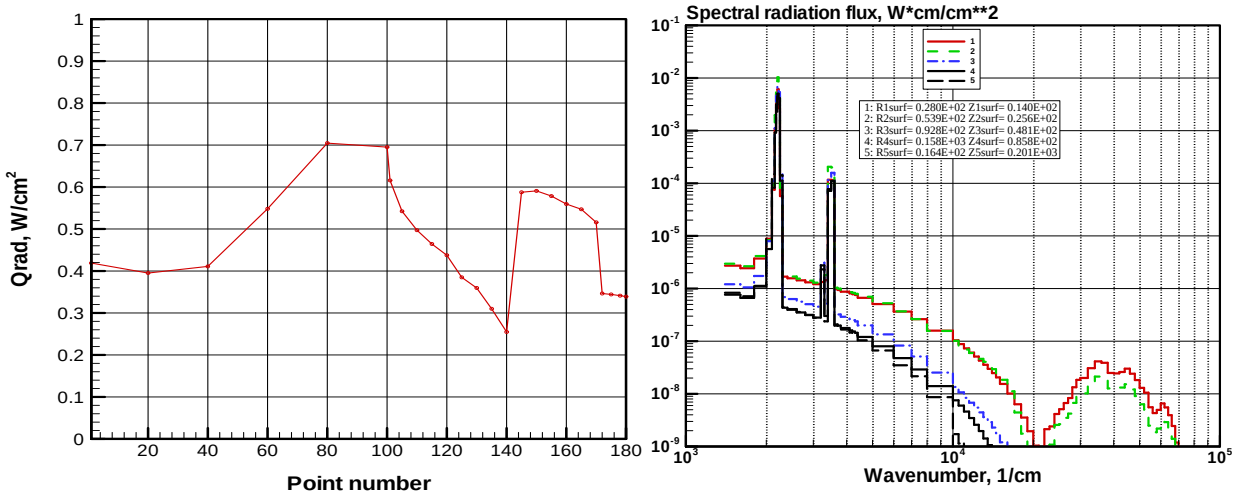

Figure 6.13: Total radiation flux on the MSRO surface (left) and the spectral radiation fluxes at some points on the MSRO surface. Trajectory point No.3. Pseudo-catalytic surface. $N_g = 91$, $N_m = 100$, $N_\theta = 11$, $N_\varphi = 11$

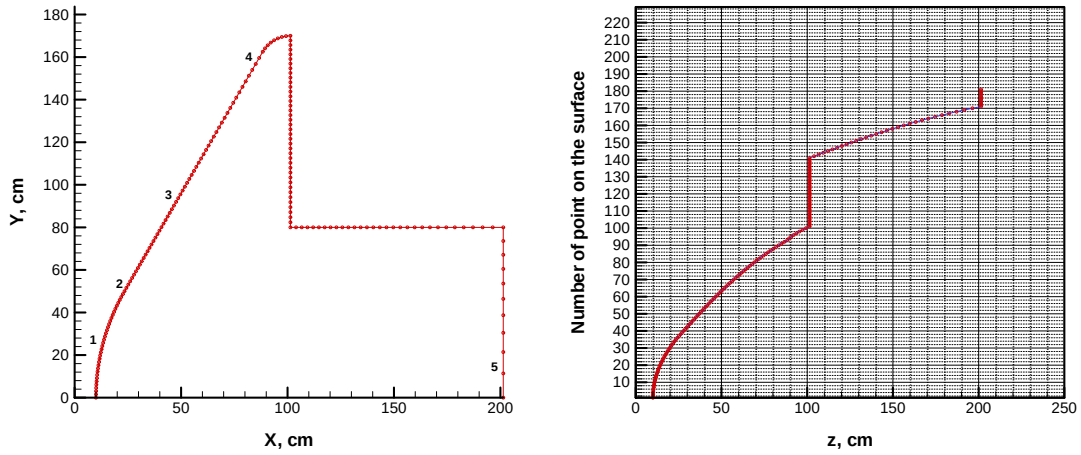

Figure 6.14: Location of marked points on the MSRO surface, and correspondence of point numbers to axial coordinates on the MSRO surface

6.3.3 Spectral signatures of space vehicle MSRO [45]

Spectral signatures of heated gas behind shock wave and from wake at MSRO entering into Martian atmosphere were calculated for two angles of observation (see schematic of the problem in Fig. 6.15), $\theta = 30°$ and $90°$. Calculations were performed for four trajectory points. The ray-tracing method was used in the case.

Table 6.1: MSRO trajectory points

No. of trajectory point	Time, s	ρ_∞, g/cm^3	p_∞, erg/cm^3	V_∞, m/s	T_∞, K
1	70	3.14×10^{-8}	8.4	5687	140
2	115	2.93×10^{-7}	78.7	5223	140
3	175	3.07×10^{-7}	82.3	3998	140
4	270	2.82×10^{-8}	7.6	3536	140

Presented data allow confirm well known fact that that most intensive radiation in spectral signature is located in the UV spectral region for high-velocity trajectory points (Figure 6.16, a) and in the infrared spectral region for relatively low-velocity trajectory points (Figure 6.16, d). Infrared radiation generally connected, as before, with vibrational bands of CO_2 and CO.

It should be noted that ablation of heat shields of lander may make a significant contribution to the radiation of the shock layer and especially of a wake. There are two consequences from this fact. First of all, the model must include detailed description of the thermo chemical processes on a streamlined surface and predict chemical composition and mass of products of heat protection material thermo chemical destruction. Secondly, this fact can be used for increase of the spectral signature at any given spectral region by including special luminous elements as admixture of heat protection material.

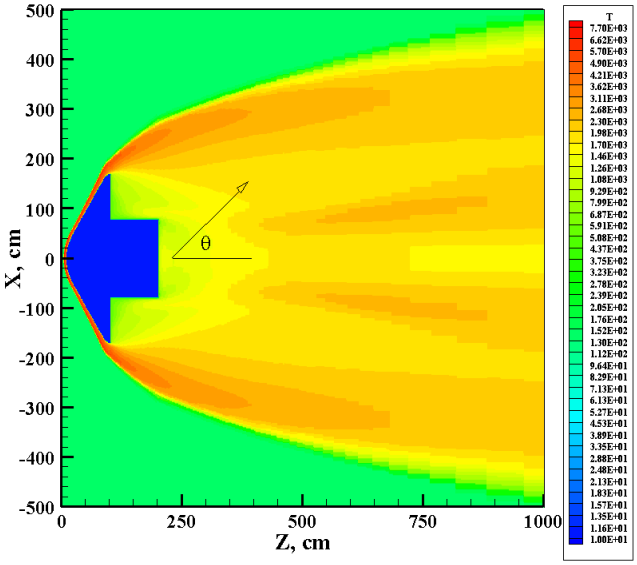

Figure 6.15: Temperature field for trajectory point No.1

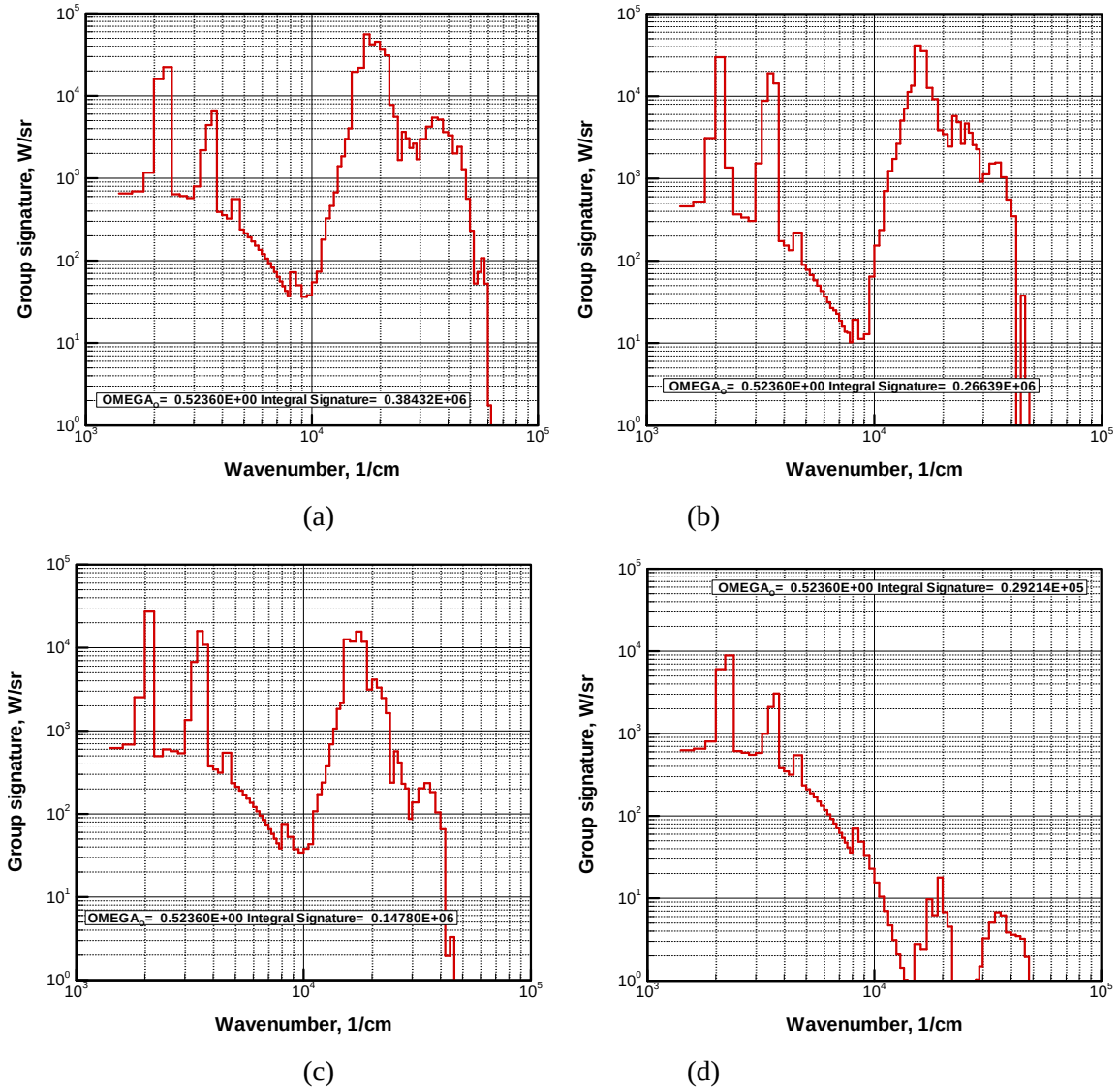

Figure 6.16: Wavenumber dependence of total-in-groups signature predicted for $\theta = 30°$. Trajectory points No.1 (a),2 (b),3 (c),4 (d). The pseudo-catalytic surface.

6.4 Discrete ordinates method [16]

Discreet ordinates method, described in Section 3.4, was used for after body radiative heating prediction for MSRO space vehicle. It was assumed that Martian atmosphere contents 97% CO_2 and 3% N_2. The optical region was chosen as $1970 \div 4000$ cm^{-1}. The temperature distribution (Figure 6.17) and mass fraction behind space vehicle were taken from [43, 46]. Surface of the MSRO was assumed absolutely black at the temperature 500 K. To define group absorption coefficients the ASTEROID code was used [1, 47]. For verification of the radiation heat flux prediction the NASA standard infrared radiation model [35] was also used. Coordinates of the cylindrical cell are defined by two spatial coordinates r, h and one angular coordinate θ. Spatial mesh for $\theta = 0$ is shown in Figure 6.18. The tetrahedral grid was generated by subdividing cylindrical cells into tetrahedrons. Integral radiation heat fluxes along afterbody surface of the MSRO depending on order of used quadrature (SN) and on number of spectral groups (GR) are shown in Figures 6.19 and 6.20. Analysis of these and others numerical simulation results shows that developed

in [16] version of the discreet ordinates method allows predict radiative heating of space vehicle surface with good accuracy.

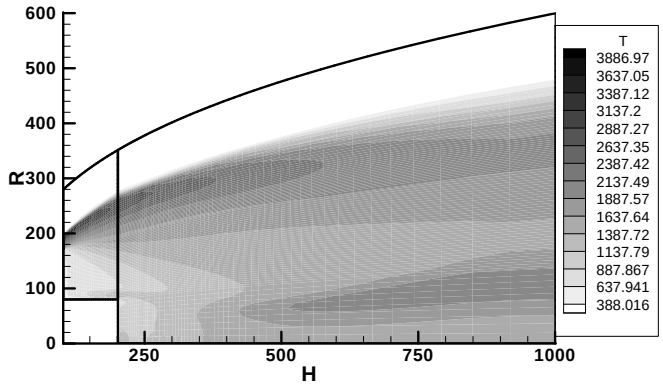

Figure 6.17: Temperature distribution behind the MSRO

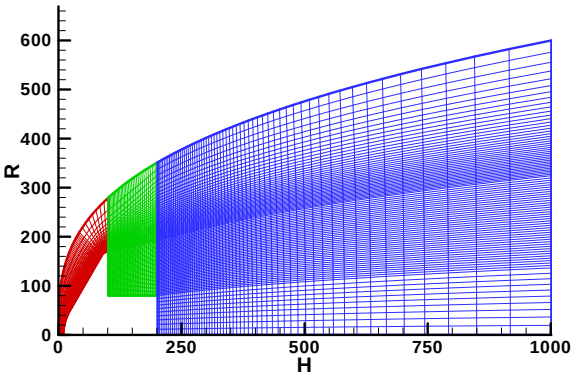

Figure 6.18: Computational grid

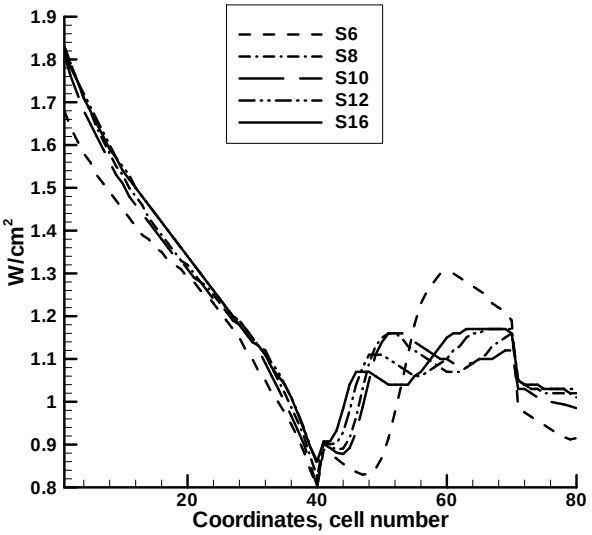

Figure 6.19: Integral radiation heat flux depending on order of used quadrature, for 10 spectral groups and NK=30

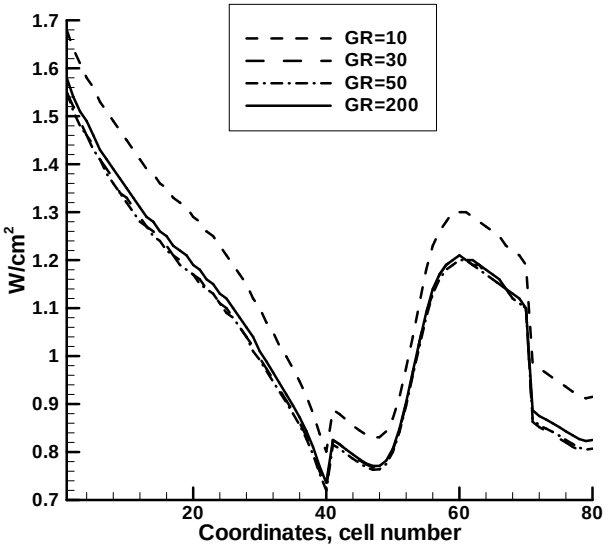

Figure 6.20: Integral radiation heat flux depending on number of spectral groups for S6 approximation and NK=30

6.5 Random models of atomic lines [48]

Radiation heat transfer behind shock waves in air is considered. The problem is solved in one dimensional (1D) approach for temperature profile behind the shock wave fronts which is shown in Figures 6.21, a at atmospheric pressure. Corresponding distributions of the molar fractions of high temperature air are shown in Figure 6.21, d. The radiation heat transfer equation was integrated with the line-by-line method and with the random model, described in Section 4.1.

For the analysis two spectral ranges $\Delta\omega_2, \Delta\omega_{16}$ were chosen (see Table in the Figure 6.22). The range $\Delta\omega_2$ contains about 100 lines of atoms N, O, formed at transitions from exited energy states. In the each spectral point of this range the optical thickness is appreciably less than unit. The second spectral range $\Delta\omega_{16}$ is characterized by the following attributes: the spectral range contains atomic and ionic lines, formed at transitions from ground and lower states; the optical thickness in centers of the strongest lines surpasses unit.

The typical distributions of integrated radiation fluxes and them divergency are shown in Figures 6.21,b,c. Areas of positive flux divergency correspond primary to emission of radiation, and negative ones corresponds to absorption. The observable absorption of radiation in the ultra violet part of the spectrum is caused generally by the photoionization and photodissociation, and also by some electronic bands of diatomic molecules.

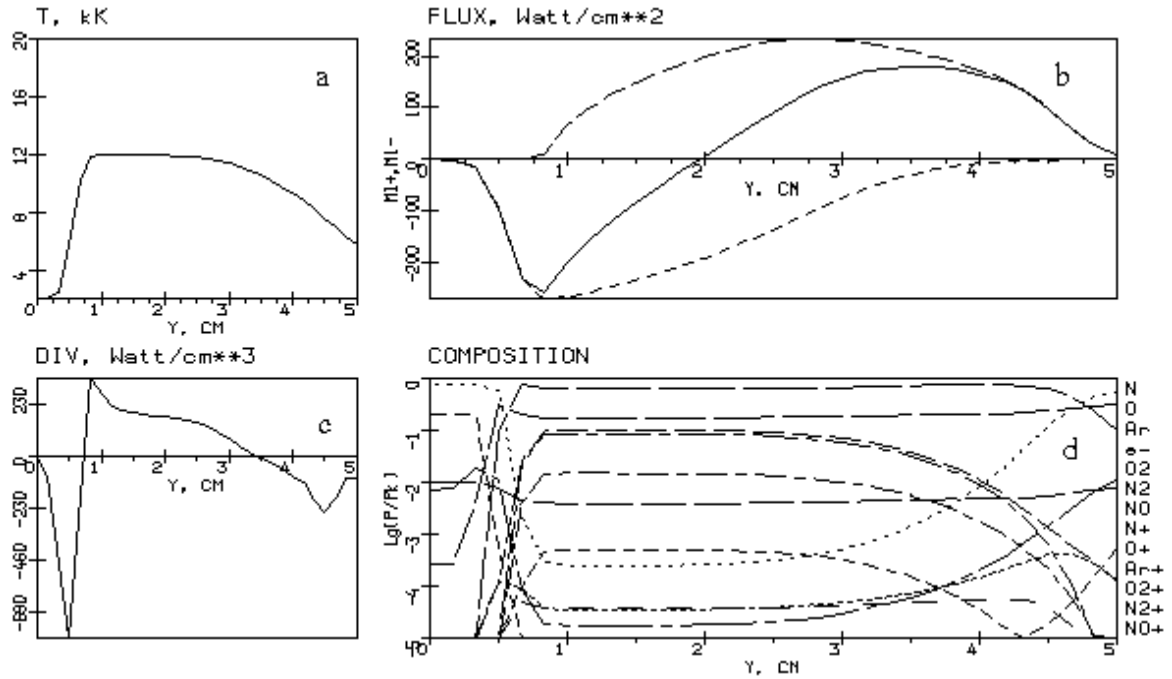

Figure 6.21: Distribution of temperature and total radiation characteristics behind shock wave with T_{max} = 12000 K: a) temperature, b) one-side (upper and lower dashed curves), and full radiative fluxes, c) divergence of the total flux, d) species molar fraction

Let us consider radiative characteristics in two points behind the shock wave front with coordinates $x_1 = 0.5$ and $x_2 = 3.7$ cm. In the first of the two points the spectral and integrated fluxes $M_1^-(x_1)$ give representation about radiation of the layer on the left its part. Coordinate x_2 corresponds to right boundary of high-temperature part of the shock wave. The values of spectral and total fluxes in the point x_1 are of interest for the purposes of the analysis of photochemical processes in the cold air. The values of radiation fluxes in the point x_2 are of interest for the analysis of processes in low-temperature regions of the shock wave.

The distributions of spectral radiation fluxes in the points x_1 and x_2 are shown in Figure 6.22. On can observe some spectral regions, in which the leaving radiation is close to radiation of the absolutely black body.

Figures 6.23 and 6.24 show spectral absorption coefficients in the points x_1 and x_2, and also spectral radiating fluxes, obtained at line-by-line calculations in the regions $\Delta\omega_2$ and $\Delta\omega_{16}$. It is seen that the atomic lines spectra in these regions differ by location, intensities and half-widths.

The spectral radiating fluxes $M_1^-(x_1)$ and $M_1^+(x_2)$ in the range $\Delta\omega_2$ are rather close. It can be explained by small optical thickness in all its spectral points. In a vicinity of the strongest lines in spectral range $\Delta\omega_{16}$ the leaving radiation $M_1^-(x_1)$ almost reaches radiation of the black body. Presence of the same

lines (low-broadening in low-temperature part of the plasma layer) results in strong absorption of the spectral radiation.

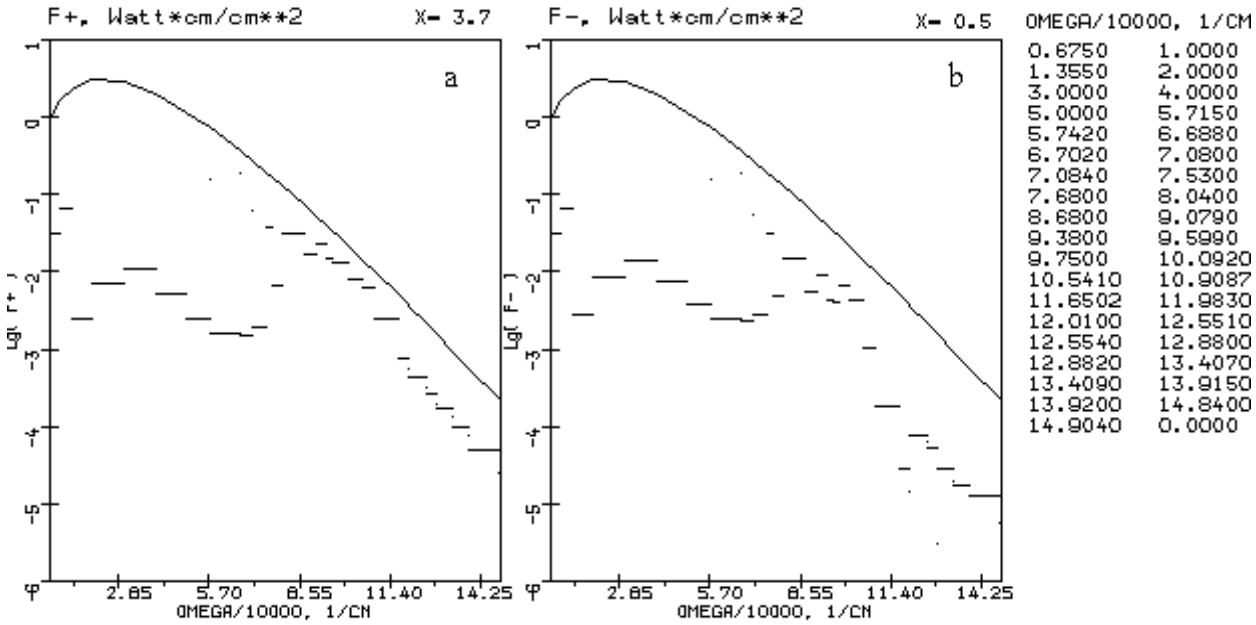

Figure 6.22: Spectral distribution of the positive radiation flux $\tilde{M}^{+}_{1,\omega}$ at the point $x = 3.7$ cm, and spectral distribution of negative radiation flux $\tilde{M}^{-}_{1,\omega}$ at point $x = 0.5$ cm; solid curves: the Planck function. $T_{max} = 12000$ K

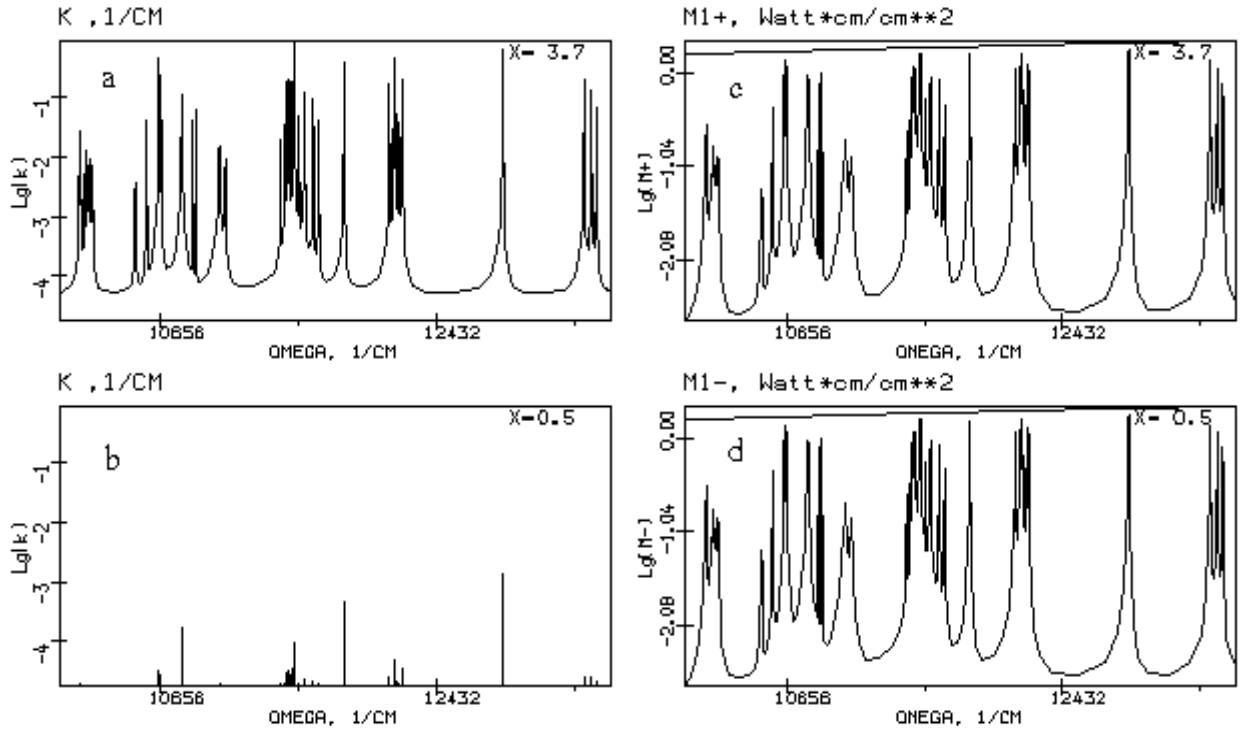

Figure 6.23: Spectral absorption coefficient in the region $\Delta\omega_2 = 10000 \div 13550$ cm^{-1} at the point $x = 3.7$ cm (a) and at the point $x = 0.5$ cm (c); spectral radiation flux in the region $\Delta\omega_2 = 10000 \div 13550$ cm^{-1} at the point $x = 3.7$ cm (b) and at the point $x = 0.5$ cm (d). $T_{max} = 12000$ K

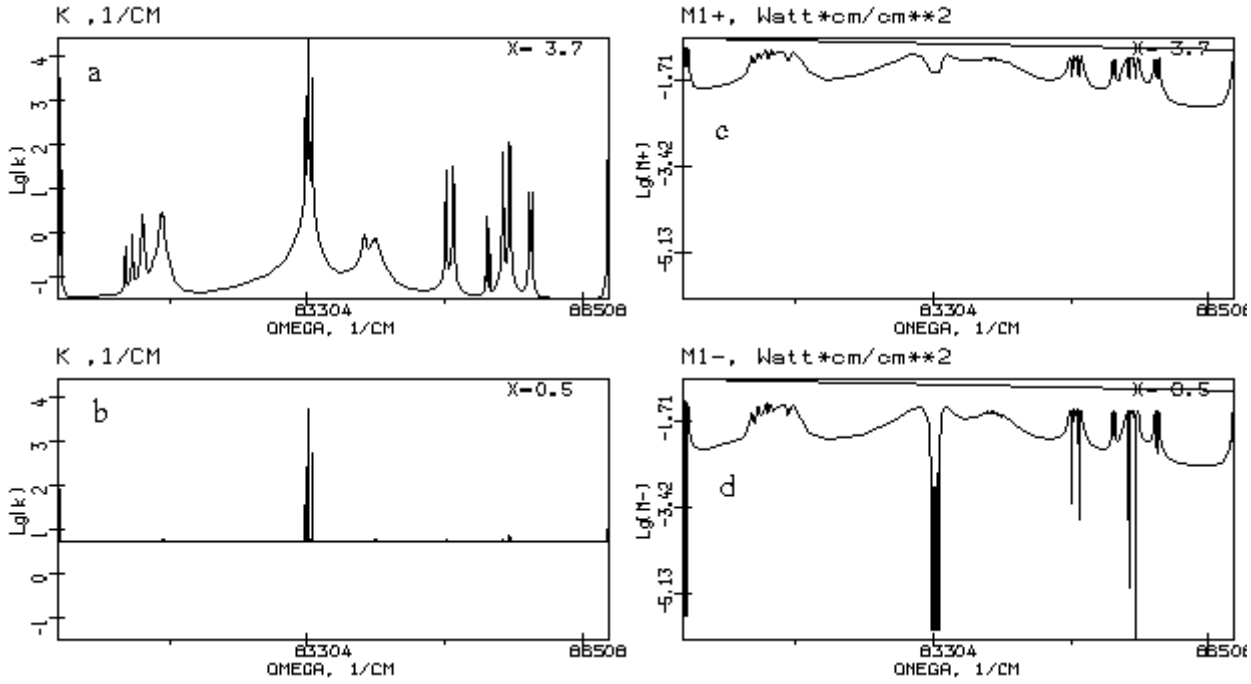

Figure 6.24: Spectral absorption coefficient in the region $\Delta\omega_{16} = 80400 \div 86800$ cm^{-1} at the point $x = 3.4$ cm (a) and at the point x=0.5 cm (c); spectral radiation flux in the region $\Delta\omega_{16} = 80400 - 86800$ cm^{-1} at the point $x = 3.4$ cm (b) and at the point x=0.5 cm (d). $T_{max} = 12000$ K

To give general representation about influence of atomic and ionic lines on heat radiative transfer in plasma layers the distributions of total radiation fluxes inside the layer are presented in Figure 6.25. In spite of the fact that in separate spectral ranges atomic and ionic lines give increase of radiation fluxes more than on the order, total radiation grows not more than in two-three times. Atomic and ionic lines exert largest influence on the radiative fluxes in the infra-red area of the spectrum, where the optical thickness of the layer is small. In the ultra-violet part of the spectrum the influence of separate groups of strong lines is not very great. Either the share of these sites in integrated radiation is small, or the investigated plasma layers here have optical thickness appreciably larger than unit and integrated fluxes poorly differ from flows of an absolutely black body.

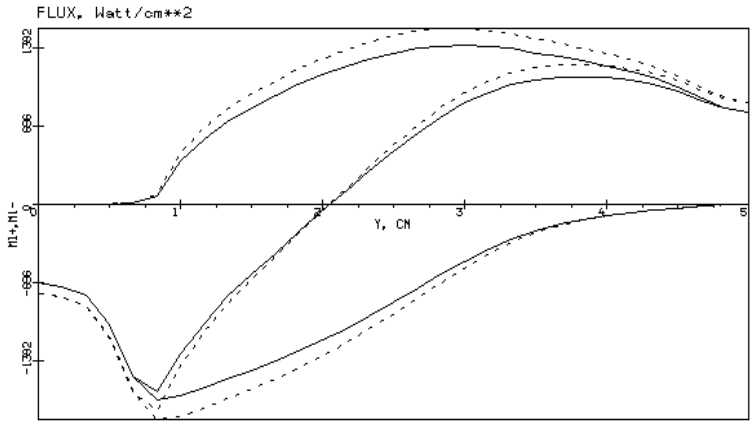

a

Figure 6.25: (beginning)

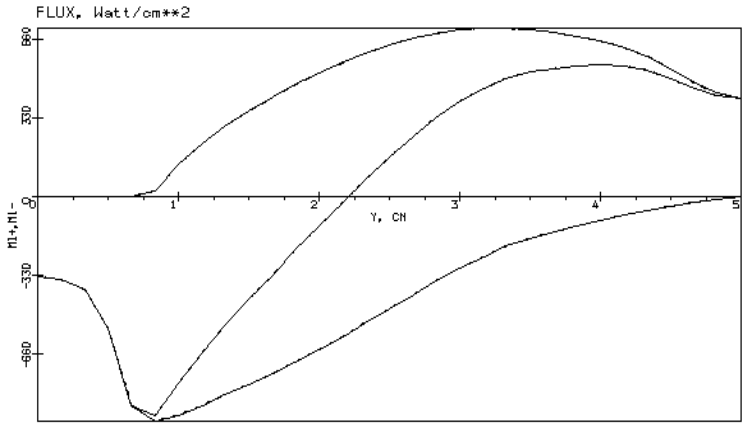

b

Figure 6.25: Distributions of the one-side (upper and lower curves), and total radiation fluxes in the plane layer with T_{max} = 12000 K: a) atomic lines are taken into account; solid curve – line-by-line calculation, dashed curve – group-random model; b) without atomic lines

Let us now consider results of estimations of radiation heat fluxes obtained with the use of group-random model. At preparation of group functions of the atomic lines parameters the following principles of the grouping were used: 1) inside given group there are the lines only one species; 2) the lines are grouped on sizes of constants C_4 (see Section 4.2): $C_4 = 0.001–0.01$ for the first group, $C_4 = 0.01–0.1$ for the second group, $C_4 = 0.1–1.0$ for the third group, $C_4 = 1.0–10$ for the fourth group.

The mathematical expectation of the oscillatory strength and half-width of lines inside each group were calculated as the average arithmetic of their sizes. An exponential low was used for probability densities of oscillator strengths, and the delta-function was used for probability densities of half-width of the atomic lines.

The relative discrepancy between the line-by-line and random numerical simulation results are calculated as follows:

$$\varepsilon = \frac{M^{\pm}_{0,1,rm} - M^{\pm}_{0,1,ls}}{M^{\pm}_{0,1,ls}} 100\%,$$

where $M^{\pm}_{0,1,ls}, M^{\pm}_{0,1,rm}$ are the radiation fluxes, obtained at the line-by-line integration and by the group-random model. Comparison of the radiation fluxes with and without atomic lines, as well as the radiation fluxes obtained by the line-by-line and the random model are shown in Figure 6.25. It is possible to conclude that the use of the group-random model allows predict total radiation fluxes with accuracy not worse than ~30 %. It should be emphasized, that by use of simple statistical model (at association of all lines in the one group on C_4) these errors can reach ~ 200 %. Comparison of the radiation fluxes with and without atomic lines shows significant influence of the atomic lines in the case under consideration.

6.6 Macro-random model [20, 21]

The macro-random model of vibrational bands of molecules H_2O and CO_2 was applied for calculation of radiative characteristics in parallel-plane inhomogeneous layers. Schematic of the problem of radiation heat transfer is shown in Figure 6.26. Temperature and molar fractions of gas species distributions (CO_2, H_2O) was set in the following form:

$$T(x) = T_0 + (T_{\max} - T_0)\exp\left[-\left|\frac{x - x_c}{d_x}\right|^n\right], \tag{57}$$

$$c_k(x) = c_{k,0} + (c_{\max} - c_{k,0})\exp\left[-\left|\frac{x - x_c}{d_x}\right|^n\right],$$

where $T_{\max}, T_0, c_{k,\max}, c_{k,0}$ are the maximal and minimal values of temperature and concentration of the *k*-th species; d_x, n are the parameters, determining a degree of non-homogeneity of the layer. Figure 6.27 shows typical distributions of temperature and molar fractions in the layer $T_0 = 300\,\mathrm{K}$, $T_{\max} = 2500\,\mathrm{K}$, ($c_{H_2O,0} = 0.01$, $c_{H_2O,\max} = 0.7$, $c_{CO_2,0} = 0.01$, $c_{CO_2,\max} = 0.3$).

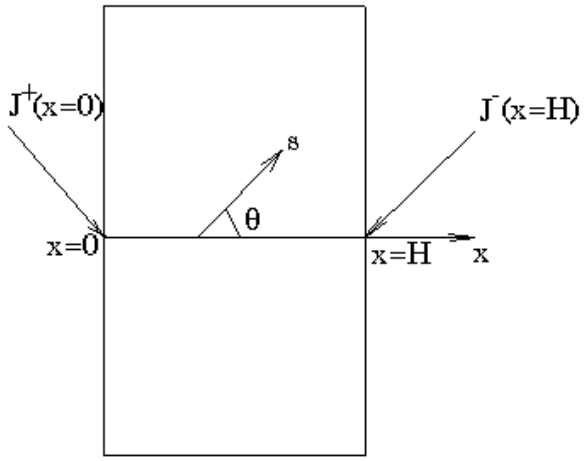

Figure 6.26: Scheme of the problem

Calculations of radiation heat transfer in the plane-parallel layer were performed with the "line-by-line" approach, and with the macro-random model. There are four vibrational bands of a molecule H_2O and four vibrational bands of a molecule CO_2 were taken into account in the following spectral region $\Delta\Omega = 1000 \div 10000\ \mathrm{cm}^{-1}$. Parameters of vibrational bands were borrowed from [22].

At the "line-by-line" calculations the spectral range $\Delta\Omega$ was broken on elementary spectral regions $\Delta\omega_i$, in the centre of each ω_i the total absorption coefficient (averaged on rotational structure) was calculated as follows:

$$\kappa(\omega_i) = 0.01\sum_{g=1}^{G_{H_2O}} \frac{C_{1,g}}{C_{3,g}}\exp\left(-\frac{|\omega_i - \omega_g|}{C_{3,g}}\right)\rho_{H_2O} + 0.01\sum_{g=1}^{G_{CO_2}} \frac{C_{1,g}}{C_{3,g}}\exp\left(-\frac{|\omega_i - \omega_g|}{C_{3,g}}\right)\rho_{CO_2}, \tag{58}$$

where G_{H_2O}, G_{CO_2} are the numbers of vibrational bands, taken into account for H_2O and CO_2 accordingly; ρ_{H_2O}, ρ_{CO_2} are densities of H_2O and CO_2. The pressure in the layer was supposed as atmospheric ($p = 1\,\mathrm{atm}$), therefore density of the *k*-th molecular component (with molecular weight M_k) is calculated under the formula:

$$\rho_k = M_k x_k p \frac{10^5}{8314}, \text{ kg/m}^3.$$

The absorption coefficient (58) was supposed constant in the limits of $\Delta\omega_i$.

Spectral absorption coefficient in two points inside the plane-parallel layer, used in the "line-by-line" calculations is shown in Figure 6.28. Distributions of total half-moment functions in the plane-parallel layer are shown in Figure 6.29. Figure 6.29 shows distribution of the total integrated flux obtained in the "line-by-line" calculations:

$$W_T(x) = M_1^+(x) + M_1^-(x),$$

and also relative error of these calculation with the use of the macro-random model ($W_{MSM}(x)$):

$$\varepsilon = \frac{|W_T(x) - W_{MSM}(x)|}{|W_T(x)|}.$$

Figure 6.30 shows distribution of divergence of the total integrated flux and error of its calculation with the use of the macro-random model. Divergence of radiating flux defines volumetric capacity of heat release, therefore this function is first of all necessary for the solution of radiative-convective interaction.

One can see that the error of prediction of the radiation function with the macro-random model is about ~ 30%, that is quite acceptable for the practice of calculations of radiative heat transfer. In separate very narrow sites this error can reach up to several hundreds of percents. However it is observed only in those points inside a layer, where the total integrated flux or divergence of the flux are close to zero, therefore the specified errors do not worsen the accuracy of the given approximate method.

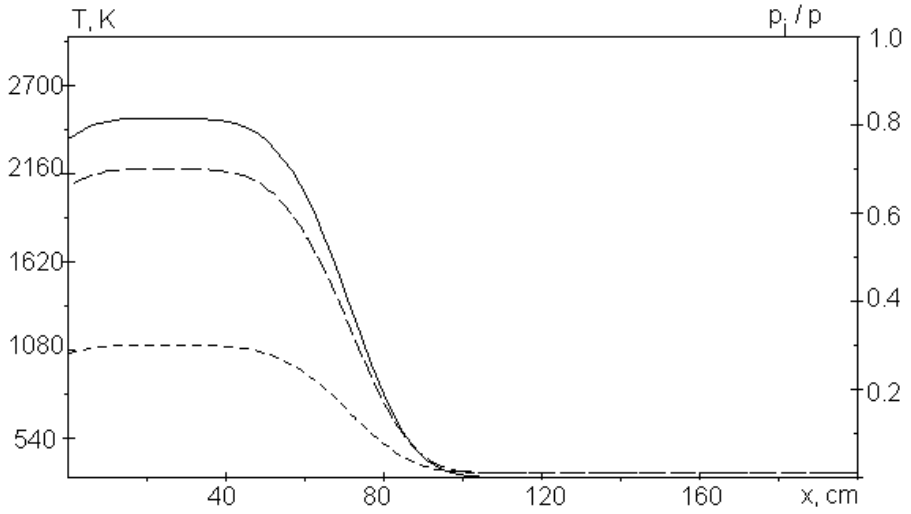

Figure 6.27: Distribution of temperature (solid line, scale at the left), and molar fractions of water vapor (long dashed line; scale at the right) and carbon dioxide (short dashed line; scale at the right)

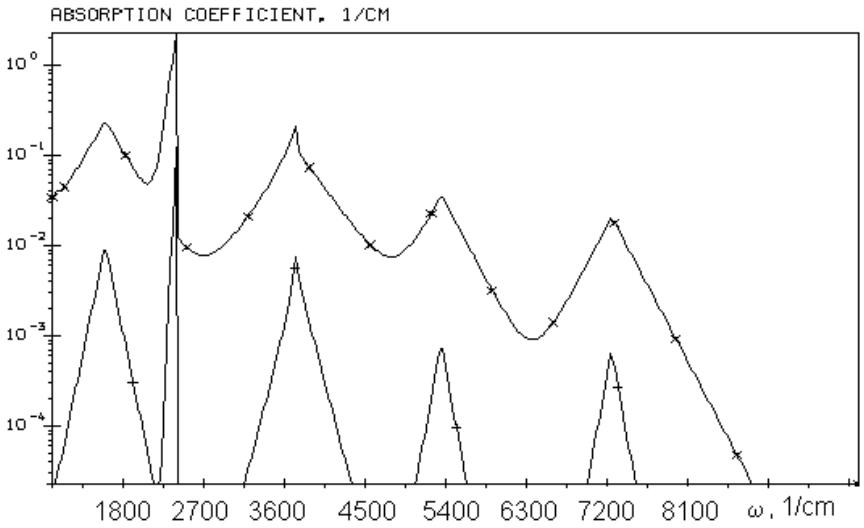

Figure 6.28: Spectral absorption coefficient, averaged on rotational structure in points of the layer with coordinates $x = 0$ (1) and $x = H$ (2)

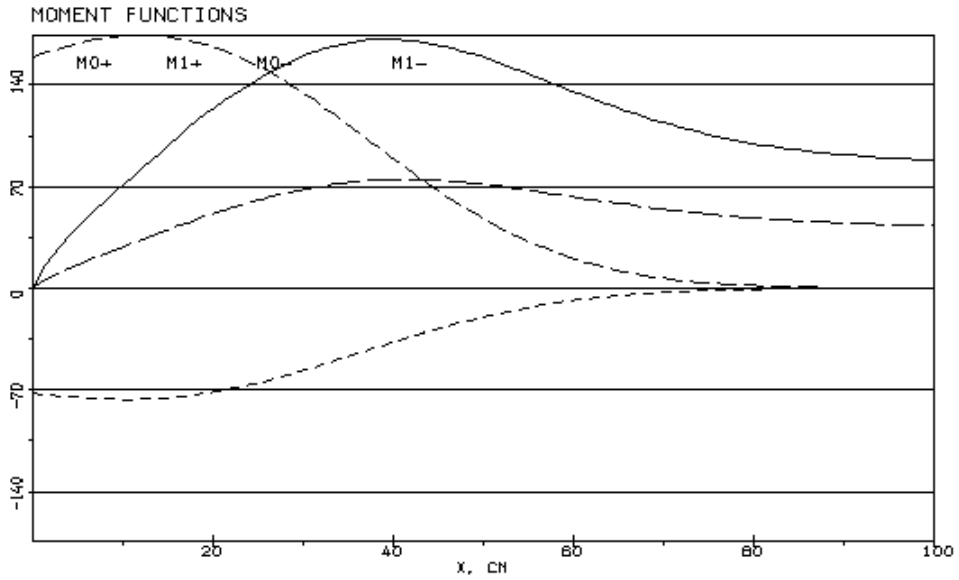

Figure 6.29: Total half-moment characteristics in the plane-parallel layer

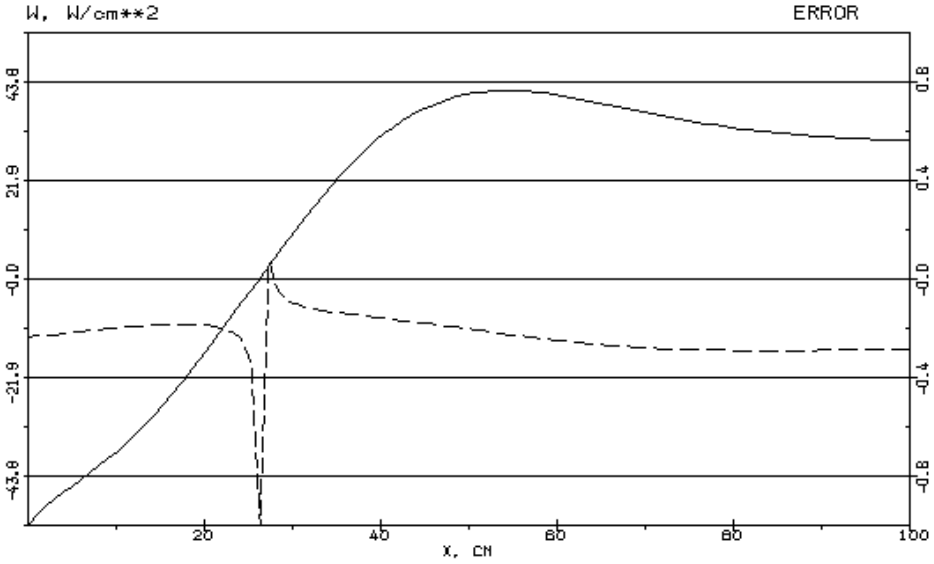

Figure 6.30: Density of the total integrated radiating flux in the layer (solid line; scale at the left) and error of its calculation with use of macro-random model (dashed line; scale at the right)

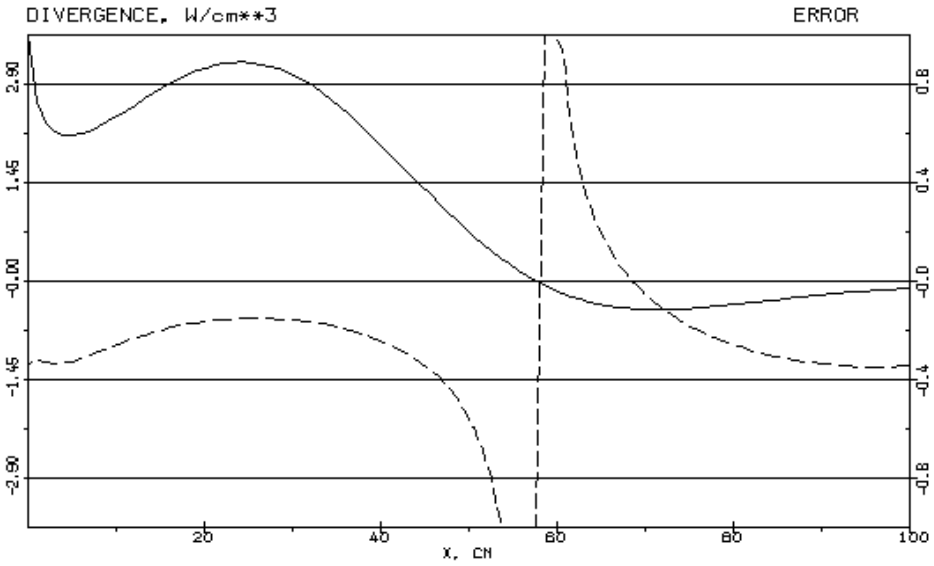

Figure 6.31: Divergence of the total integrated flux in the layer (solid line; scale at the left) and error of its calculation with the use of macro-random model (dashed line; scale at the right)

6.7 The Monte-Carlo method

6.7.1 Monte-Carlo prediction of signature of model solid rocket motor plume on non-orthogonal grids [31]

Imitative Monte-Carlo algorithm of quasi-random sampling (see Section 5.7) is used here for prediction of spectral signature of multi-phase plume of model solid rocket motor (SRM). Gas dynamic functions of the model SRM plume are shown in Figures 6.32. These are: gas temperature (*a*), temperature of solid particles (*b*), volume concentration of the monodisperse cloud of Al_2O_3 particles with radius of particles of 2 microns (*c*), molar fractions of H_2O (*d*) and CO_2 (*e*). Non-orthogonal computational grid used for these calculations is shown in Figure 6.32, f.

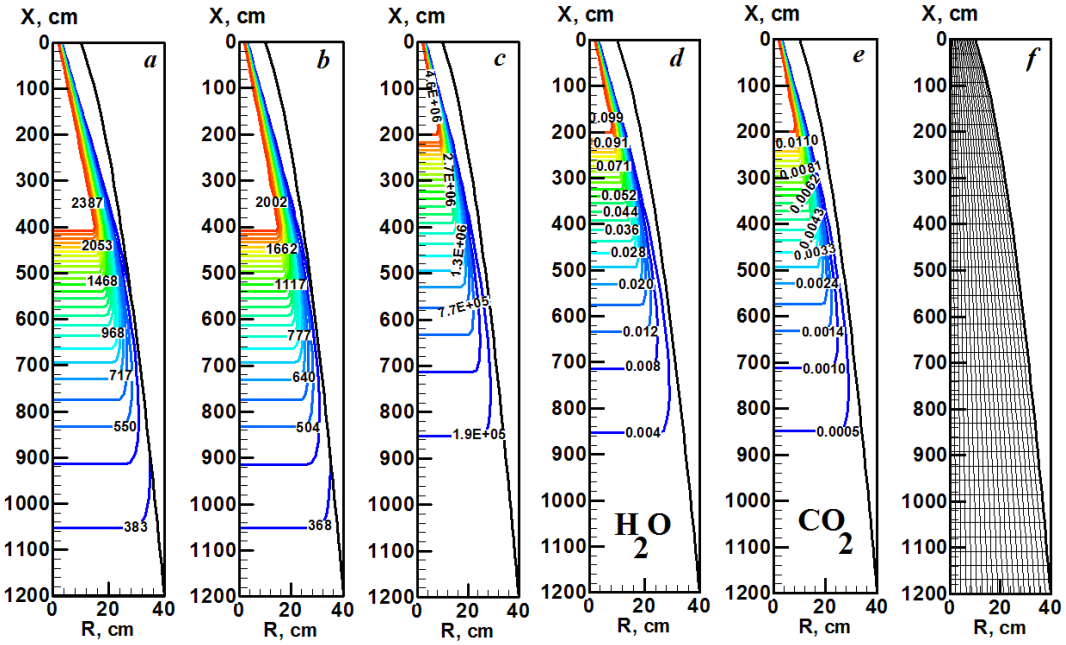

Figure 6.32: Gas temperature (*a*), temperature of Al_2O_3 particles (*b*) and volume concentration of Al_2O_3 particles in model scattering plume of SRM (*c*) on the non-orthogonal axysimmetric grid

Calculations were performed for infrared region of spectrum corresponding to center of strong absorption band of water vapors (the 2.7μ-band), $\Delta\omega = 3600 \div 3620\ \text{cm}^{-1}$. Pressure in the plume was assumed to be $p = 1\text{atm}$. A spectral absorption coefficient in spectrum of the Lorentzian rotational lines inside and outside of not scattering and scattering model SRM plumes is shown in Figure 6.33.

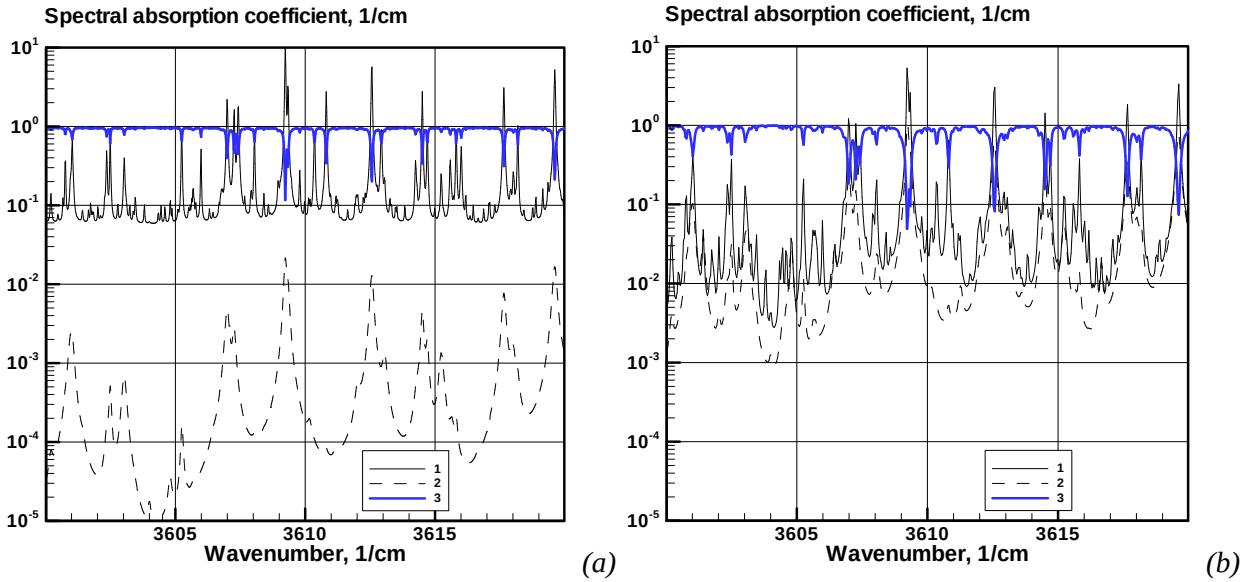

Figure 6.33: Spectral absorption coefficient in two points inside scattering model plume; *a*: solid line – *X* = 0, *R* = 0, dashed line – *X* = 0, *R* = 10 cm; *b*: solid line – *X* = 600 cm, *R* = 0, dashed line – *X* = 600 cm, *R* = 30 cm. Albedo of the single scattering (the bold solid line) inside scattering model plume (*a*: *X* = *R* = 0; *b*: *X* = 600 cm, *R* = 30 cm)

The computational case of the light-scattering plume is characterized by presence of spectral regions with very high single-scattering albedo, that is by the very high probability of scattering (Figures 6.33,a,b).

Results of the Monte-Carlo calculations of integral and spectral signatures of model non-scattering plume on the non-orthogonal grid are shown in Figures 6.34–6.36. Dependences of integral directional signature of the plume from the angle of observation, calculated with use of three described imitative methods, are shown in these figures. The Monte-Carlo simulation algorithms, which use methods of the quasi-random sampling (Figure 6.34) and the Maximum Cross-Section (Figure 6.35), give close results.

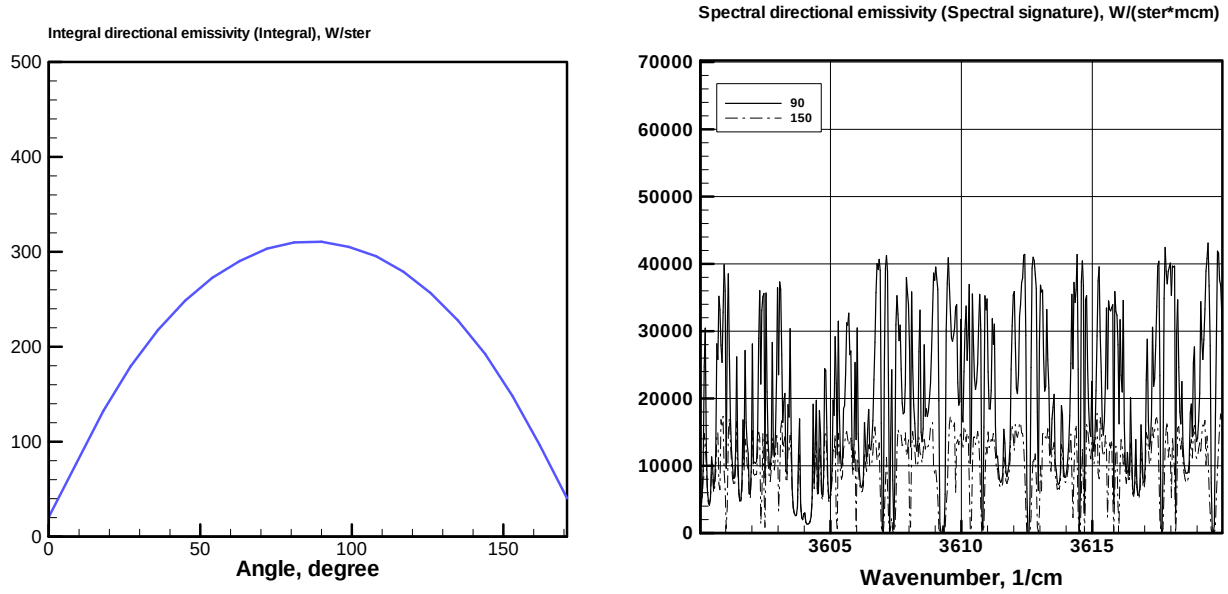

Figure 6.34: Left: Integral signature of non-scattering plume vs. angle θ of the plume observation. Right: Spectral signature of SRM in two directions to *X*-axis (θ = 90° and θ = 150°). The direct LBL Monte Carlo method on non-orthogonal axysimmetric grid (number of points along photon trajectory: 30)

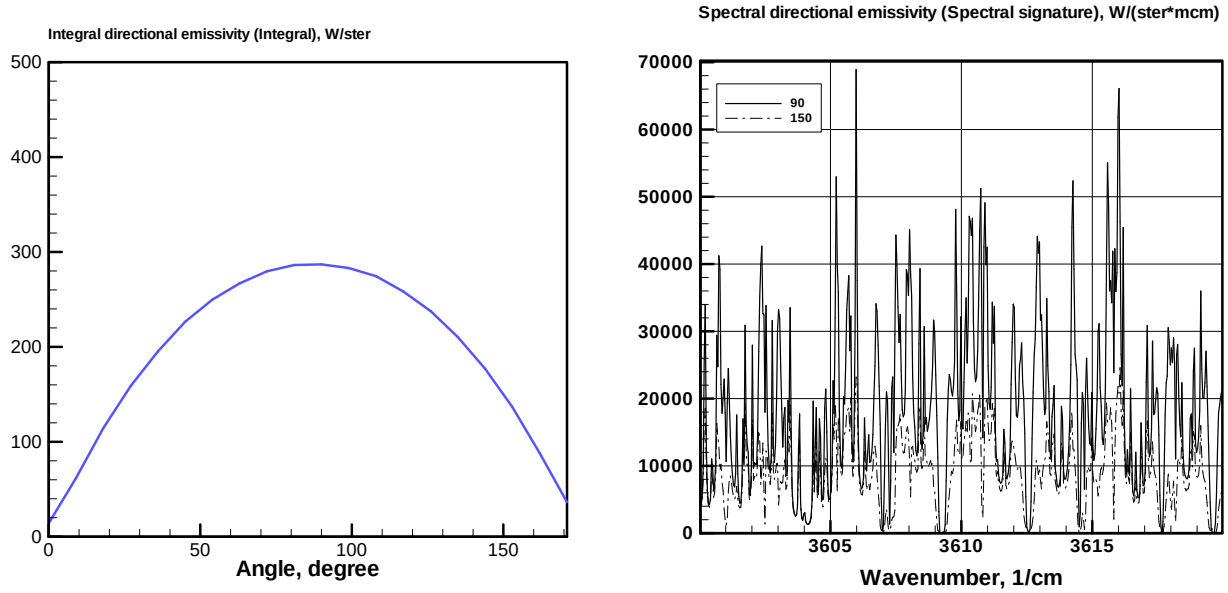

Figure 6.35: Left: Integral signature of non-scattering model plume of SRM vs. angle θ of the plume observation. Right: Spectral signature of non-scattering model plume of SRM in two directions of observation to *X*-axis (θ = 90° and θ = 150°). The LBL Monte Carlo method with the Maximal Cross-Section algorithm on non-orthogonal axysimmetric grid

The hybrid method (Figure 6.36) gives the overestimated results in the normal direction to *X*-axis. However, it is necessary to note, that the optimization of approximating parameters of molecular rotational lines statistical models was not performed in this case.

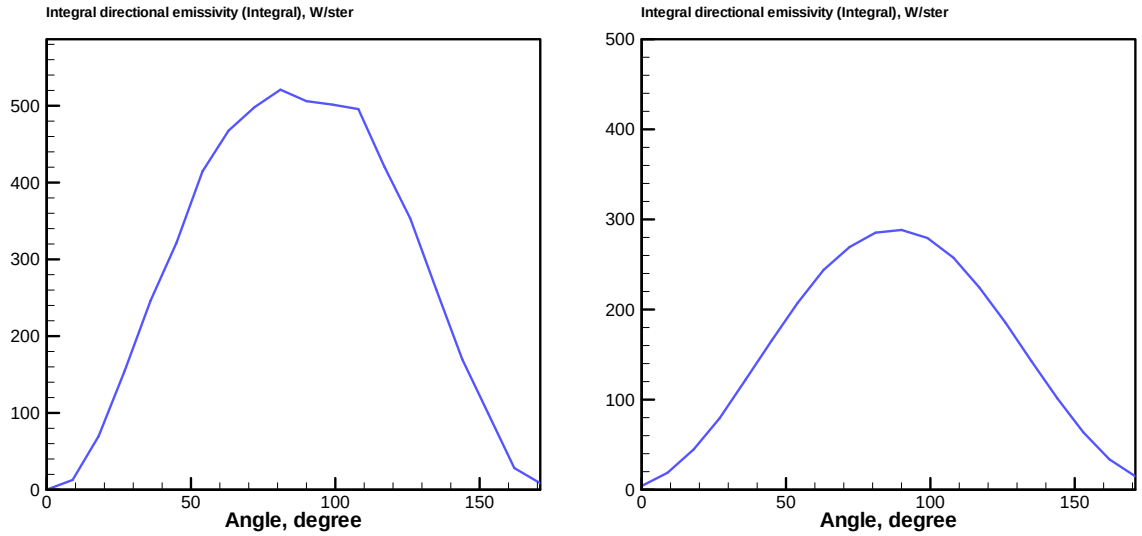

Figure 6.36: Integral signature of non-scattering model plume of SRM vs. angle θ of the plume observation (the angle θ is counted off from the *X*-axis). Left: the Hybrid Monte Carlo method. Right: the Direct LBL Monte Carlo method (number of points along photon trajectory: 30)

The spectral dependences of signatures at two angles of observation, which are presented in Figures 6.34 and 6.35, show some differences in separate narrow spectral ranges. These differences can be referred to statistical errors of the Monte-Carlo algorithms.

Calculation results for integral and spectral signatures for scattering plume of the model SRM are shown in Figures 6.37–6.39.

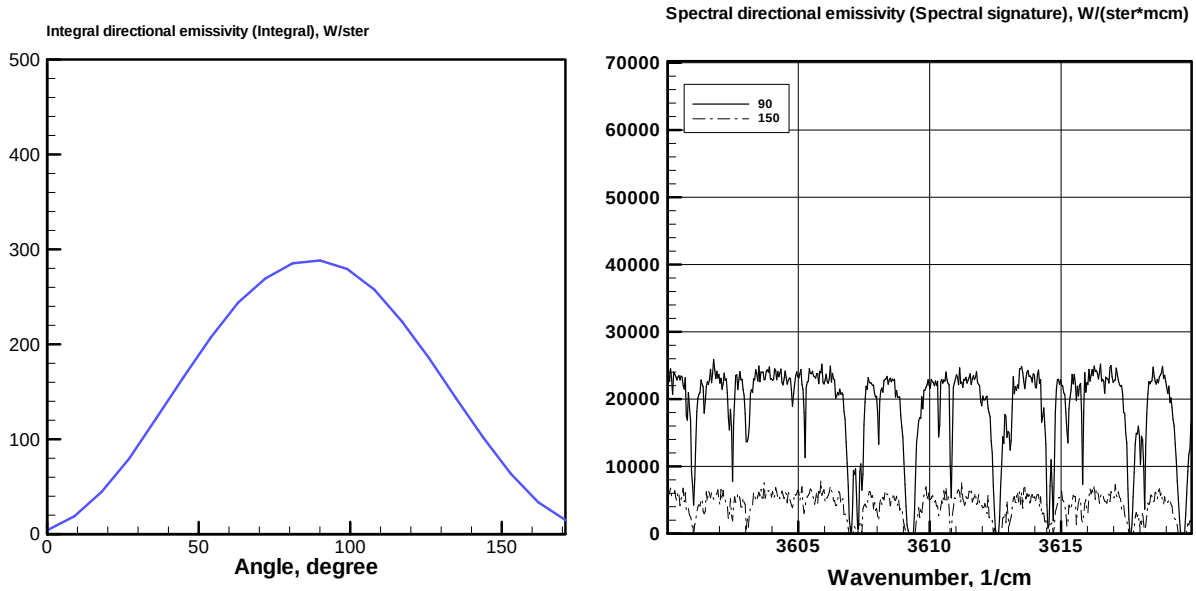

Fig.6.37 Integral signature (left) of scattering model plume of SRM vs. angle θ of the plume observation. Spectral signature (b) of scattering model plume of SRM in two directions to *X*-axis (θ = 90° and θ = 150°). The direct LBL Monte Carlo method (number of points along photon trajectory: 30)

As well as for the non-scattering medium, the results obtained by two LBL-methods are rather close. It concerns both to the total signature (Figures 6.37,a and 6.37,b) and to the spectral signature (Figures 6.37,b and 6.38,b).

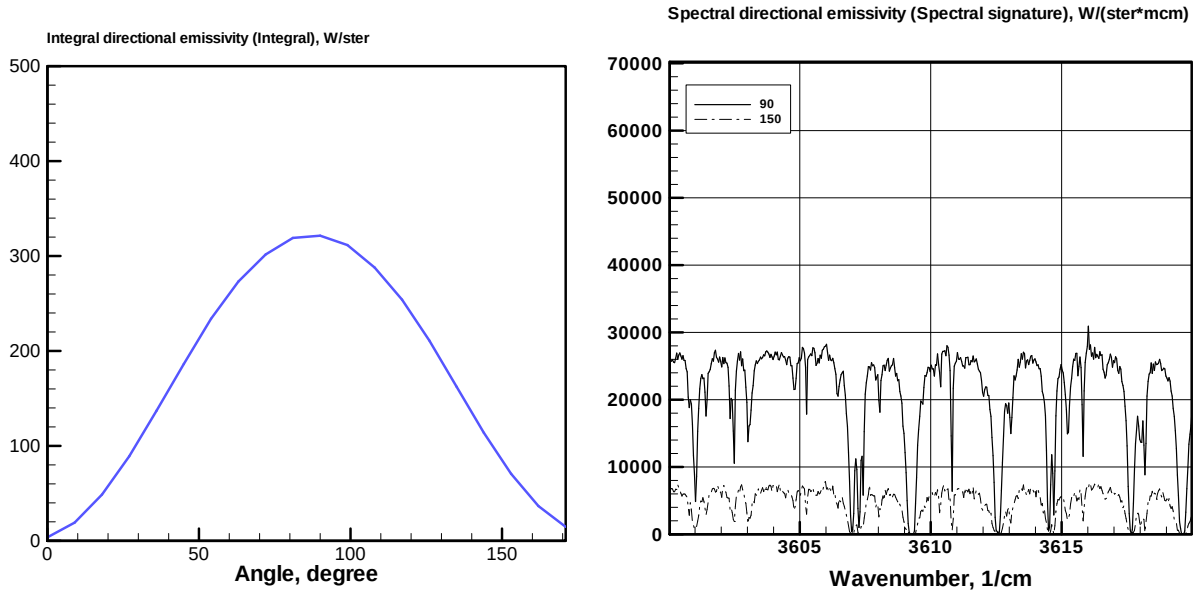

Figure 6.38: Integral signature (a) of scattering model plume of SRM vs. angle θ of the plume observation. Spectral signature of scattering model plume of SRM in two directions to *X*-axis (θ = 90° and θ = 150°). The LBL Monte Carlo method with the Maximal Cross-Section algorithm

The hybrid method also shows rather good accuracy in the case under consideration (Figure 6.39).

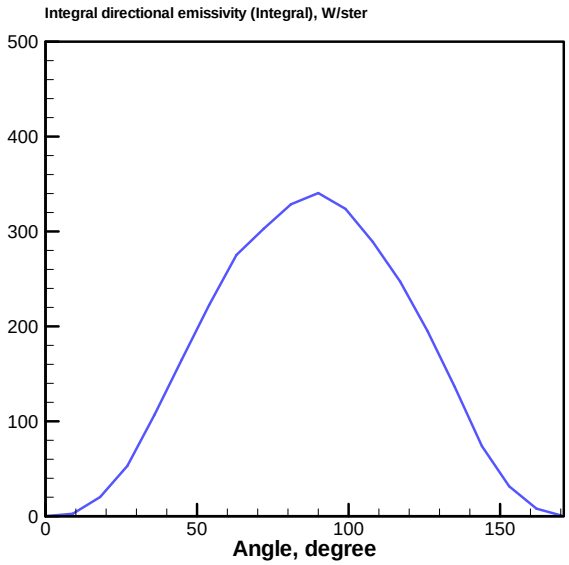

Figure 6.39: Integral signature of scattering model plume of SRM vs. angle θ of the plume observation. The Hybrid Monte Carlo method

Presented data allow make conclusion about effect of scattering on a signature of plumes. Let us compare, for example, the spectral signature calculated by the LBL-method with the Maximum Cross-Section method for non-scattering (Figure 6.35) and for scattering (Figure 6.38) plumes. Scattering processes become apparent appreciably for angles of observation far from 90. This is because in paraxial directions the absorption probability of photons increases. Integral radiation in the normal direction to the axis of

symmetry in this case changes insignificantly, however the spectral distribution of radiation undergoes noticeable changes: the spectral signature of the light-scattering plume has smaller oscillations on the spectrum. This fact also can be explained by the presence of additional absorber (particles of Al_2O_3) and by much higher probability of photon survival at any elementary collision act of photons with particles of the medium.

6.7.2 Monte-Carlo prediction of spectral emissivity of three-dimensional plumes [33]

Developed algorithm of imitating modeling of radiation heat transfer in a three-dimensional case was used for analysis of spectral and integral signatures of model jet shown in Figures 6.40–6.42. Two calculation cases were analyzed. The first one is the weak light-scattering plume (concentration of Al_2O_3 particles in the exit cross section of each SRM is $n_p = 5\times10^3$ cm^{-3}), and the second is the strong light-scattering plume (concentration of Al_2O_3 particles Al_2O_3 exit cross section of each SRM is $n_p = 10^7$ cm^{-3}). The average radius of particles was presumed equal to 2 and 20 microns.

Distribution of temperatures of gas and condensed phase were set on the basis of the approached analytical solution of the problem about two-phase plume, and distribution of mass fractions of optically active components was set on the base on theory of analogy of heat and mass transfer processes. Spectral optical properties of combustion products were calculated with use of the computer system ASTEROID [1, 47]. Calculations of the optical properties of particles Al_2O_3 were performed with the use of the Mie theory [29]. Spectral calculations of radiation heat transfer were performed for 100-group model of optical properties with averaging of rotational structure of molecular spectrum. Trajectories of 10^5 groups of photons were modeled in each spectral group. Control calculations were executed at modeling of 10^6 groups of photons in each spectral group.

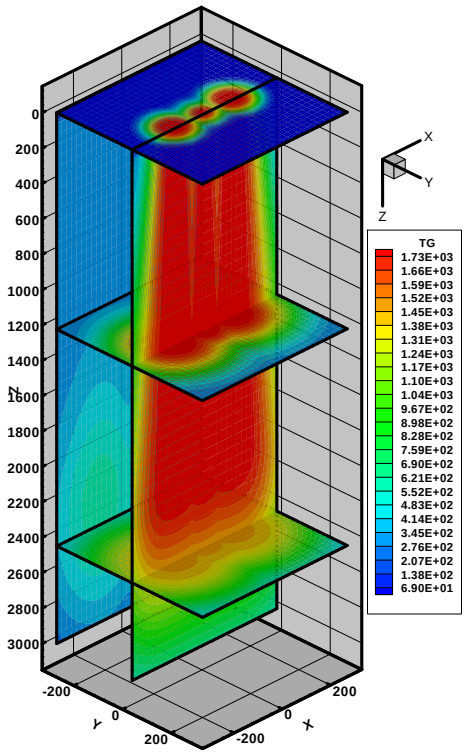

Figure 6.40: Gas temperature in three-block plume

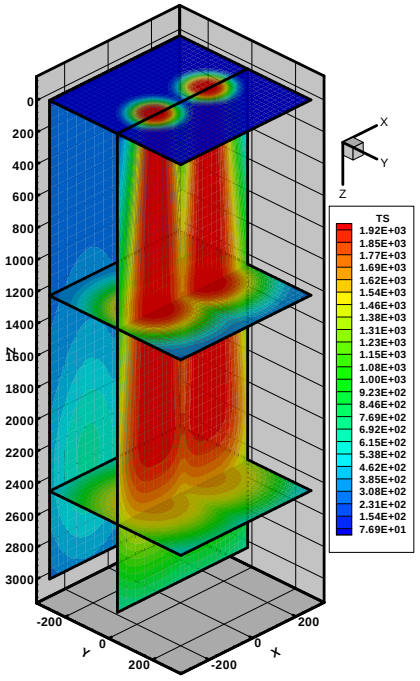

Figure 6.41: Temperature of Al_2O_3 particles in three-block plume

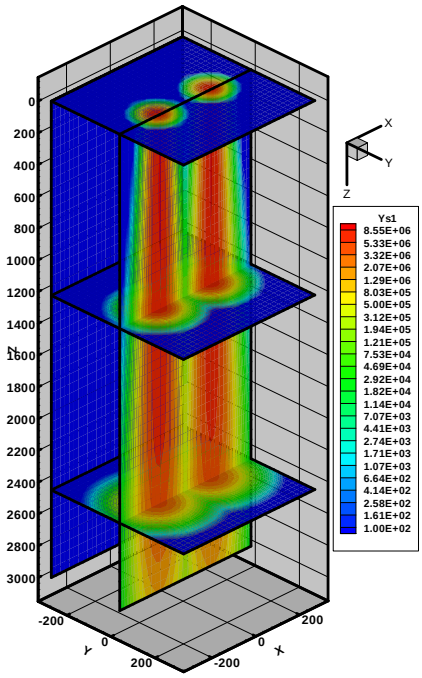

Figure 6.42: Concentration of Al_2O_3 particles in three-block plume

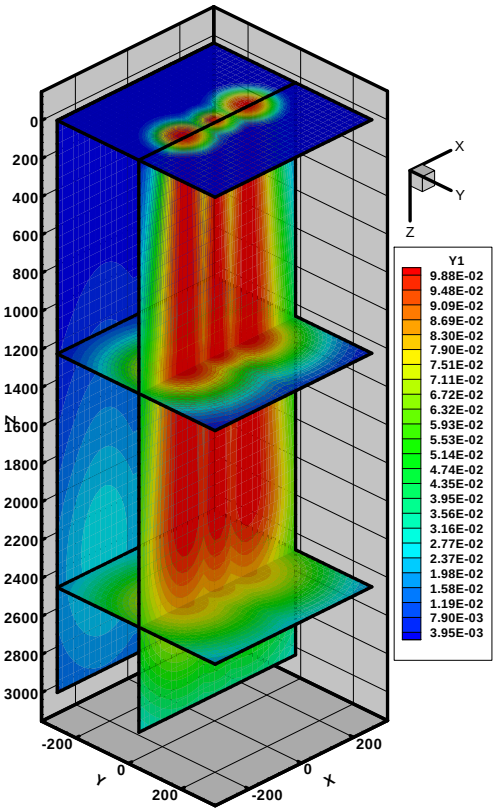

Figure 6.43: Mass fraction of H_2O

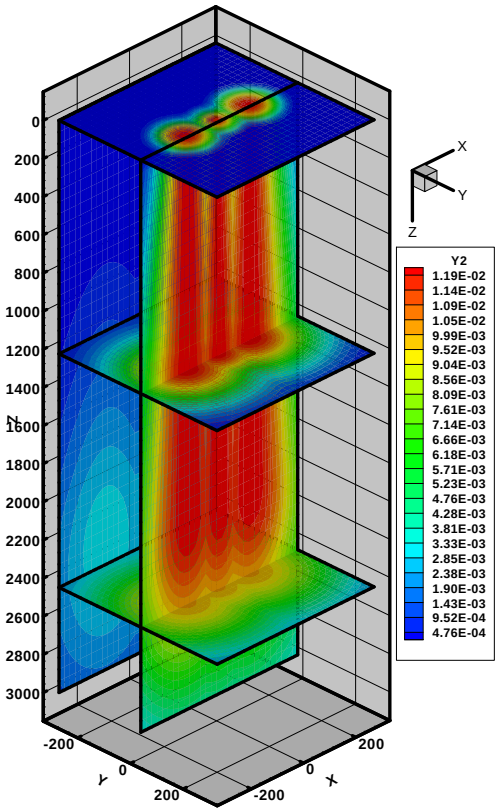

Figure 6.44: Mass fraction of CO_2

Signatures of radiation of three-block plume are shown in Figures 6.45 and 6.46. Created calculation algorithm demonstrates symmetry of received results in relation to turn on 90°. In the first case (Figure 5.45) signature of the plume in *YZ* plane exceeds radiating ability from *XZ* plane. A reverse situation is observed in the second case (Figure 5.46). Marked regularities for integral radiation are repeated also for the spectral signature. In the considered case, as before, radiating ability is formed in the centers of vibrational bands, and the solid phase radiation is distinctly visible in transparency windows of vibrational bands.

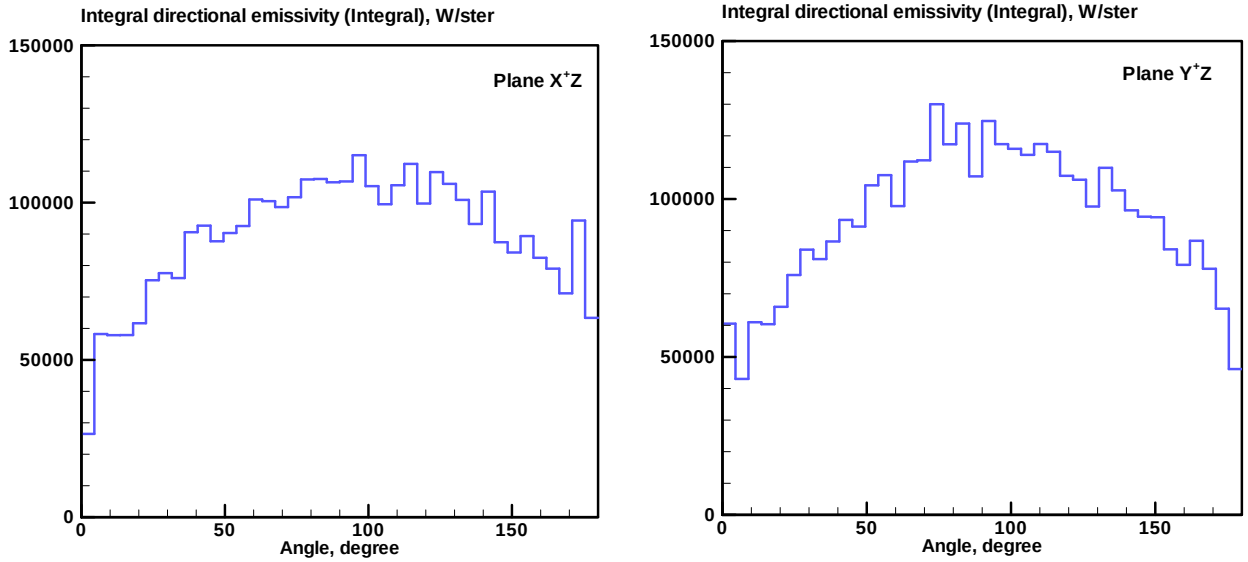

Figure 6.45: Integral signature of the three-block plume with high level of scattering; Observation of plane at $x = x_{max}$ (left) and plane $y = y_{max}$ (right)

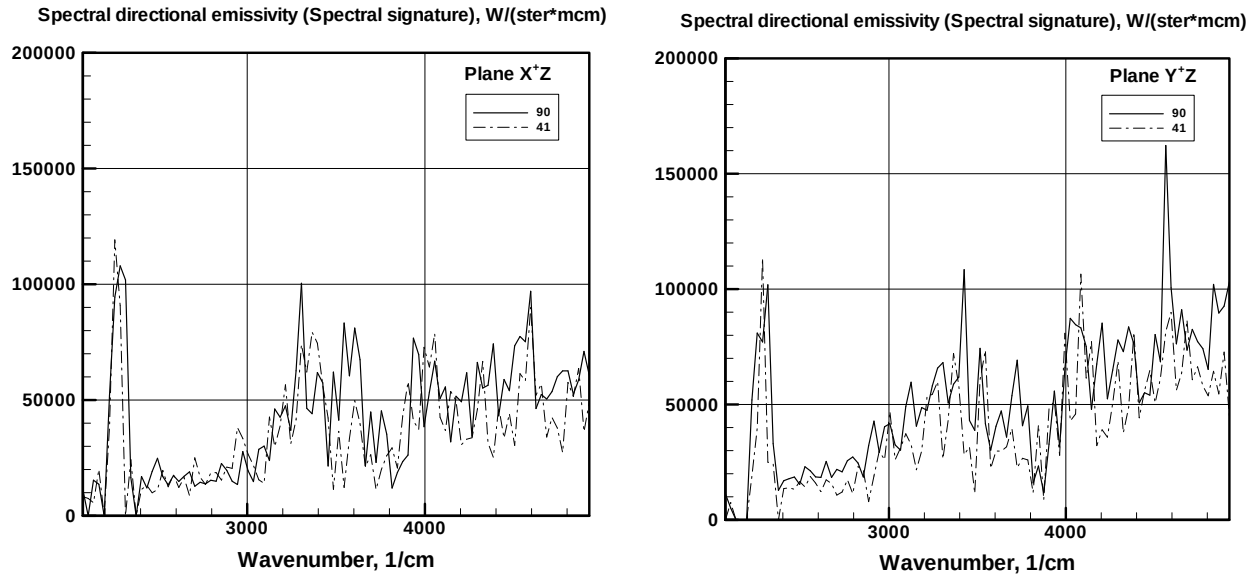

Figure 6.46: Spectral signature of the three-block plume with high level of scattering; Observation of plane at $x = x_{max}$ (left) and plane $y = y_{max}$ (right)

6.7.3 Monte-Carlo simulation with line-by-line spectral modelling [49]

Computing code Plume-3D-MC was used for interpretation of the ERIM experimental data [2], and to systematic study of selective radiation heat transfer from cloud of hot gases through cold air atmosphere [50]. To focus attention on verification of spectral optical models included into code Plume-3D-MC the problem of prediction of spatial radiation characteristics was significantly simplified in comparison with previous study. In this case homogeneous cylindrical volume of height $H_{hc} = 60$ cm and radius $R_{hc} = 30$ cm contains mixture of water vapour or carbon dioxide with molecular nitrogen at temperature $T \sim 1200$ K and pressure $p = 0.1$ atm. Such conditions were experimentally studied in [50].

Cylindrical volume involving heated mixture of H_2O/N_2 at temperature $T = 1202$ K and total pressure $p = 0.1$ was considered in the second case. Molar fractions of gas species are $x_{H_2O} = 0.5$, $x_{N_2} = 0.5$. Numerical prediction of spectral radiation intensity of the heated volume in normal direction to plane surface are shown in Figure 6.47. Optical properties of heated H_2O were borrowed from NASA standard infrared radiation model [35], where rotational line structure was averaged in each spectral group of $\Delta\omega = 25\,\text{cm}^{-1}$. Experimental data [50] are presented for spectral region $\Delta\Omega = 3000 \div 4200\,\text{cm}^{-1}$. These calculations were performed with the same spectral resolution. Spectral absorption coefficient calculated at these conditions is shown in Figure 6.48.

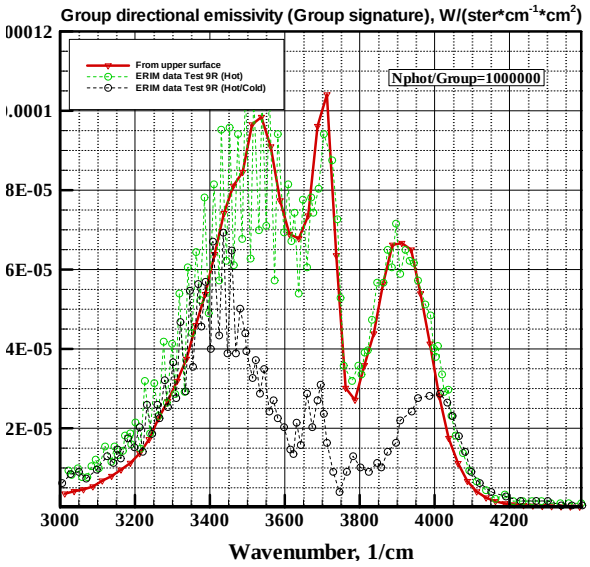

FIGURE 6.47: TEST 9R. ERIM EXPERIMENTAL DATA FOR H2O HOT CELL RADIANCE (UPPER DOTTED LINE), HOT-THROUGH-COLD RADIANCE (LOWER DOTTED LINE), AND PLUME-3D-MC NUMERICAL PREDICTION (SOLID LINE) OF THE HOT CELL RADIANCE. NASA STANDARD INFRARED RADIATION MODEL; AVERAGED ROTATIONAL LINE STRUCTURE; SPECTRAL REGION FOR EACH SPECTRAL GROUP IS $\Delta\omega = 25$ CM–1

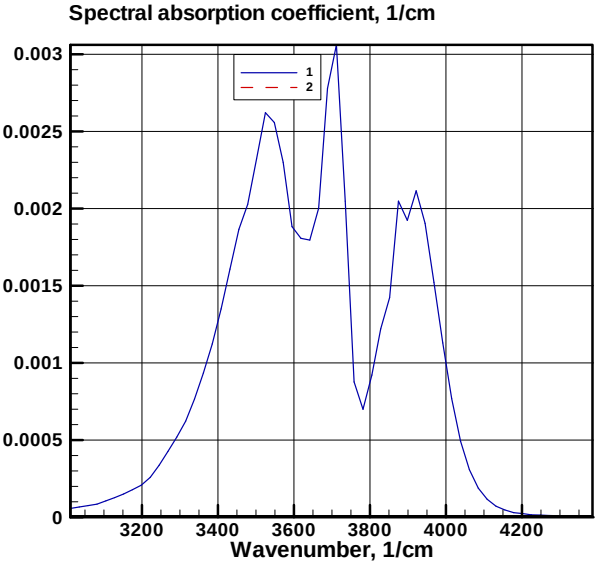

FIGURE 6.48: SPECTRAL ABSORPTION COEFFICIENT OF HEATED H2O FOR CONDITIONS OF TEST 9R. NASA STANDARD INFRARED RADIATION MODEL

Observed in Figure 6.47 good agreement between theoretical prediction and ERIM experimental data indicates that optical model [35] provides adequate data for the case under consideration.

Cylindrical volume involving heated mixture of CO_2/N_2 at temperature $T = 1200\,\mathrm{K}$ and total pressure $p = 0.1$ was considered in the second case. Molar fractions of the gas species are $x_{C_2O} = 0.5$, $x_{N_2} = 0.5$. Other initial conditions were the same as in the first calculation series.

Numerical simulation results for spectral intensity obtained with the use of code Plume-3D-MC are shown in Figure 6.49. The NASA standard infrared radiation model [35] was used in these calculations. Averaged over rotational line structure spectral absorption coefficient of hot mixture CO_2/N_2 for conditions of experimental research [50] (Test 5) is shown in Figure 6.50.

Considered above numerical prediction of spectral radiation intensity of heated volumes of H_2O/N_2 and CO_2/N_2 for conditions of experiments [50] (Test 9R and Test 5), were obtained with the data accumulated in NASA standard infrared model [35]. It is of great practical interest to consider possibility to use other optical models for interpretation of the experimental data. Results of such investigations are presented in [49].

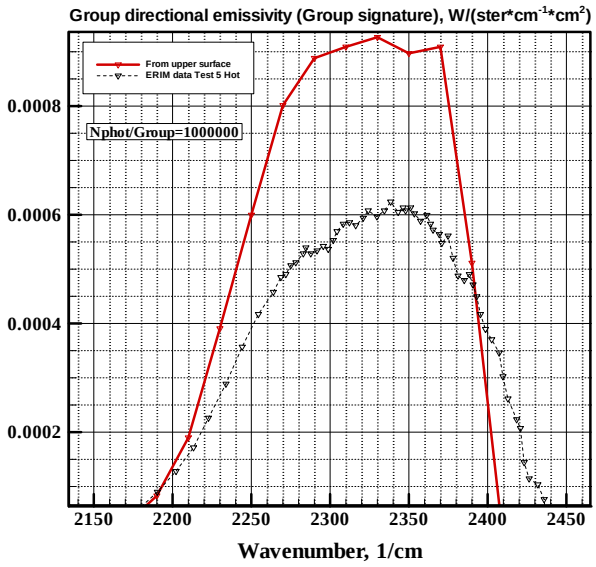

FIGURE 6.49: TEST 5. ERIM EXPERIMENTAL DATA FOR CO2 HOT CELL RADIANCE (DOTTED LINE) AND PLUME-2D-MC NUMERICAL PREDICTION (SOLID LINE) OF THE HOT CELL RADIANCE. THE NASA STANDARD INFRARED RADIATION MODEL; AVERAGED ROTATIONAL LINE STRUCTURE; SPECTRAL REGION FOR EACH SPECTRAL GROUP IS $\Delta\omega = 20$ CM–1

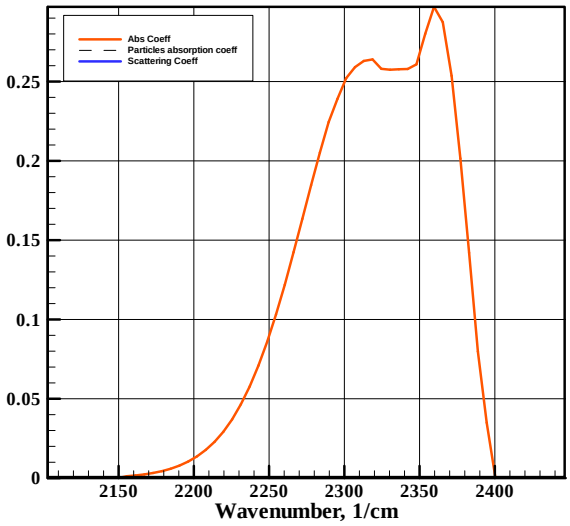

FIGURE 6.50: SPECTRAL ABSORPTION COEFFICIENT OF HEATED CO2 AT CONDITIONS OF TEST 5; NASA STANDARD INFRARED RADIATION MODEL [35]

Next calculation case corresponded to experimental data on observation of hot volumes of H_2O from large distances. Schematic of the problem is shown in Figure 6.51. Initial conditions were identical to real experimental investigation. Parameters of gas mixture inside heated volume: $p = 0.1$ is the total pressure, atm; $p_{H_2O} = 0.05$, $p_{N_2} = 0.05$ are the partial pressures of species, atm; $H = 60$ is the height of the heated cylindrical volume, cm; $T = 1202$ is the temperature of gas mixture, K. Parameters of surrounding cold gas are: $p = 0.07$ is the total pressure, atm; $p_{H_2O} = 0.001$, $p_{N_2} = 0.069$ are the partial pressures of species, atm; $L = 10000$ is the length of the optical path of observation, cm; $T = 293$ is the temperature in surrounding gas, K. Note, that parameters of hot gas model conditions in exhaust rocket plumes at altitude

about ~16 km, and parameters of cold gas model optical path of ~ 28.8 km at altitude 18 km. Note that the calculation domain contains to sub-domains (Figure 6.51). The first one exactly corresponds to conditions of experiment Test-9R. The second one, which models volume of cold gas, is 100 times smaller than in real experimental situation. To model radiation transfer in real conditions, the following approach was used in code Plume-3D-MC. An effective pressure of H_2O in surrounding gas was introduced: $p^*_{H_2O} = 100\, p_{H_2O} = 0.1$ atm, that is $x_{H_2O} = p^*_{H_2O} / p = 1.429$. But this effective pressure can be used only for prediction of averaged absorption coefficient (parameter S/d) for narrow-band random model of rotational lines. To calculate broadening of rotational lines in real surrounding conditions (parameter γ/d) one should use the real pressure $p = 0.07$ atm.

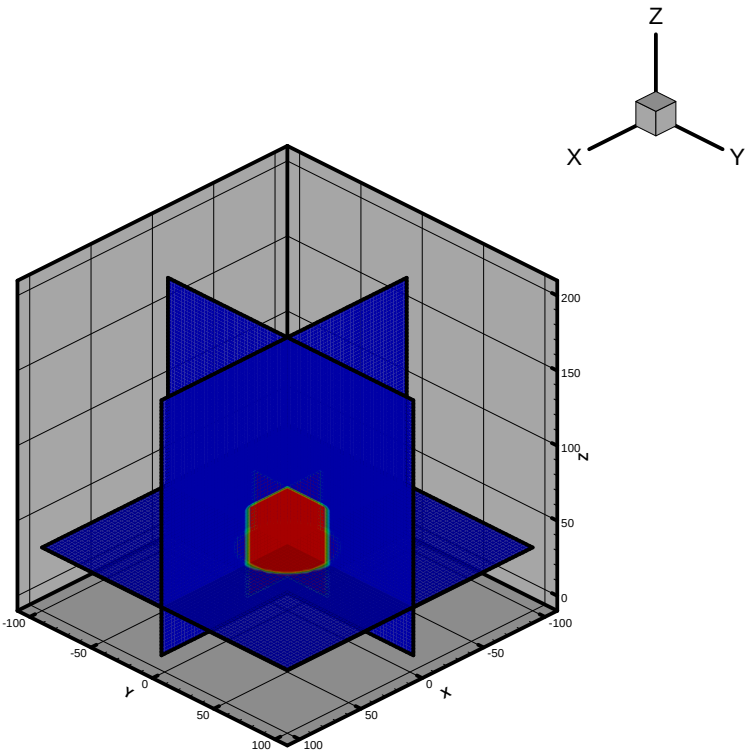

Figure 6.51: Schematic of the 3D "Hot/Cold" problem of visibility of heated cylindrical volume of H_2O/N_2 and CO_2/N_2 through cold atmosphere

Prediction of hot cell and hot-thought-cold spectral radiance by code Plume-3D-MC and NASA standard infra-red model with averaged rotational line structure is shown in Figure 6.52 and 6.53. One can see from these data that essentially, the problem is as follows: a major portion of heat radiation is absorbed in surrounding gas, containing resonant absorbing cold gas. Figure 6.51 shows comparison of experimental data and numerical prediction of hot-thought-cold spectral radiance for conditions of Test-9R experiments. Reference to Figure 6.51 shows that maximal discrepancy between experimental data and numerical prediction is observed within the region of maximal absorption ability of H_2O vibrational bands. At the same time, it is well known, that real spectra (vibrational bands) of emission and absorption contain large number of molecular rotational lines, therefore it might be assumed that the reason for the large discrepancy between experimental and numerical data is in using of non-adequate spectral optical model.

Figures 6.54 and 6.55 show numerical prediction of hot-through-cold spectral radiance for ERIM experimental conditions Test-9R (mixture H_2O/N_2), obtained by code Plume-3-MC with the use of narrow-random models [22]. Numerical simulation data presented in Figures 6.54 and 6.55 correspond to NASA standard infrared radiation optical model [35]. The following two spectral optical models of radiation transfer were used for both databases:

- the narrow-band random model for optically thin layers (the method of smoothing coefficients; see Section 5.3);
- the narrow-band random model of real spectrum (Figure 6.55).

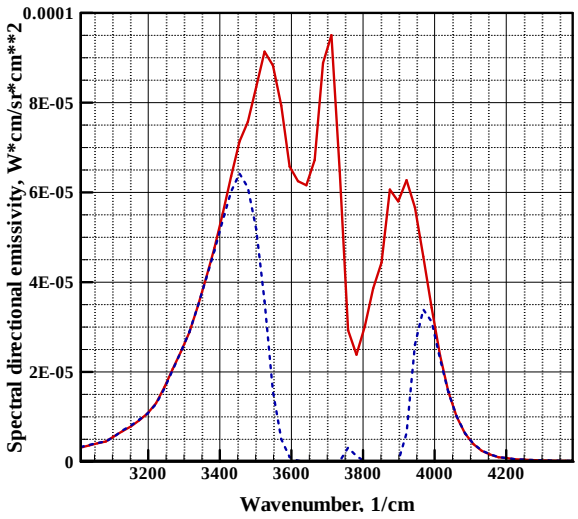

FIGURE 6.52: SPECTRAL SIGNATURE OF HOMOGENEOUS CYLINDRICAL VOLUME OF HEATED H2O UP TO $T = 1202$ K; 3D CALCULATION DOMAIN; $N_{ph} = 10^4$; THE MCLEDE ALGORITHM. SOLID LINE- PREDICTION OF HOT CELL RADIANCE (TEST 9R); DOTTED LINE – PREDICTION OF HOT-THROUGH-COLD CELL RADIANCE (TEST-9R). THE NASA STANDARD INFRARED MODEL

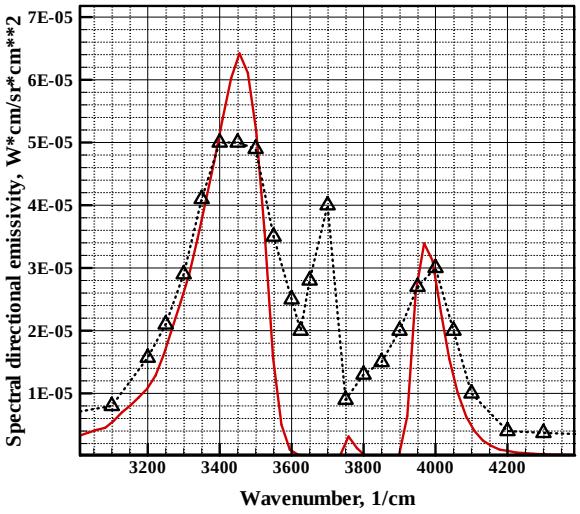

FIGURE 6.53: SPECTRAL SIGNATURE OF HOMOGENEOUS CYLINDRICAL VOLUME OF HEATED H2O UP TO $T = 1202$ K; 3D CALCULATION DOMAIN; $N_{ph} = 10^4$; THE MCLEDE ALGORITHM. CODE PLUME-3D-MC. SOLID LINE – PREDICTION OF HOT-THROUGH-COLD CELL RADIANCE, DOTTED LINE – ERIM EXPERIMENTS FOR TEST-9R

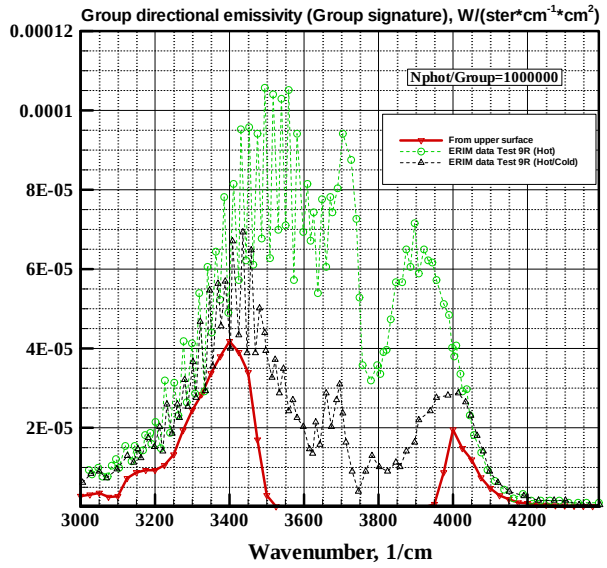

FIGURE 6.54: TEST 9R. ERIM EXPERIMENTAL DATA FOR H2O HOT CELL RADIANCE (UPPER DOTTED LINE), HOT-THROUGH-COLD RADIANCE (LOWER DOTTED LINE), AND PLUME-3D-MC NUMERICAL PREDICTION (SOLID LINE) OF THE HOT –THROUGH-COLD RADIANCE. THE NASA STANDARD INFRARED RADIATION MODEL; THE METHOD OF SMOOTHING COEFFICIENT; SPECTRAL REGION FOR EACH SPECTRAL GROUP IS $\Delta\omega = 25$ CM–1

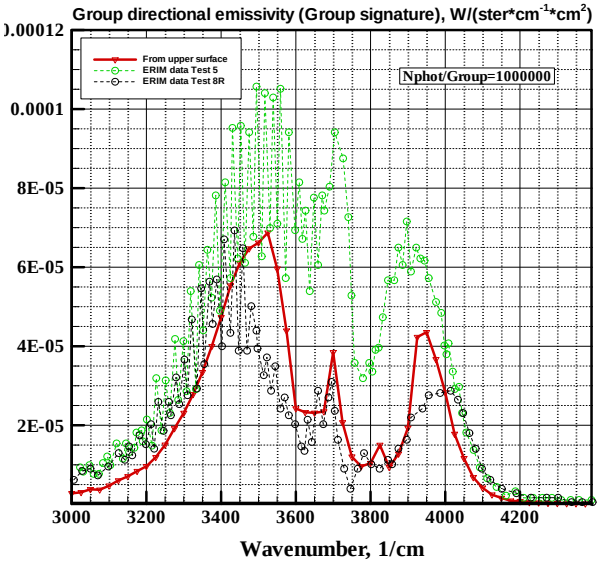

FIGURE 6.55: TEST 9R. ERIM EXPERIMENTAL DATA FOR H2O HOT CELL RADIANCE (UPPER DOTTED LINE), HOT-THROUGH-COLD RADIANCE (LOWER DOTTED LINE), AND PLUME-2D-MC NUMERICAL PREDICTION (SOLID LINE) OF THE HOT –THROUGH-COLD RADIANCE. THE NASA STANDARD INFRARED RADIATION MODEL; RANDOM MODEL (JLBL = 2); SPECTRAL REGION FOR EACH SPECTRAL GROUP IS $\Delta\omega = 25$ CM–1

With reference to presented numerical simulation data (Figure 6.55), it can be seen that narrow-band random models provide reasonable prediction of hot-through-cold spectral radiance for ERIM experimental conditions. However, some discrepancies between predicted and experimental data (inside separate spectral regions) have engaged our attention, and it substantiates necessity in further development of spectral optical models of heated gases and radiation heat transfer.

And finally, prediction of hot-through-cold radiance with the use of line-by-line spectral models based on HITRAN-like databases will be considered. Figures 6.56,a-d show numerical prediction of hot cell spectral radiance for ERIM experimental conditions Test-9R (mixture H_2O/N_2), obtained by code Plume-3D-MC with the use of line-by-line model. These numerical simulation data were obtained with the use of parameters of rotational lines from HITRAN database [36].

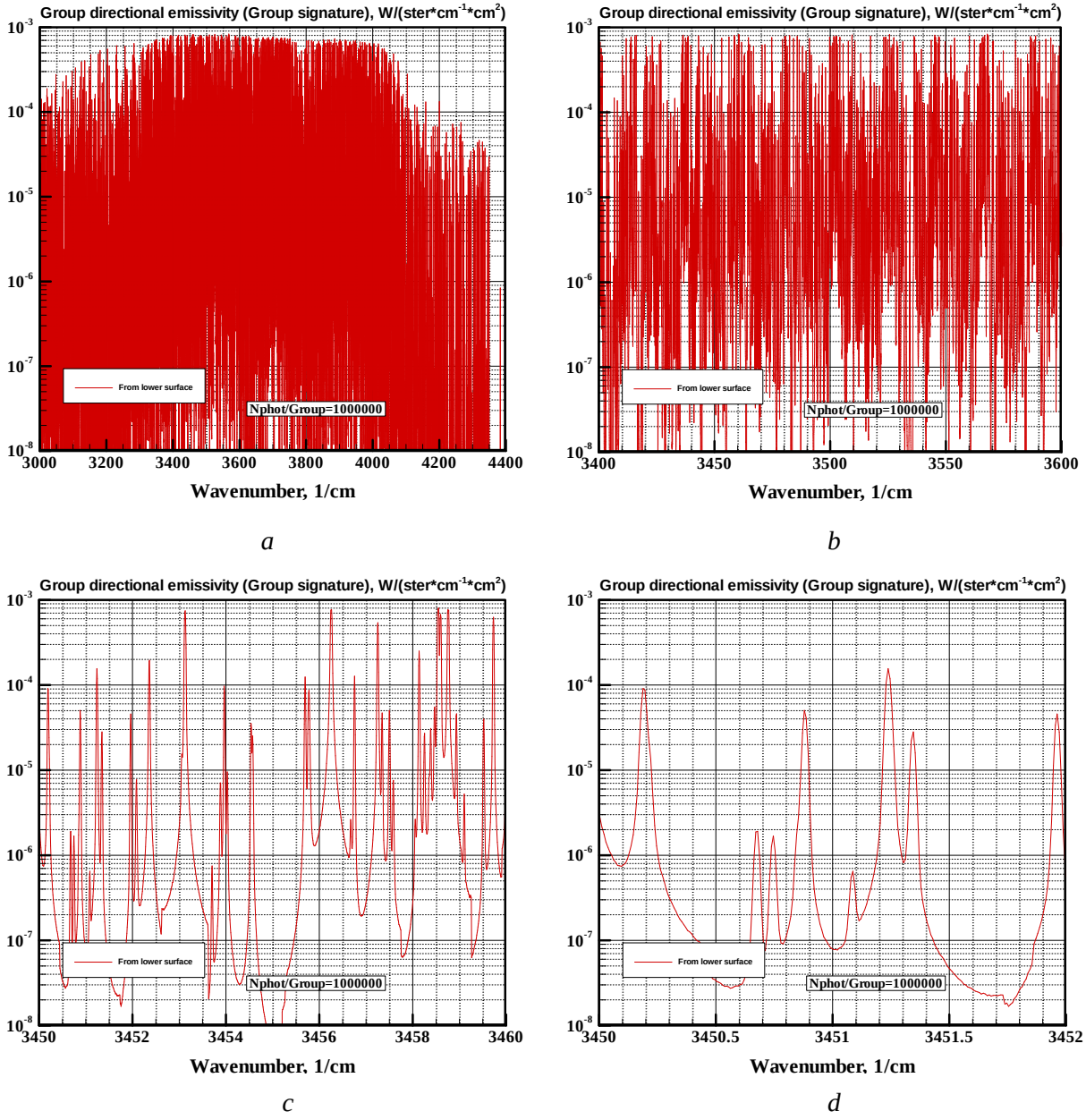

Figure 6.56: Line-by-line prediction of spectral intensity for conditions of ERIM experiments (Test 9R); Hot cell H_2O/N_2 radiance; spectral resolution is $\Delta\omega = 0.0083\ \text{cm}^{-1}$

Figure 6.56,a shows spectral intensity of hot cell radiance in spectral region $\Delta\Omega = 3000 \div 4400\ \text{cm}^{-1}$. This spectral region was divided by 56 spectral groups. The Monte-Carlo simulation of radiation transfer was performed in 3000 spectral points inside each spectral group. Thus, the spectral resolution of these calculations was about $\sim \Delta\omega = 0.0083\ \text{cm}^{-1}$. Figures 6.56,b-d show the spectral intensity inside successfully decreasing spectral regions (up to $\Delta\Omega = 3450 \div 3452\ \text{cm}^{-1}$). Figures 6.57,a–c show numerical prediction of hot-through-cold spectral radiance for ERIM experimental conditions Test-9R (mixture H_2O/N_2), obtained by code Plume-3D-MC with the use of line-by-line model. These numerical simulation data were also obtained with the use of parameters of rotational lines from HITRAN database [36].

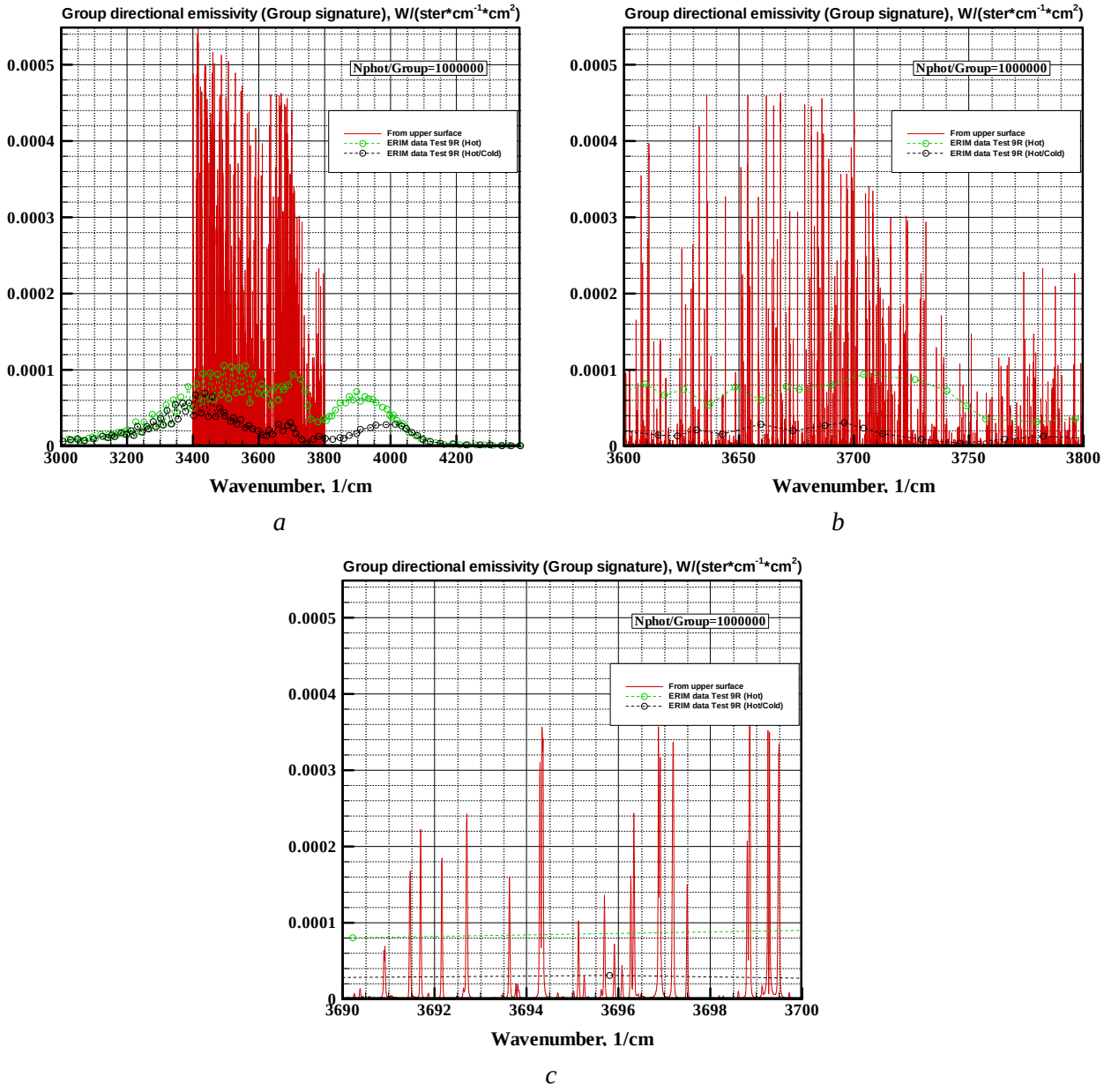

Figure 6.57: Line-by-line prediction of spectral intensity for conditions of ERIM experiments (Test 9R); Hot-through-cold radiance (H_2O/N_2); spectral resolution is $\Delta\omega = 0.0083\ cm^{-1}$

With reference to Figures 6.56 and 6.57 it can be seen that the spectral intensity is changed inside range of ~5 orders. Therefore, it is easy to understand that the problem of averaging of the intensity in spectral region of $\sim \Delta\omega_g \sim 25\ cm^{-1}$ is very complex and difficult problem, which is very sensitive to many input factors of used models.

6.7.4 Spectral signatures of fireballs generated at chemical explosions [51]

Radiative gas dynamics and emission of heat radiation of fireballs generated at large-scale accident at chemical industry, natural gas transportation or rocketry is considered in the section. The problem will be illustrated on the example of rocket accident at active part of trajectory. It was shown at qualitative analysis of processes accompanying explosion of rockets on a launching pad or in flight [52] that after end of shock-wave stage of the process, formation of fireball is rather probable. The fireball is a burning cloud of a mix of components of rocket fuel, which emerges in the environment atmosphere under action of the

Archimedean force, involving in the movement big masses of ambient air. The process of the fireball formation, in turn, can be presented as the following two-stage process:

1) *Expansion of the burning mix during the first 3÷7 seconds of the process.* Feature of this phase of the process is the fast increasing of the fireball sizes. Average speed of such expansion reaches to 20 m/s. Thermal radiation of the fireball accrues most quickly at this stage, reaching the maximum at 5÷7 second of the process. Then intensity of heat radiation gradually decreases owing to intensive cooling of the fireball.

2) *Emersion of the fireball in the environment atmosphere.* Feature of this stage is fast emersion of the fireball, accompanying with involving in movement of the big masses of air and formation of large-scale vortical movement in the free atmosphere. The fireball intensively exchanges heat with ambient air during its emersion. In spite of the fact, that its thermal radiation is not so high (due to relative low temperatures, ~ 500 ÷ 1000 K), heat exchange by radiation plays an important role in the fireball dynamics.

Multi-component model of chemically reacting gas generated at burning of rocket fuel (H_2O, CO_2, CO, H_2) was suggested and studied in [51] for prediction of the fireballs dynamics in view of heat exchange by heat radiation and its influence on gas-dynamic processes (in this sense the term *radiating gas dynamics* was introduced in [52]). It will be shown here how the spectral signature registered from large distance of the fireball reflects physical-chemical processes accompanying the phenomenon under consideration.

Figures 6.58, 6.59 show temperature, mass fraction of H_2O and CO_2 molecules, and velocity vector field in the fireball at consecutive time moments after a rocket explosion.

Being based on these data we shall describe a qualitative picture of a process of the fireball dynamics:

1) Rather fast expansion of the fireball (~ 3 s) with its simultaneous cooling approximately up to ~ 1000 K is observed. The fireball form remains practically spherical on this time interval.

2) Vortical movement of gas is formed inside and outside of the fireball on the 5th second of the process.

3) To the same time moment the fireball begins to lose its spherical form (Figure 6.58,a). It concerns both to temperature distribution, and to distribution of mass fractions of molecular species. The top boundary of the fireball at this time moment is displaced approximately on 200 m, reaching height of 800 m.

4) Further, the fireball continues to move, being increased in the sizes that occur because of involving in the movement of atmospheric air, which is heated and mixed with products of combustion of the rocket fuel. For example, through 11 сек after explosion, the top boundary of the fireball heated up area reaches height of 1000 m (Figure 6.58,b), and to 21 s – 1200 m (Figure 6.58,d). From these figures the increase of the fireball radial sizes is clearly visible.

5) As it was already marked, the cooling of the fireball is observed in process of its rise. A rate of the cooling is the most quick at the first 5 s, due to significant radiating losses of energy. Gradually the basic mechanism of the energy loss due to thermal radiation is replaced by the convective heat exchange, and the rate of the cooling is reduced. By the 21st second of the process the temperature inside the fireball falls approximately to 600 K.

6) It is visible from Figure 6.58 that to 21st second of the process the vortical movement of atmospheric air and burning products covers region more than 1 km on height, and ~ 500 ÷ 600 m in radial direction.

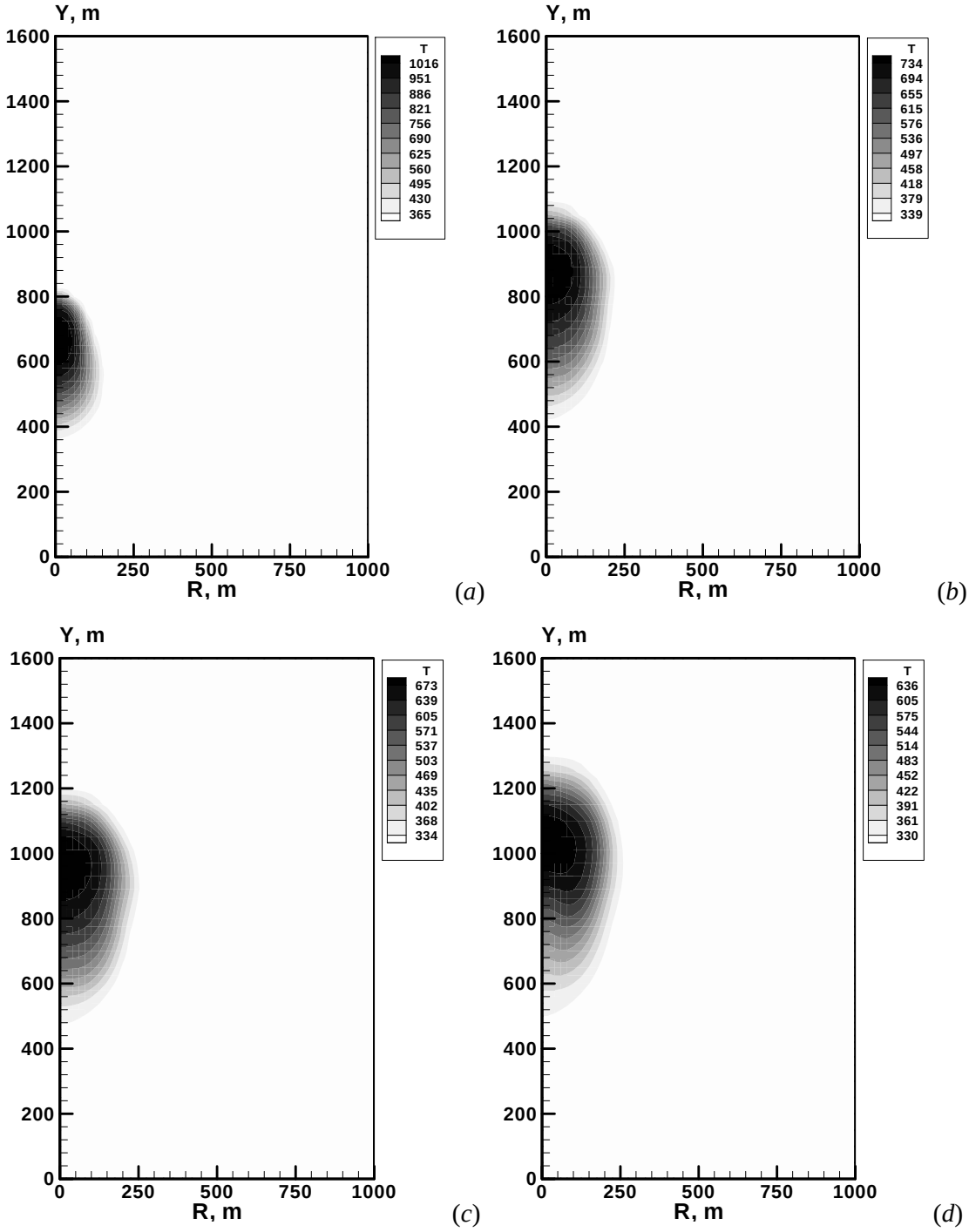

Figure 6.58: Temperature distribution in fireball at consecutive time moments: (*a*) t = 5 s, (*b*) t = 11 s, (*c*) t = 15 s, (*d*) t = 21 s

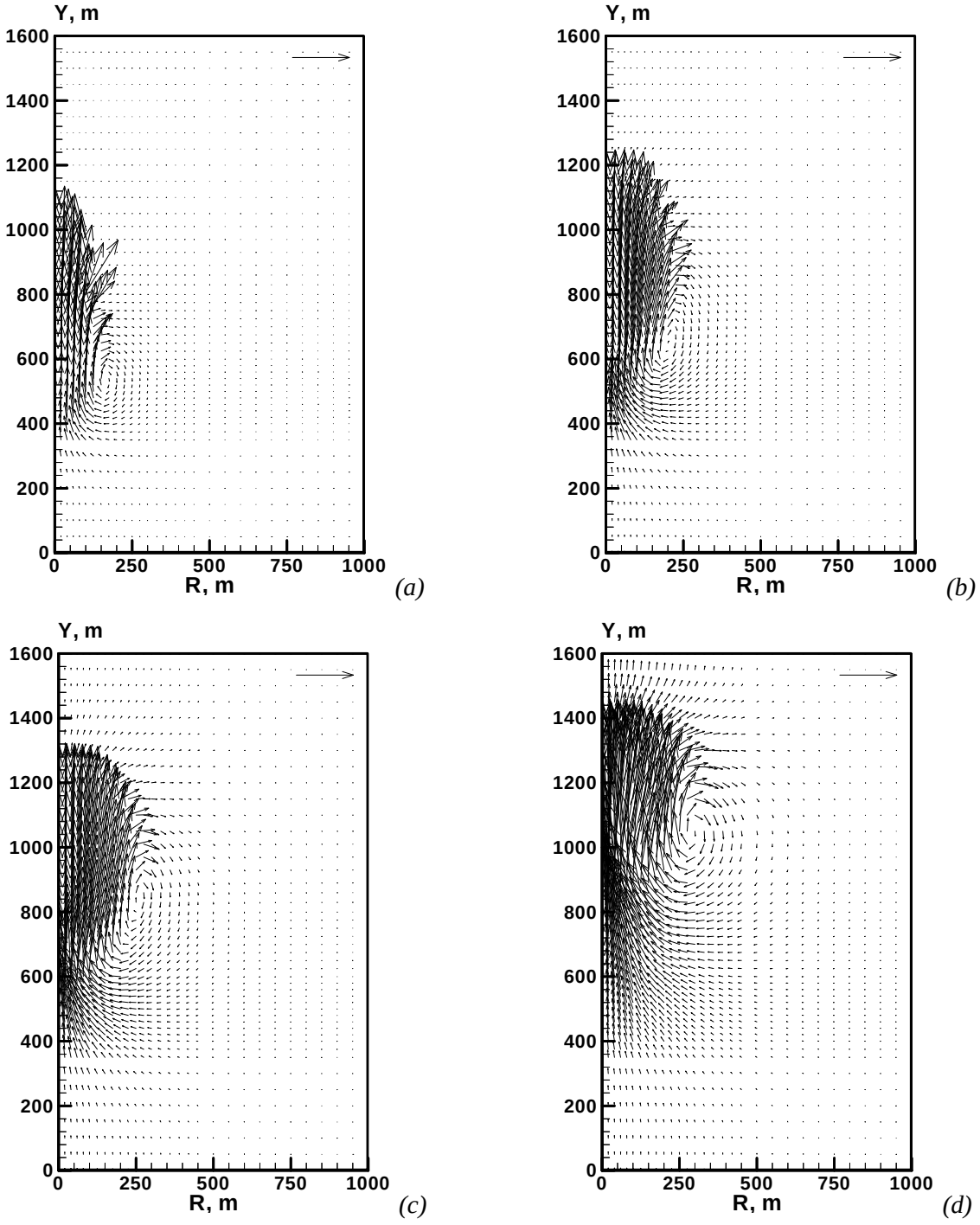

Figure 6.59: Velocity field in fireball at consecutive time moments: (*a*) t = 5 s, (*b*) t = 11 s, (*c*) t = 15 s, (*d*) t = 21 s; velocity scale (50 m/s) is shown in right top corner

Strong influence of radiating processes on dynamics of fireballs was established in [52]. It means that in spite on the fact that temperature inside fireball is not very high, the radiation emission and reabsorption have significant influence on the fireball dynamics due to its large sizes. For example, the full radiative gas dynamic model gives maximum temperature inside the fireball ~ 1140 K to the 5th second after explosion. If we take into account only radiation emission (without reabsorption) this temperature will be

approximately 600 K. This result is quite natural, because losses of thermal energy by heat radiation are rather great. It is easy to estimate the role of heat radiation reabsorption comparing temperature distributions at identical time moments for different models of radiation heat transfer: the significant part of the radiant energy does not leave the heated volume, reducing total losses of the fireball energy. It is obviously that the total energy balance makes significant effect on all parameters of the fireball.

Fields of temperature and species concentrations presented above were used for calculation of spectral signature of the fireball at normal direction to its axis of symmetry. Figures 6.60, 6.61 show spectral signatures in W/(μm·sr) at consecutive time moments. The Monte-Carlo simulation technique was used in 180 spectral bands covered spectral range $\Delta\Omega = 1000 \div 9000\,\mathrm{cm}^{-1}$.

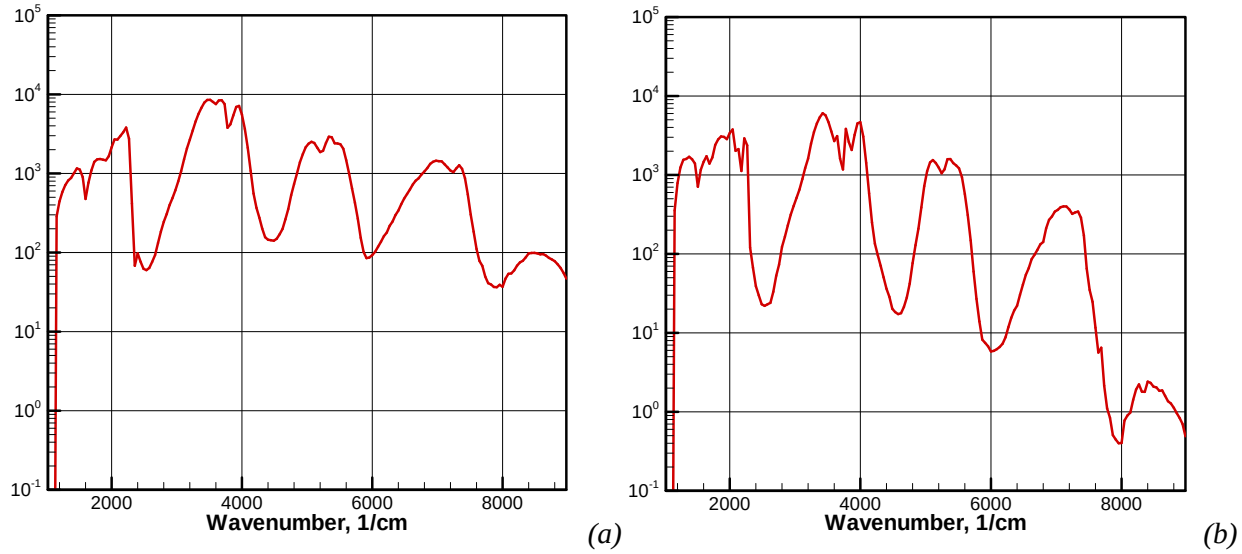

(a) *(b)*

Figure 6.60: Spectral signature (W/(μm·sr)) of the fireball at t = 2 s and 5 s

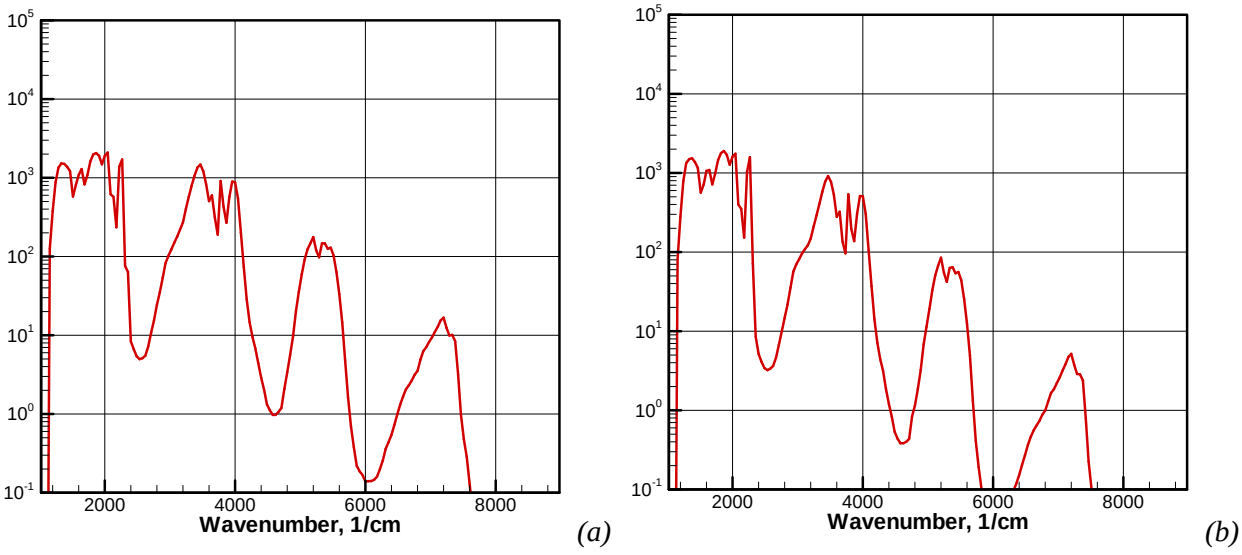

(a) *(b)*

Figure 6.61: Spectral signature (W/(μm·sr)) of the fireball at t = 11 s and 15 s

Homogeneous spectral grid was used here. One million photon groups were modeled in the each spectral group.Analysis of the data presented allows conclude that time dependence of spectral signature adequate reflects facts of increasing of the fireball size and cooling processes. One can see that the spectral signature in short-wave part of investigated spectral region (at wave-number larger than 6000 cm^{-1}) drops

more quickly than in long-wave part due to fast cooling. Spectral emissivity in the long-wave part (at wave-number $\rightarrow$ 1000 cm^{-1}) corresponds to relative low-temperature regions of the fireball. Therefore, practically stable radiation in this spectral region is clarified by the following: not very high rate of cooling of the fireball in temperature region ~ 400 ÷ 600 K is compensated by increasing of its size.

So, presented in [51] radiative gas dynamic model of fireballs generated at rocket explosions at active part of trajectory allows predict time-dependence of spectral signature. It is shown that to predict adequate spectral signature of fireball it is necessary to take into account not only gas dynamic and burning processes, but also radiation heat transfer processes. Presented numerical simulation results show that typical time for registration of a rocket explosion by spectral signature is more than ~30 s.

REFERENCES

[1] Surzhikov, S.T., "Creation of the Emitting Gas Dynamic Radiative Models by Computing Experiment," Moscow, "Nauka", 1992 (in Russian)

[2] Pomraning, G.C., "The Equations of Radiation Hydrodynamics," Pergamon Press. 1973. 286 p.

[3] Ozisik, M.N., "Radiative Transfer and Interactions with Conduction and Convection," A Wiley-Interscience Publication, John Wiley & Sons, 1973.

[4] Surzhikov, S.T., "Heat Radiation of Gases and Plasma," Moscow. Baumansky State University Press. 2004. 544 p. (in Russian)

[5] Abramowitz, M., Stegun, I.A. (Eds.), "Handbook of Mathematical Functions," NBS. Applied Mathematical Series 55. 1964.

[6] Mark, J.C., "The Neutron Density Near a Plane Surface," Phys. Rev. 1947. Vol.72. P.558.

[7] Marshak, R.E., "Variation Method for Asymptotic Neutron Densities," Phys. Rev. 1947. Vol. 71. P. 668.

[8] Sherman, M.P., "Moment Methods in Radiative Transfer Problem," JQSRT. 1967. Vol. 7. № 1. pp.89–109.

[9] Fivelend, W.A., "Three- Dimensional Radiative Heat- Transfer Solutions by the Discrete- Ordinates Method", J. of Thermophysics and Heat Transfer, 2 (1988), pp.309–316.

[10] Fivelend, W.A., "A Discrete Ordinates Method for Predicting Radiative Heat Transfer in Axisymmetric Enclosures", ASME Paper 82-HT-20.

[11] Ramankutty, M.A., Crosbie, A.L., "Modified Discrete- Ordinates Solution of Radiative Transfer in Three- Dimensional Rectangular Enclosures", JQSRT, 60 (1998), pp.103–134.

[12] Menart, J., "Radiative Transport in a Two-Dimensional Axisymmetric Thermal Plasma Using the S–N Discrete Ordinates Method on a Line-by-Line Basis", JQSRT, Vol. 67, 2000, pp.273–291.

[13] Filipskiy, M., Mokrov, M., Surzhikov, S., Capitelli, M., Colonna, G., "Prediction of Radiative Heating of Internal Surfaces of Hydrogen and Air Laser Plasma Generators Intended for Aerospace Applications", 1th International Workshop on Radiation of High Temperature Gases in Atmospheric Entry; 8-10 October 2003, Lisbon, Portugal (ESA SP-533, December 2003), pp.11–18.

[14] Filipskii, M.V., Surzhikov, S.T. "Numerical Simulation of Radiation Heat Transfer in Laser Plasma Generators," AIAA 04-0988, 2004, Reno, NV, pp.1–11.

[15] Sakami, S., Charette, A., V. Le Dez, "Analysis of Radiative Heat Transfer in Enclosures of Complex Geometry Using the Discrete Ordinates Method", Proceedings of the Second International Symposium on Radiation Transfer, Kusadasi, Turkey, July, 1997, M. Pinar Mengüç Editor, Begell House, pp.253–270, 1998.

[16] Filipskii, M.V., Surzhikov, S.T. "Discrete Ordinates Method for Prediction of Radiative Heating of Space Vehicle," AIAA Paper 05-4948. 2005. 11 p.

[17] Goody, R.M., "Atmospheric Radiation. I. Theoretical Basis," Oxford at the Claredon Press, 1964.

[18] Plass, G.N., "Models for Spectral Band Absorption," J.Opt.Soc.Am., 1958, Vol.48, P.690.

[19] Taine, J., Soufiani, A., "Gas IR Radiative Properties: From Spectroscopic Data to Approximate Models," Advances in Heat Transfer. Vol.33 1999. pp.295–414.

[20] Surzhikov, S.T., "Macrostatistical Model Describing Heat Transfer by Radiation with Due Regard for the Vibrational Band Spectrum. Formulation of the Model," High Temperature. 1998. Vol.36. No.2. pp.269–274.

[21] Surzhikov, S.T., "Macrostatistical Model Describing Heat Transfer by Radiation with Due Regard for the Vibrational Band Spectrum. Calculation of Radiation Transfer," High Temperature, 1998, Vol.36. No.3. pp.451–457.

[22] Edwards, D.K., "Molecular Gas Band Radiation," Advances in Heat Transfer. 1976. Vol.12. Edited by Thomas F.Irvine, Jr., James P. Hartnett. Academic Press, New York, San Francisco, London.

[23] Curtis, A.R., Discussion of "A Statistical Model for Water-Vapour Absorption" by R.M.Goody. Quart. J. Roy. Meteorol. Soc. 1952. Vol.78. P.638.

[24] Godson, W.L., "The Evaluation of Infra-Red Radiative Fluxes due to Atmospheric Water Vapour," Quart. J. Roy. Meteorol. Soc. 1953. Vol.79. P.367.

[25] Surzhikov, S.T., Howell, J.R., "Monte-Carlo Simulation of Radiation in Scattering Volumes with Line Structure," J. of Thermophysics and Heat Transfer. 1998. Vol. 12. No. 2. pp. 278–281.

[26] Surzhikov, S.T., "Numerical Simulation of Radiant Emittance of Light-Scattering Plane and Cylindrical Volumes with Regard to Linear Structure," AIAA Paper 2001-2972, 2002, 11p.

[27] Surzhikov, S.T., "Spectral and Narrow Band Directional Emissivity of Light-Scattering and Non-Scattering Volumes," AIAA Paper 2002-3324, 2002, 21p.

[28] Surzhikov, S.T., "Direct Simulation Monte-Carlo Algorithms for the Rocket Exhaust Plumes Emissivity Prediction," AIAA 2002-0795, 2002, 14-17 Jan., Reno/NV, P.11.

[29] Bohren, C.F., Huffman, D.R., "Absorption and Scattering of Light by Small Particles," A Wiley-Interscience Publication, John Wiley&Sons, New-York, 1983.

[30] Nelson, H.F., "Influence of Particles on Infrared Emission from Tactical Rocket Exhaust," Journal of Spacecraft and Rockets, 1984, Vol.21, No.5, pp.425–432.

[31] Surzhikov, S.T., "Monte-Carlo Simulation of Plumes Spectral Emission," AIAA Paper 2003-3895, 36th AIAA Thermophysics Conference, 23-26 June 2003, Orlando, Florida.

[32] Duff, J.W., Bernstein, L.S., "Monte Carlo Scattering of Sunlight by High Altitude Rocket Plumes," JQSRT, 1981, Vol.26, pp.85–102.

[33] Surzhikov, S.T. "Prediction of 3D Rocket Exhaust Plume Signatures by the Monte-Carlo Method," AIAA Paper No.04-1354, 2004, Reno, NV, pp.1–11.

[34] Kotov, D.V., Surzhikov, S.T., "Benchmark Solutions for the Monte-Carlo Simulation Prediction of Spectral Signatures," AIAA paper 05-4947. 2005. 11 p.

[35] Ludwig, C.B., Malkmus, W., Reardon, J.E., Thomson, J.A.L, "Handbook Infrared Radiation from Combustion Gases," NASA, Washington, D.C., 1973; Ludwig, C.B., Malkmus, W., et al., "The Standard Infrared Radiation Model," AIAA 81-1051, 1981.

[36] Rothman, L.S., Gamache, R.R., Tipping, H., et al., "The HITRAN Molecular Database: Editions of 1991 and 1992," JQSRT. 1992. Vol.48. No.5/6. pp.469–518; Also edition of 1996 (on CD).

[37] Tashkun, S.A., Perevalov, V.I., Teffo, J.-L., et al. CDSD-1000, "The high temperature carbon dioxide spectroscopic databank," JQSRT, 2003, Vol. 82, pp.165–196.

[38] Li, W., Tong, T.W., Dobranich, D., Gritzo, L.A. "A Combined Narrow- and Wide-Band Model for Computing the Spectral Absorption Coefficient of CO_2, CO, H_2O, CH_4, C_2H_2, and NO", JQSRT. 1995. Vol. 54. No. 6. pp.961–970.

[39] Surzhikov, S.T., "Optical Properties of Gases and Plasmas," Moscow, Moscow State Technical University Press, 2004, 575 p.

[40] Surzhikov, S.T., "Calculation of the radiation flux divergence near the region of local heat release by quadromoment method. Radiative Transfer – 1," Ed. M. Pinar Menguc. Begell House, Inc., New York. 1996. pp. 92 – 106.

[41] Filipskiy, M., Mokrov, M., Surzhikov, S., Capitelli, M., Colonna, G., "Radiative Heating of Internal Surfaces of Hydrogen Laser Supported Plasma Generator," AIAA Paper 2003-4037, 34th AIAA Plasmadynamics and Lasers Conference, 23-26 June 2003, Orlando, Florida.

[42] Surzhikov, S.T., "Subsonic Radiation Gas Dynamics in a Laser Plasma Generator Channel," Fluid Dynamics. 2005. Vol.40. No.3. pp.446–461.

[43] Surzhikov, S.T., "2D CFD/RGD Model of Space Vehicles," Proceedings of the 1st International Workshop on Radiation of High Temperature Gases in Atmospheric Entry; 8-10 October 2003, Lisbon, Portugal. ESA- 533, December 2003, pp.95–102.

[44] Surzhikov, S.T., "TC3: Convective and Radiative Heating of MSRO for Simplest Kinetic Models," Proceedings of the International Workshop on Radiation of High Temperature Gases in Atmospheric Entry. Part II.30 Sept.-1 Oct., 2005. Porquerolles. France. ESA SP-583, May 2005, pp.55–62.

[45] Surzhikov, S.T., "Numerical simulation of heat radiation generated by entering space vehicle," AIAA 2004-2379, 2004, p.11.

[46] Surzhikov, S.T., "Radiative Gasdynamic Model of a Martian Descent Space Vehicle," AIAA Paper No.04-1355, 2004, Reno, NV, pp.1–11.

[47] Surzhikov, S.T., "Computing System for Solving Radiative Gasdynamic Problems of Entry and Re-Entry Space Vehicles", Proceedings of the 1st International Workshop on Radiation of High Temperature Gases in Atmospheric Entry; 8-10 October 2003, Lisbon, Portugal. ESA- 533, December 2003, pp.111–118.

[48] Surzhikov, S.T., "Random Models of Atomic Lines for Calculation of Radiative Heat Transfer in Laser Supported- and Shock Waves," AIAA Pap. 97-2367, 28th AIAA Plasmadynamics and Laser Conference, June 1997, Atlanta, GA.

[49] Surzhikov, S.T., "Hybrid Monte-Carlo/Random Model of Molecular Lines Algorithm for Signature Prediction," AIAA paper 2006-1187. 2006. 17 p.

[50] Lindquist, G.H., Arnold, C.B., Spellicy, R.L. "Atmospheric Absorption Applied to Plume Emission. Experimental and Analytical Investigations of Hot Gas Emission Attenuated by Cold Gases," Report ERIM No. 102700-20-F, AFRPL-TR-75-30. August 1975, 208 p.

[51] Surzhikov, S., Levine, J., "Time-Dependent Spectral Radiation of Fire Ball Generated at Rocket Explosion," AIAA Paper 2003-1054, 41st Aerospace Sciences Meeting & Exhibit, 2003, Reno, NV.

[52] Surzhikov, S.T., Labourdette, P., "Numerical Simulation of Large-Scale Oxygen-Hydrogen Fire Balls. Semi-Empirical Model," AIAA Pap. 96-1901, 31st AIAA Thermophysics Conference, June 1996, New Orleans, LA.